

ON-CHIP PREPARATION OF BIOLOGICAL  
CELLS USING MICROFLUIDIC ARRAYS

YU CHEN

A DISSERTATION

PRESENTED TO THE FACULTY  
OF PRINCETON UNIVERSITY  
IN CANDIDACY FOR THE DEGREE  
OF DOCTOR OF PHILOSOPHY

RECOMMENDED FOR ACCEPTANCE

BY THE DEPARTMENT OF  
ELECTRICAL ENGINEERING

ADVISER: PROFESSOR JAMES C. STURM

JUNE 2017

© Copyright by Yu Chen, 2017.

All rights reserved.

# Abstract

The analysis of biological cells plays an important role in disease detection and treatment. The credibility of analysis results depends on the quality of prepared cells. The preparation usually starts from extracting the target cells from biological samples, such as tissue, body fluid, and blood. Then multiple preparation processes could be performed: staining with dye, extracellular labeling with monoclonal antibodies, permeabilization for intracellular labeling, fixation for optical observation, lysis for DNA sequencing, and washing to remove unbound labels and unreacted chemicals. Each preparation process often requires several manual steps which may include pipetting, manual shaking, centrifugation, and re-suspension of a pellet after centrifugation.

For more uniformly prepared cell samples, automated and integrated processing and preparation of cells is preferred. Microfabricated arrays of functional structures driven by continuous flow have shown great potentials in achieving high recovery efficiency, purity and quality of prepared cell sample with good practicality in a broad range of cell preparation applications. In this thesis, we will first discuss a methodology for on-chip chemical processing of biological cells using deterministic lateral displacement (DLD) arrays by directing the target cells through sequential regions of treatment chemical and washing streams. With separator walls and long serpentine channels properly designed, the performance can be greatly improved. We then discuss a trap structure array to capture, process, and wash the target cells. Unlike DLD arrays, target cells are immobilized by the trap structures and then processed by sequentially loading treatment chemical, washing, and releasing streams, other than being directed through multiple fixed functional regions. Finally, we discuss concentrating genomic-length DNA using DLD arrays. The experimental and theoretical study is the first step towards high-speed and high-throughput sorting of genomic-length DNA for sequencing applications.

## Acknowledgements

It has been five years since the first time I came to Princeton University. This long journey was not easy. I can still remember how frustrated I am after my first experiment. Fortunately, with the help and support from many people, I managed to reach the end of my doctoral life. First, I would like to thank my advisor, Professor James C. Sturm for being an excellent mentor, and for his inspiring and encouraging advises to help me overcome the many challenges along this road. His perpetual enthusiasm and unwavering support always helped me to do better research and to become a better person. I would also like to thank my co-advisor, Professor Robert H. Austin for providing me the opportunity to do research in his lab, and for his guidance in setting up experiments and the lessons about the importance of tiny details.

Next, I would like to thank all of my colleagues and friends in Sturm and Austin groups. Thanks to Joseph D'Silva and Amy Wu who brought me to the world of microfluidics and showed me how to do great research. Thanks to Saurabh Vyawahare and Jason Puchalla for maintaining the microfluidic facilities and walking me through the microscope problems. Thanks to Ke-Chih Lin for always being able to help. I am also grateful to Julia Bos, Matthew Black, George Liu, Weibin Liang, Can Wu, Warren Rieutort-Louis, Chiao-Ti Huang, Bhadri Visweswaran, Josue Sanz-Robinson, Yasmin Afsar, Levent Aygun, Alexander Berg, Janam Jhaveri, Ken Nagamatsu, and many others, for the interesting discussions, and making the group full of fun and warmth.

I would like to thank my research collaborators for their contributions to this work. Thanks to Professor Curt Civin and his lab member Min Jung Kim, James Moynihan, and Xiaochun Chen at the University of Maryland School of Medicine, and the staff at GPB Scientific LLC for helpful discussions and collaborations on the experiments.

I am thankful to the MNFL staff Pat Watson, Bert Harrop, Joe Palmer, Yong Sun, Sen Liu, and Conrad Silvestre and the IAC staff Nan Yao for their assistance in device fabrication and characterization. I also appreciate the help from the Physics Department Machine Shop staff Bill Dix for making the high quality manifolds used in the experiments.

I would like to thank all of my friends at Princeton and elsewhere. Thanks to Zhuozhi Yao, Xue Wu, Zhaoran Wang, Xiao Shi, Chen Zhao, Duyu Chen, Yu Shen, Suerfu Fnu, Xiaojie Shi, Ruixiang Zhang, and many others, for the countless lunches, dinners, conversations, games, and trips which made the life at Princeton much more enjoyable. Special thanks to my beautiful girlfriend Yawen Xu for the wonderful time we spent together, and for making my life more meaningful.

Last but not least, my deepest gratitude goes to my family for their constant support and encouragement. Thanks to my mom and dad for their understanding of my every decision, and for their spiritually and financially assistance which made my pursuing of Ph.D. possible.

To my parents.

# Contents

Abstract . . . . .	iii
Acknowledgements . . . . .	iv
List of Tables . . . . .	xii
List of Figures . . . . .	xiv
<b>1 Introduction</b>	<b>1</b>
1.1 Background and Motivation . . . . .	1
1.2 Thesis Outline . . . . .	4
1.3 Relation of Work in This Thesis to Publications . . . . .	6
<b>2 Microfluidic Principles, Fabrication Technology and Experimental Setup</b>	<b>7</b>
2.1 Reynolds Number and Péclet Number . . . . .	7
2.2 Deterministic Lateral Displacement . . . . .	9
2.3 On-Chip Chemical Processing of Biological Cells by a Microfluidic Trap Structure . . . . .	11
2.4 Device Fabrication . . . . .	14
2.5 Experimental Setup . . . . .	15
<b>3 On-Chip Chemical Processing of Biological Cells Using DLD Arrays</b>	<b>20</b>
3.1 Introduction . . . . .	20
3.2 Conventional DLD arrays . . . . .	21

3.2.1	Principle of Operation . . . . .	21
3.2.2	Device Performance Analysis . . . . .	22
3.3	DLD Arrays with Separator Walls . . . . .	25
3.3.1	Principle of Operation . . . . .	25
3.3.2	Device Design . . . . .	26
3.3.3	Modelling of Diffusion of Treatment Chemical . . . . .	29
3.3.4	Diffusion of Treatment Chemical to Product Output . . . . .	32
3.3.5	Incubation time vs. output contamination . . . . .	36
3.3.6	Summary of DLD Arrays with Separator Walls . . . . .	40
3.4	DLD Arrays with Long Serpentine Channels . . . . .	40
3.4.1	Principle of Operation . . . . .	40
3.4.2	Device Design . . . . .	42
3.4.3	Flow Control . . . . .	45
3.4.4	Experimental Results . . . . .	48
3.4.5	Summary of DLD Arrays with Serpentine Channels . . . . .	51
3.5	Summary and Outlook . . . . .	52
<b>4</b>	<b>On-Chip Chemical Processing of Biological Cells by Capture and Release Using Microfluidic Trap Arrays</b>	<b>54</b>
4.1	Introduction . . . . .	54
4.2	Device Design . . . . .	56
4.3	Leukocyte Capture . . . . .	58
4.4	Leukocyte Labelling with SYTO 13 and Washing . . . . .	60
4.5	Leukocyte Release . . . . .	62
4.6	Modelling of Cell Capture . . . . .	65
4.6.1	“One-Column” Model . . . . .	66
4.6.2	“Three-Column” Model with Wall Interaction Consideration . . . . .	68
4.7	Capture Efficiency vs. Device Length . . . . .	72

4.8	Modelling of Cell Release . . . . .	74
4.9	On-Chip Chemical Processing of Fixed/Permeabilized Cell Samples Using Microfluidic Trap Arrays . . . . .	76
4.9.1	Introduction . . . . .	76
4.9.2	Capture and Release of Fixed/Permeabilized Cells . . . . .	78
4.9.3	On-Chip Labelling of Fixed/Permeabilized Cells with SYTO 13 . . . . .	81
4.9.4	Clogging of Fixed/Permeabilized K562 Cells in Trap Arrays . . . . .	83
4.10	Summary and Outlook . . . . .	89
<b>5</b>	<b>Concentrating Genomic-Length DNA Using DLD Arrays</b>	<b>90</b>
5.1	Introduction . . . . .	90
5.2	Device Design . . . . .	91
5.3	PEG Compacts DNA by Depletion Force . . . . .	93
5.4	Experimental Results . . . . .	93
5.5	Theory . . . . .	96
5.6	Discussion . . . . .	100
5.7	Summary and Outlook . . . . .	101
<b>6</b>	<b>Conclusion</b>	<b>103</b>
6.1	Summary . . . . .	103
6.2	Comparison between DLD and Trap Arrays for On-Chip Preparation of Biological Cells . . . . .	105
6.3	Future Work . . . . .	108
<b>A</b>	<b>Publications and Presentations</b>	<b>110</b>
A.1	Peer-reviewed Publications . . . . .	110
A.2	Conference Presentations . . . . .	111
<b>B</b>	<b>Fabrication Process</b>	<b>112</b>

B.1 Etching . . . . .	112
B.1.1 Silicon Wafer Preparation . . . . .	112
B.1.2 <20 $\mu\text{m}$ Etching . . . . .	112
B.1.3 >20 $\mu\text{m}$ Etching . . . . .	113
B.2 Device Clean . . . . .	114
B.2.1 Piranha Clean . . . . .	114
B.2.2 HF Clean . . . . .	114
B.3 Device Sealing . . . . .	114
B.3.1 Tape Sealing . . . . .	115
B.3.2 PDMS Sealing . . . . .	115
B.3.3 Anodic Bonding . . . . .	115
<b>C Blood Protocols</b>	<b>117</b>
C.1 Buffer Preparation . . . . .	117
C.2 Whole Blood Sample Preparation . . . . .	118
C.3 RBC Lysed Blood Sample Preparation . . . . .	118
<b>D Fixation and Permeabilization Protocol</b>	<b>119</b>
<b>E DNA Staining</b>	<b>120</b>
E.1 Running buffer . . . . .	120
E.2 DNA staining . . . . .	120
<b>Bibliography</b>	<b>122</b>

# List of Tables

2.1	List of hydraulic diameters . . . . .	8
2.2	Capture efficiencies of some reported microfluidic trap structures . . .	13
2.3	List of diameters of some types of cells . . . . .	14
3.1	$x/\sqrt{4D\tau_{tot}}$ for various degrees of concentration at the outputs . . . .	24
3.2	Incubation time can be achieved using conventional DLD arrays at different conditions . . . . .	25
3.3	Calculated fluidic resistances of DLD arrays and serpentine channels .	47
3.4	Calculated input flow rates and on-chip incubation time for DLD arrays with serpentine channels . . . . .	48
3.5	Recovery efficiency of leukocytes measured in DLD arrays with serpentine channels . . . . .	49
3.6	Contamination and on-chip incubation time for leukocyte labelling with R6G using DLD arrays with serpentine channels . . . . .	51
4.1	Fixed and permeabilized cell samples . . . . .	77
4.2	Recovery efficiency of fixed/permeabilized cells using trap arrays . . .	79
4.3	Recovery efficiency of on-chip labelling of fixed/permeabilized cells using trap arrays . . . . .	84
6.1	Summary for on-chip leukocyte preparation using microfluidic arrays	106

6.2	Chemical use for different labelling processes using off-chip approach, DLD arrays with serpentine channels or trap arrays . . . . .	107
-----	---	-----

# List of Figures

2.1	Schematic of deterministic lateral displacement array . . . . .	9
2.2	Critical size in DLD arrays . . . . .	10
2.3	Schematic of 3-D microfluidic trap structure . . . . .	12
2.4	SEM micrograph of cross section of DLD array . . . . .	15
2.5	The fabrication process for trap array . . . . .	16
2.6	Micrographs of fabricated trap array . . . . .	17
2.7	Experimental setup for an on-chip cell preparation system . . . . .	18
3.1	Schematic of conventional DLD array for on-chip cell preparation . .	21
3.2	Schematic of conventional DLD array for on-chip cell preparation . .	22
3.3	Diffusion of treatment chemical in conventional DLD array . . . . .	23
3.4	Schematic of DLD array with separator walls . . . . .	27
3.5	L-edit design of DLD array with separator walls . . . . .	28
3.6	Fluorescent beads flowing in DLD array with separator walls . . . . .	29
3.7	Fluorescent beads at the outputs of DLD array with separator walls and conventional DLD array . . . . .	30
3.8	Modelling of the diffusion of the treatment chemical . . . . .	33
3.9	2-D COMSOL simulations of relative concentration across DLD arrays	34
3.10	Fluorescent images of R6G flowing in the treatment stream in DLD arrays . . . . .	35
3.11	Experimental and COMSOL simulation results of relative concentration	38

3.12	Fluorescent images of on-chip leukocyte staining with R6G . . . . .	39
3.13	Schematic of DLD arrays with a very long serpentine channel for on-chip incubation . . . . .	41
3.14	Symmetric 3-zone DLD array to achieve high recovery efficiency of leukocytes . . . . .	43
3.15	Design of 3-zone DLD arrays with long serpentine channels created using L-edit software . . . . .	44
3.16	Fluidic analogous circuit model of DLD arrays with serpentine channels	46
3.17	Fluorescence images of on-chip leukocyte labelling with R6G using DLD arrays with serpentine channels . . . . .	50
4.1	Operations for on-chip labelling of biological cells using trap array . .	57
4.2	Schematic of 3-D microfluidic trap structure . . . . .	58
4.3	Trap array design . . . . .	59
4.4	Leukocyte capture in trap arrays . . . . .	60
4.5	Experimentally measured leukocyte capture efficiency . . . . .	61
4.6	SYTO 13 leukocyte labelling and washing . . . . .	62
4.7	Total fluorescence intensity measured for on-chip SYTO 13 leukocyte labelling and washing . . . . .	63
4.8	Leukocyte release from trap array . . . . .	64
4.9	Experimentally measured leukocyte release efficiency . . . . .	65
4.10	Fluidic analogous circuit model of trap array . . . . .	66
4.11	Schematic of flow field at the center plane of trap array . . . . .	71
4.12	The simulated capture efficiencies of particles of different diameters in 6- $\mu\text{m}$ critical gap trap array . . . . .	72
4.13	Capture efficiency vs. device length . . . . .	73
4.14	COMSOL simulation for releasing a 10- $\mu\text{m}$ bead from a 6- $\mu\text{m}$ critical gap device . . . . .	75

4.15	Forward and side scatter plots of fixed/permeabilized cell experiments	80
4.16	Side scatter and SYTO 13 fluorescence intensity plots of on-chip labelling of fixed/permeabilized cells . . . . .	82
4.17	Side scatter and SYTO 13 fluorescence intensity plots of conventional 30 min off-chip labelling of fixed/permeabilized cells . . . . .	83
4.18	Fluorescence images of different numbers of fixed/permeabilized K562 cells loaded to 8- $\mu$ m critical gap trap arrays . . . . .	85
4.19	Possible mechanism of on-chip clogging of cells in trap array . . . . .	86
4.20	Release of fixed/permeabilized K562 cells from 8- $\mu$ m critical gap trap arrays . . . . .	87
5.1	DNA concentrator design . . . . .	92
5.2	Depletion force induced by PEG crowding . . . . .	94
5.3	DNA concentrating in DLD array . . . . .	95
5.4	DNA in DLD array . . . . .	96
5.5	DNA extent in the flow direction under different conditions . . . . .	97
5.6	DNA behaviors in DLD array under different conditions . . . . .	98

# Chapter 1

## Introduction

### 1.1 Background and Motivation

The quality of prepared biological samples (viability, uniformity of cell size, low background fluorescence noise, less contamination of bacteria, etc.) is critical for the credibility of later analysis, such as flow cytometry to detect disease and DNA sequencing to read out genomic information. The preparation usually includes but is not limited to extraction and purification of the target cells, cell culture to enrich rare cells, intracellular and extracellular labelling, fixation, permeabilization, lysis, and washing between each two steps and at the end to avoid contaminations of unreacted chemicals. Each preparation step often requires multiple manual processes, which may include pipetting, centrifugation, and re-suspension of a pellet after centrifugation. These labor-intensive steps will inevitably cause variations and introduce artifacts to the quality of prepared cells and the results of sub-sequential analysis or diagnosis [1].

A lab-on-a-chip, a device that integrates multiple laboratory functions on a single chip, may be the solution to replace the labor-intensive preparation steps described above, where microfluidics plays an important role. Microfluidics refers to the physics

and engineering that manipulates and studies of minute amounts of fluids in micro- or nano-scale structures, which enables the miniaturization, integration and automation of biochemical assays. This research field has blossomed since A. Manz [2] introduced the term miniaturized total analysis system, now synonymous with micro total analysis system,  $\mu$ TAS. Many types of microfluidic devices for on-chip process, preparation and analysis of biological cells have been developed in the past decades. However, none of them has been mass produced due to the complex nature of fluids and biological cells in micro- and nano-scale.

Some microfluidic devices can perform one of the cell preparation steps. M. A. McClain, et al. have shown a microchannel for on-chip cell lysis using electric field [3]. Conventional centrifugation (and washing) is still needed before (and after) the on-chip cell lysis. Moreover, the distinctive structures of this type of microfluidic devices often lead to difficulties in higher level integration. J. Nguyen, et al. have presented a Polydimethylsiloxane (PDMS) microfluidic system for on-chip whole blood cell count and preparation from raw blood [4], which has a complicated design of multiple functional sections and needs accurate fluid controls to function correctly, limiting its practicality.

Other cell preparation and processing devices with simpler structures include a “centrifuge on-chip” device for cell preparation using simple rectangular shaped channels [5]. However, the underlying separation mechanism of on-chip vortices limits the cell capture efficiency to 20%. Integrated microfluidic devices for chemical treatment with high cell capture efficiency are often limited by the diffusion of the treatment chemical. The diffusion of the treatment chemical will cause a contamination at the output by the treatment chemical and a decrease of the effective concentration of the treatment chemical at the processing region. Usually, a high flow speed is required to avoid this diffusion. A. P. Tan, et al. have presented a microfluidic device utilizing inertial lift force as the separation mechanism to give very high cell capture efficiency

[6]. The cells are directed into a sodium carbonate stream from a hematoxylin suspension buffer with an acetic acid stream as diffusion barrier to avoid the mixture of sodium carbonate and hematoxylin suspension buffer. However, the flow speed is  $\sim 0.6$  m/s for a treatment chemical's diffusion constant of  $10^{-9}$  m<sup>2</sup>/s, requiring a separate on-chip or off-chip incubation.

Microfluidic arrays of functional structures driven by continuous flow have shown great potentials in achieving high recovery efficiency, purity and quality of prepared cell sample with good practicality in a broad range of cell preparation applications. K. Morton et al. have presented a method for on-chip cell processing in a continuous-flow microfluidic chip, in which deterministic lateral displacement (DLD) arrays are used to move target cells into and then out of a treatment chemical processing stream [7]. High fluid speeds are required to avoid the diffusion of the treatment chemical. However, the simple device design and high cell capture efficiency [8, 9] make the proposed device attractive.

Another type of microfabricated arrays is a microfluidic trap structure. A. Huebner, et al. have demonstrated a simple 2-dimensional trap structure for droplet trapping, incubation and release for enzymatic and cell-based assays [10]. 90% of captured droplets can be released from the trap structure, although the capture efficiency is extremely low:  $>90\%$  of droplets just pass through the trap array. A 3-dimensional trap structure of similar idea is proposed by D. Di Carlo, et al. for on-chip cell culture and single-cell analysis for enzyme concentrations, kinetics, and inhibition [11, 12]. Again the capture efficiency of cells is still very low. Interestingly, a modified 3-dimensional trap structure has shown a capture efficiency of  $\sim 90\%$  of incoming cells [13].

Inspired by these works of microfluidic arrays, we delve deeper toward the goal of automated and integrated cell preparation system with high recovery efficiency (number of cells can be retrieved to that of total input cells) and high quality with optimized design of DLD and trap arrays. This thesis will thus focus on these two

types of microfluidic devices, each of which has had an impact on the field of microfluidics.

## 1.2 Thesis Outline

**Chapter 2** introduces the microfluidic principles for DLD and trap arrays for on-chip preparation of biological cells. The microfluidic arrays depend on accurately controlled dimensions to function correctly. Microfabrication technology enables us to quickly fabricate and test the devices as designed. The fabrication technology and experimental setup used in this thesis are also described in this chapter.

**Chapter 3** discusses the development of on-chip chemical processing of biological cells using DLD arrays. The quality of prepared cell samples is significantly affected by the incubation time and contamination of the treatment chemical to the product. Usually long incubation time (30 min to many days [14–19]) is preferred such that the treatment chemical is completely reacted and the prepared cells have strong fluorescence intensity. However, the treatment chemical will have enough time to diffuse away from the incubation region, reducing the effective concentration of treatment chemical and affecting the quality of the prepared cells. To maintain the concentration of treatment chemical, we can continuously load the treatment chemical to the device, which can be very costly. The other bad consequence of the diffusion of treatment chemical is its contamination to the prepared cells, thus affecting the later analysis results, such as increasing the background fluorescence noise and generating undesired side products. To avoid this type of contamination, high flow speed was used in conventional DLD array design where target cells were driven through a treatment chemical, and washing region. The high flow speed not only decreases the total residence time of the treatment chemical but also decreases the total incubation time. Therefore, conventional DLD array can be used only for applications

that don't require long incubation time ( $<1$  s). To resolve this trade-off between long on-chip incubation time and low contamination, we introduced separator walls and serpentine channel to the conventional DLD array. The former extended the on-chip incubation via concentrating the target cells along the first separator wall for an increased on-chip incubation, and confined the diffusion of treatment chemical in a smaller region. A second separator wall further reduced the contamination at low flow speed via blocking the treatment chemical. The later provided a long serpentine channel for on-chip incubation up to 10 min for target cells and washed the chemical processed cells in a second DLD array to have desired level of contamination of treatment chemical. On-chip leukocyte labelling with Rhodamine 6G (R6G) was demonstrated using these two designs.

**Chapter 4** discusses the development of on-chip chemical processing of biological cells using microfluidic trap arrays. Unlike DLD arrays, target cells are immobilized by the trap structures and then processed by sequentially loading treatment chemical, washing, and releasing streams, other than being directed through multiple fixed functional regions. In principle, cells can be on-chip incubated for infinite time and can be washed until the desired contamination level of treatment chemical is reached. However, as cells gradually forms adhesion bonds to the substrate surface and the other cells, it is impossible to release all of the cells from the device, affecting the cell recovery efficiency. Experimental results showed that  $\sim 90\%$  of captured cells can be released from the trap array with incubation time up to 20 min. The other concern is the varying capture efficiency, which is significantly affected by the geometry of the trap structure. For a quick design for other on-chip cell preparation applications, we developed a qualitative model to explain and predict the device performance. This model also provided numerical results which can be used as a guide to design the microfluidic trap structure. On-chip leukocyte labelling with SYTO 13

was demonstrated using this design with  $\sim 85\%$  capture efficiency and  $\sim 99\%$  release efficiency.

**Chapter 5** extends the work of DLD array to concentrate genomic-length DNA. Concentration and purification of genomic-length DNA is the first step for DNA sequencing, conventionally done by electrophoresis (very long running time), or long nano-channels (low throughput). DLD array with resolution down to 10 nm provides the possibility for high-speed and high-throughput DNA concentration. However, as DNA is stretched by the shear flow between posts, it is not possible to displace the polymer like and extremely long DNA molecule. In this chapter, polyethylene glycol (PEG) was introduced to compact 166 kbp T4 DNA into globular conformation via depletion force. The compacted DNA was less stretched in the array due to an increase in shear modulus, and thus can be displaced and concentrated in a DLD array. A DNA concentrator driven by continuous fluid flow was demonstrated using this approach.

**Chapter 6** summarizes our contributions and makes suggestions for the future work in this area.

### **1.3 Relation of Work in This Thesis to Publications**

Chapter 3 is based on work published in *Biomicrofluidics* [20]. Chapter 4 is being prepared for publication. Chapter 5 contains the work published in *Physical Review Letters* [21]. As it is the policy with most of these journals, we include in the bibliography the appropriate copyright notices whenever we reproduce material directly from published articles.

# Chapter 2

## Microfluidic Principles, Fabrication Technology and Experimental Setup

### 2.1 Reynolds Number and Péclet Number

Throughout most of this thesis, and in microfluidics in general, the concept of low Reynolds number flow is important. The Reynolds number  $Re$  is a dimensionless number describing the ratio of inertial to viscous forces present in a flow. It is defined as

$$Re = \frac{\rho v L}{\mu} \quad (2.1)$$

where  $\rho$  is the density of the fluid,  $v$  is the fluid flow speed,  $\mu$  is the dynamic viscosity of the fluid, and  $L$  is a characteristic linear dimension. When the fluid is confined in a bounded region, such as circular, square and rectangular duct,  $L$  can be replaced by hydraulic diameter  $D_H$  for a more general description. Table. 2.1 shows the commonly used hydraulic diameters in different confined geometries.

Table 2.1: List of hydraulic diameters

<b>Geometry</b>	<b>Edges</b>	<b>Hydraulic diameter</b>
Circular	Diameter $D$	$D_H = D$
Square	Edge $a$	$D_H = a$
Rectangular	Edges $a$ & $b$	$D_H = \frac{2ab}{a+b}$

Low Reynolds number flow is characterized by smooth and laminar motion, usually described by streamlines, due to negligible inertial forces. This type of flow is important for automated on-chip cell preparation to have uniform and less damaged cell samples. The streamlines are curves that are instantaneously tangent to the flow velocity vector. When  $Re \ll 1$ , we can assume that particle or cell flowing in the fluid moves at the flow speed of the streamline where the particle or cell center is [22].

Another dimensionless number is the Péclet number  $Pe$  which expresses the ratio of the advective and the diffusive transport rate of the particles, which is calculated as

$$Pe = \frac{vL_D}{D} \quad (2.2)$$

where  $L_D = \sqrt{D\tau}$  is the characteristic diffusion length,  $\tau$  is the residence time fluid flowing through a certain region,  $D = k_B T / 3\pi\mu d_P$  is the diffusion constant of the particles or cells,  $k_B$  is the Boltzmann constant,  $T$  is the temperature, and  $d_P$  is the particles or cells' diameter. The flows discussed in microfluidic devices often contain a complex mixture of particles and chemicals, each with a corresponding Péclet number. When  $Pe \gg 1$ , the diffusion of the particles or cells can be ignored. The diffusion of treatment chemicals may induce contamination to the prepared cells and affect the following analysis, such as introducing higher background noise. Moreover, the diffusion of target cells may reduce the number of recovered cells. These effects usually take place when the treatment chemicals' or cells'  $Pe \lesssim 1$ . Therefore when

$Pe \lesssim 1$ , the diffusion of the particles or cells should be taken into consideration to have optimized device design [24].

## 2.2 Deterministic Lateral Displacement

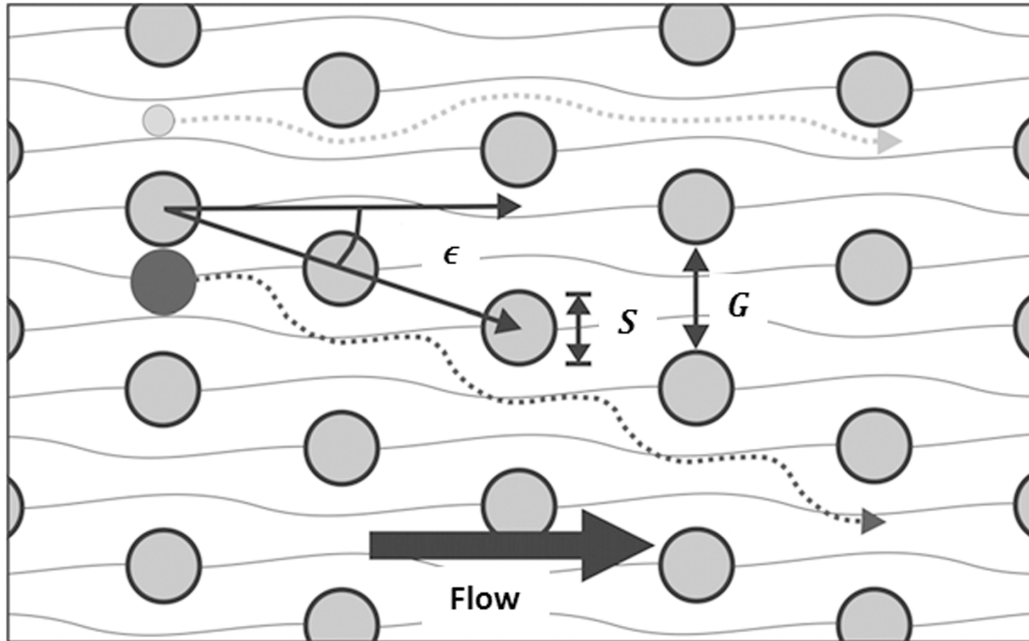


Figure 2.1: Schematic of deterministic lateral displacement (DLD) array. Posts of  $S$  diameter are arrayed in a channel with a gap  $G$  between posts such that one axis of the array forms an angle  $\epsilon$  with the average fluid flow direction. The flux flows through the gaps is divided into  $1/\epsilon$  streams separated by stagnation streamlines that begin and end on posts and show how fluid divides around the posts. Small particles move through the array in a “zigzag” trajectory and follow the average fluid flow direction. Large particles are mechanically displaced downward by the posts at each column and follow the array axis (the migration angle  $\epsilon$ ) in a “bumping” trajectory. Image courtesy of K. Loutharback, et al. [25].

Deterministic lateral displacement (DLD) arrays are microfluidic structures for continuous flow separation of particles by size [26]. The underlying separation mechanism is physical displacement by obstacles arrayed in the fluid flow. Fig. 2.1 shows the schematic of DLD array. Circular posts with diameter  $S$  and gap  $G$  are arrayed with one axis of the array forms an angle  $\epsilon$  to the average fluid flow direction. The

fluid flowing through the gaps is thus divided into  $1/\epsilon$  streams. Therefore  $1/\epsilon$  is often set to be an integer for design convenience. This structure works by asymmetric bifurcation of fluid streams around the posts.  $\epsilon$  and  $1 - \epsilon$  of the fluid flow at different directions around the post. The fluid motion can be characterized by  $1/\epsilon$  streams that periodically cycle through positions in the gap with a periodicity of  $1/\epsilon$ , but travels in an average straight direction, as shown in Fig. 2.1.

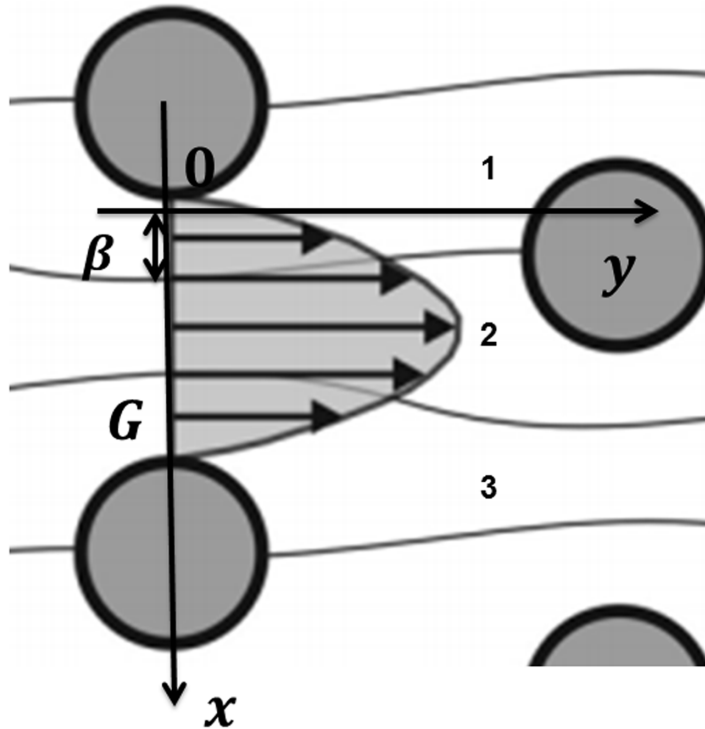


Figure 2.2: Parabolic flow profile between posts of DLD array with  $\epsilon = 1/3$ . The critical size  $D_C = 2\beta$ , where  $\beta$  is the width of the first stream line close to the post. Image courtesy of K. Loutnerback, et al. [25].

Two flow patterns of particles in the DLD arrays can be observed depending on their size relative to the stream next to the post as they move through a gap. The width of this stream is viewed as  $1/2$  of the critical size  $D_C$  and can be numerically solved following a method proposed by D. W. Inglis, et al. [27]. As shown in Fig. 2.2, the flow profile between posts of a DLD array with  $\epsilon = 1/3$ . If the particle's size is larger than 2 times the width  $\beta$  of the first stream line, it will be mechanically pushed

to the second stream line. Therefore, the critical size can be obtained by solving the following equation

$$\int_0^{D_C/2} u(x)dx = \epsilon \int_0^G u(x)dx \quad (2.3)$$

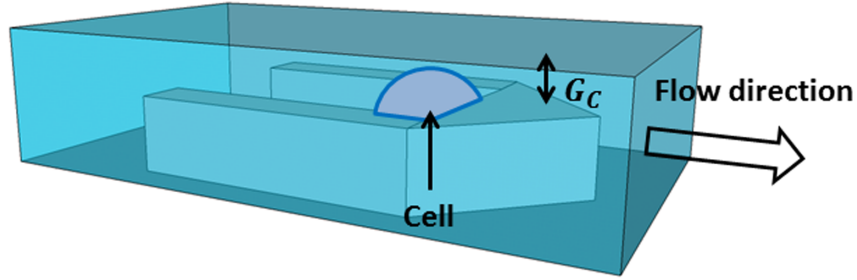
where  $u(x)$  is the flow profile along  $x$ -direction. Parabolic flow profile can be utilized for a quick estimation [27].

Particles whose diameters are smaller than the critical size  $D_C$ , denoted by the light gray particle with dotted trajectory in Fig. 2.1, will remain bound within the stream next to the post as they follow a “zigzag” trajectory that waves around through the posts in an average straight direction. Particles larger than the critical size, denoted by the dark gray particle with dotted trajectory in Fig. 2.1, will be “bumped” by the mechanical force of the posts into the adjacent stream. The cyclical way that the streams move through the gaps then locks large particles into being “bumped” into an adjacent stream at every column of posts and the particle will travel along the migration angle  $\epsilon$  determined by the array geometry. The separation based on size using DLD arrays has shown a large operating range (100 nm to 30  $\mu\text{m}$ ) [8, 28] for a variety of objects including polystyrene beads, DNA, bacteria, human blood cells, and circulating tumor cells (CTCs) [7–9, 26, 29–35], with a resolution down to 10 nm [26, 36].

## 2.3 On-Chip Chemical Processing of Biological Cells by a Microfluidic Trap Structure

A microfluidic trap structure separates target cells from the fluid by forming a critical gap  $G_C$  smaller than the target cells. Different types of trap structure arrays have been proposed for single cell analysis [11, 37], cell culture [12], cell cytometry [38], cell pairing and fusion [13], enzymatic and cell-based assay [10], etc. A 3-D microfluidic

### (a) Trap cell



### (b) Release cell

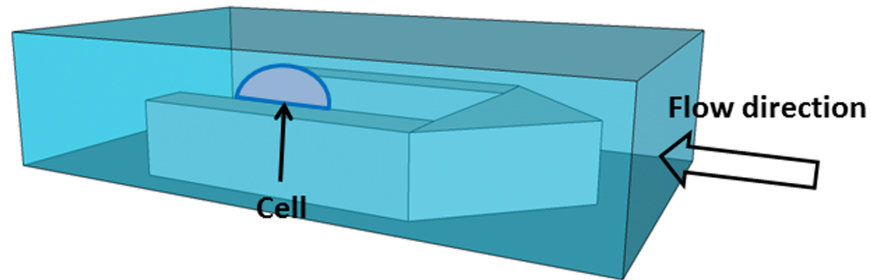


Figure 2.3: Schematic of 3-D microfluidic trap structure, where the lid would be on the top of the 3-D boxed region shown in the figures. There is a critical gap  $G_C$  between the trap structure and lid layer. (a) When a flow is input against the trap structure, cells of size larger than  $G_C$  flowing in the fluid will be physically captured. (b) When a flow is input from the other direction, a net force will be applied on the cells through this critical gap to release the cells from the trap structure.

trap structure schematic, which is designed and tested in this thesis, is shown in Fig. 2.3. When a flow is input against the trap structure, cells of size larger than  $G_C$  flowing in the fluid will be captured within the trap region (Fig. 2.3(a)). Then chemicals, such as labelling solution, culture medium, lysis solution, etc., can be loaded to “on-chip process” the trapped cells. However, there is no “release step” to remove the cells or particles from the traps and to harvest them in nearly all papers to date due to the fact that the trap structures don’t have a streamlined shape, and that the critical gap is not large enough to allow enough fluid flow to provide a large release force. The cells often require a force to be released because they may stick or “bind” to the obstacle. Fig. 2.3(b) shows the streamlined 3-D structure to release

the trapped cells when the flow is input from the other direction. A. Huebner, et al. have demonstrated a simple 2-dimensional trap structure for droplet trapping, incubation and release for enzymatic and cell-based assays [10]. 90% of captured droplets can be released from the trap structure, although the capture efficiency is extremely low: >90% of droplets just pass through the trap array, as is another concern of the microfluidic trap structures. Table 2.2 shows the capture efficiencies (the number of particles or cells captured to that of total input particles or cells) of particles or cells reported in previous works.

Table 2.2: Capture efficiencies of some reported microfluidic trap structures

<b>References</b>	<b>particles</b>	<b>Capture efficiency</b>
A. Huebner, et al. [10]	droplets	< 10%
A. M. Skelley, et al. [13]	NIH3T3 fibroblasts, myeloma cells, B cells, mouse embryonic stem cells, and mouse embryonic fibroblasts	1%, 70%, 90% in three different designs
L. Lin, et al. [39]	HeLa cells	0.3% to 16.3 %
D. Di Carlo, et al. [12]	HeLa cells	< 20% supposing $\approx 10^6$ cells/mL concentration
This thesis	Leukocytes	$\sim 85\%$

However, the large variation in capture efficiencies is not well explained and modelled, limiting the practicality of this type of microfluidic device. In Chapter 4, we developed a qualitative model to explain the achieved capture efficiency in this thesis and previous works. The model also provided the first order numerical results with the consideration of particle's size, which can be used as a quick guide to design microfluidic trap arrays for other on-chip cell preparation applications.

Using the developed model, we designed and fabricated a trap array for on-chip chemical processing of leukocyte. The experimental results showed a capture efficiency  $\sim 85\%$  of input leukocytes, which is as good as Ref. [13]. Then, to demonstrate on-chip chemical processing of cells, the captured leukocytes were labelled with SYTO

13 solution and washed by a washing buffer to remove the background fluorescence noise. Finally, the labelled and washed leukocytes were released from the trap structures, with a release efficiency  $\sim 99\%$  better than previous work (70% to 90%) [10] for short incubation time, and  $\sim 80\%$  for up to 20 min incubation.

## 2.4 Device Fabrication

The microfabricated arrays separate and capture target cells based on their size. Table 2.3 shows the size of some types of cells. All of the listed cells are commonly analyzed and investigated in biological and clinical laboratories for disease detection and treatment development. Thus well-controlled feature size is a critical issue in developing on-chip cell preparation devices using microfluidic arrays based on cell size. Fortunately, microfabrication technologies enable us to fabricate and test the device principle in a short period of time with high resolution in feature size down to 1 nm [40–42].

Table 2.3: List of diameters of some types of cells

Cell name	Diameter ( $\mu\text{m}$ )
Neutrophil	10–12 [43]
Eosinophil	10–12 [43]
Basophil	12–15 [43]
Lymphocyte	7–8 for small lymphocytes, 12–15 for large lymphocytes[43]
Monocyte	15–30 [43]
J82 and T24 bladder cancer cell	12–16 [44]
Breast cancer cell	15–30 [45]
Prostate cancer cell	6.9–8.95 [46]

In this thesis, devices were fabricated in silicon wafers using standard microfabrication techniques. For detailed fabrication procedures, see Appendix B. Fig. 2.4 shows the scanning electron microscopy (SEM) of cross section of DLD array using

deep reactive ion etching (DRIE). Etching masks were formed on the silicon wafers using single-layer photolithography (Karl Suss, MA6) with AZ 1518 photoresist (AZ Electronic Materials, USA) and AZ 300 MIF developer.

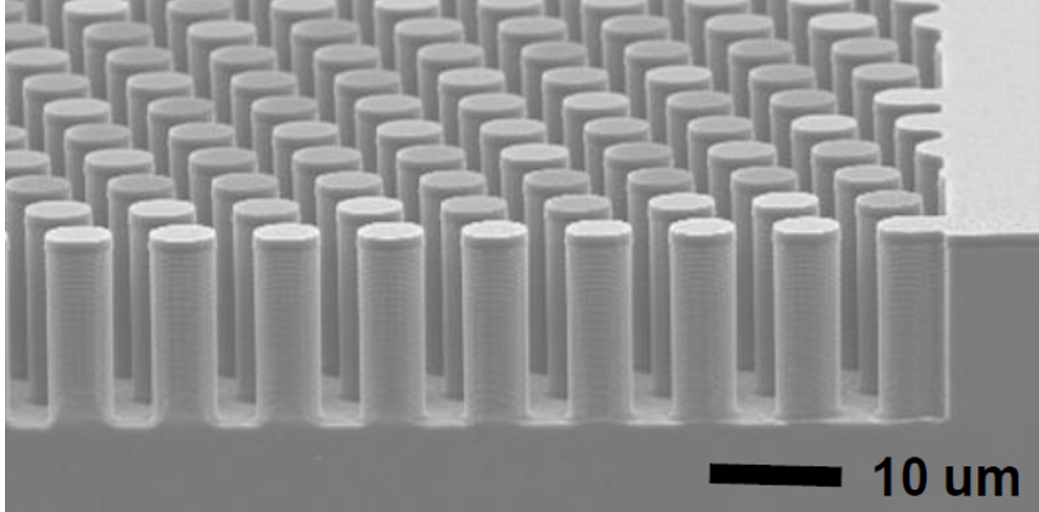


Figure 2.4: Scanning electron microscopy (SEM) of cross section of posts etched into silicon using deep reactive ion etching (DRIE). Image courtesy of K. Loutharback, et al. [25].

The fabrication process for trap arrays was a little more complicated where two-step DRIE was used to create the critical gap (Fig. 2.5). Fig. 2.6(b) and (c) show the micrographs of fabricated trap array like that in Fig. 2.3 with a  $6\text{-}\mu\text{m}$  critical gap using two-step DRIE. Support pillar structures were implemented to avoid the deformation of the Pyrex glass lid (anodically bonded to the pillars and channel walls), to maintain tight control of the critical gap across the device channel (Fig. 2.6(a)). The anodic bonding also allows the devices to be operated at up to 50 psi without problems related to the lid deforming or leaking [47].

## 2.5 Experimental Setup

Once the devices were fabricated, inlets and outlets were through-wafer holes created by either sandblasting using  $50\ \mu\text{m}$  diameter aluminum oxide particles, laser drilling,

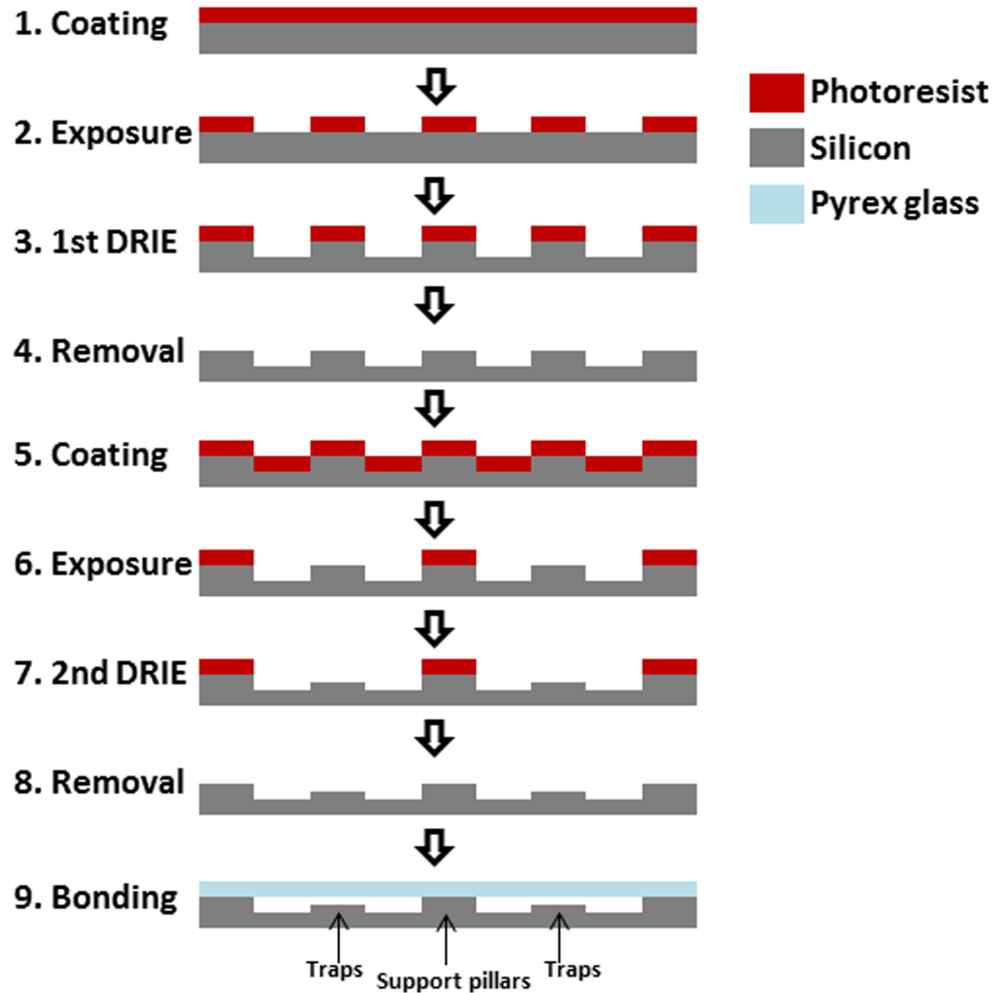


Figure 2.5: The two-step DRIE fabrication process for the trap array.

or another DRIE step. Three sealing methods were used in this thesis to form the transparent lid layer for optical observation: tape, PDMS on coverslip, and anodic bonding (see Appendix B). Then the devices were mounted to a polycarbonate jig (Fig. 2.7(a)) connected to an external syringe pump.  $0.2 \mu\text{m}$  Polytetrafluoroethylene (PTFE) filters were applied to the jig to allow air to be pushed out of the manifold. Finally, a stainless steel metal plate with a window for microscopic observation was used to hold the devices and the polycarbonate jig.

An inverted microscope (Nikon Eclipse Ti) was used to record the experiment process with a high pressure mercury lamp as an excitation source with matching

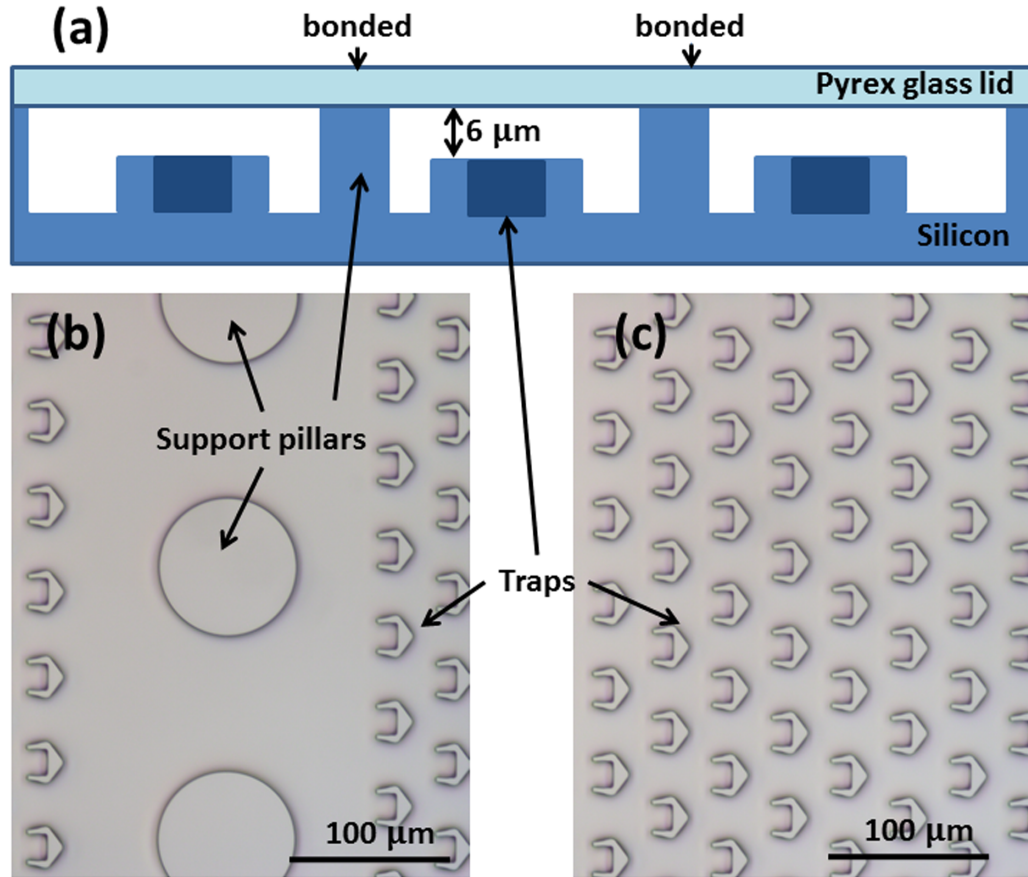
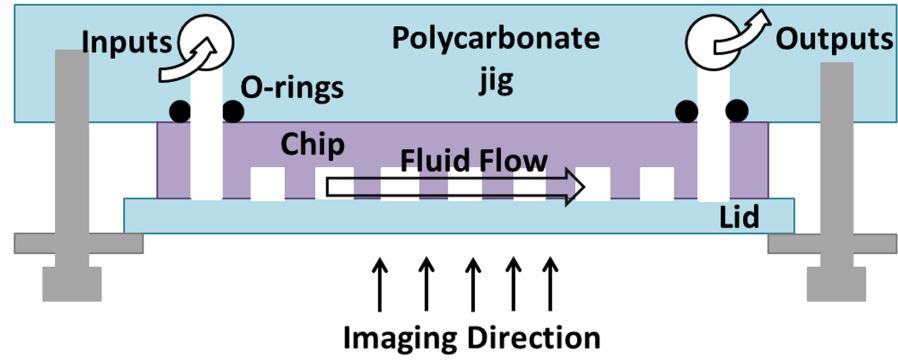


Figure 2.6: (a) Side view schematic of fabricated trap structure with 6  $\mu\text{m}$  critical gap. (b) and (c) micrographs of fabricated trap array using two-step DRIE with support pillars implemented to avoid the deformation of the Pyrex glass lid.

fluorescence filter sets (FITC, 467–498 nm excitation and 513–556 nm emission, and TRITC 532–556 nm excitation and 570–613 nm emission).

Fig. 2.7(b) shows the entire syringe pump and microfluidic system. The system and tubing was first rinsed and wet with degassed 0.2% Pluronic F108 surfactant in deionized water and then the buffer. The syringe pump was running in the range of 0.1  $\mu\text{L}/\text{min}$  to 100  $\mu\text{L}/\text{min}$ . For consistency, an average fluid speed in the array  $v_{avg}$  is used to represent all simulation and experimental results in this thesis, where  $v_{avg}$  is defined as

(a)



(b)

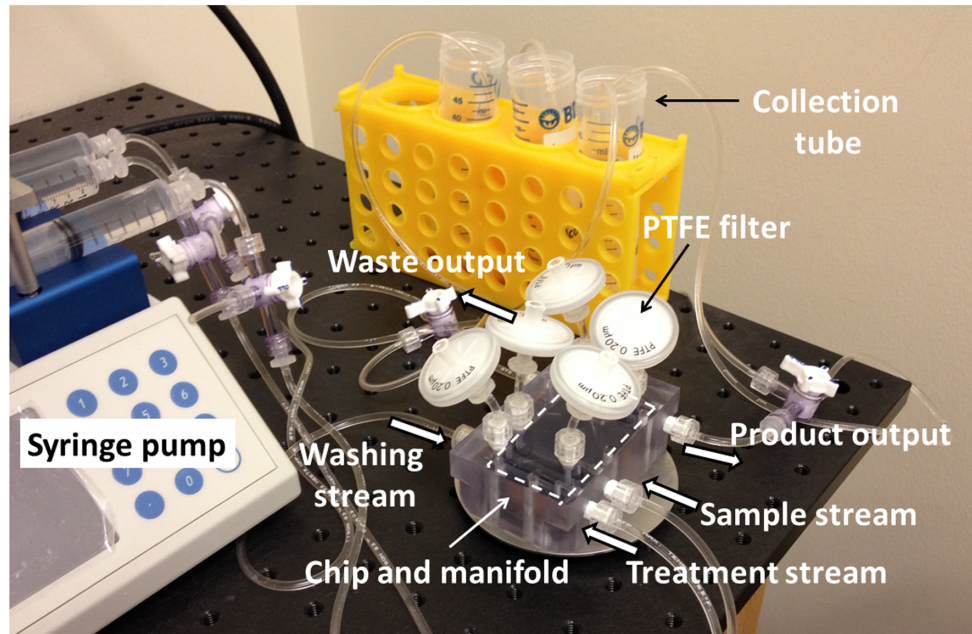


Figure 2.7: (a) Schematic of the manifold setup for an on-chip cell preparation system. (b) Experimental apparatus with device mounted into polycarbonate manifold connected to syringe pump which drives fluid through the device.

$$v_{avg} = \frac{L_{tot}}{\tau_{tot}} = \frac{L_{tot}F}{V_{tot}} \quad (2.4)$$

where  $L_{tot}$  is the total length of the device channel,  $\tau_{tot} = V_{tot}/F$  is the average residence time for the fluid to flow through the device channel,  $F$  is the volume flow

rate of the syringe pump,  $V_{tot} = nL_{tot}W_{tot}H_{tot}\theta$  is the total fluid volume of the device channel,  $n$  is the number of devices used,  $W_{tot}$  and  $H_{tot}$  are the total width and the depth of the device channel respectively, and  $\theta$  is the void fraction, i.e. the fraction of the array volume filled with fluid (i.e. excluding the array of structures).

# Chapter 3

## On-Chip Chemical Processing of Biological Cells Using DLD Arrays

### 3.1 Introduction

In this chapter, we tried to develop a microfluidic system driven by continuous flow for on-chip cell preparation using DLD arrays. The work presented in this chapter was inspired by the device proposed by K. J. Morton, et al. [7] utilizing conventional DLD arrays for on-chip platelet labelling with R6G and on-chip cell lysis. There were no microfluidic structures to control the diffusion of treatment chemical in the conventional DLD arrays, so the diffusion of treatment chemical took place all through the device. Therefore, the conventional DLD arrays required high flow speed to minimize the contamination of treatment chemical at the product output, thus limiting the total on-chip incubation time on the order of 10 – 100 ms. To resolve the trade-off between the requirements of low contamination of treatment chemical and long on-chip incubation time, two approaches were demonstrated with detailed experimental and modelling results in this chapter. The first approach was implementing the “separator walls” to increase the on-chip incubation time and confine the region for the

diffusion of treatment chemicals. The second approach was integrating two DLD arrays connected by a very long serpentine channel. The target cells were harvested at the first DLD array, then on-chip incubated in the very long serpentine channel, and finally washed in the second DLD array to remove most of the treatment chemicals.

## 3.2 Conventional DLD arrays

### 3.2.1 Principle of Operation

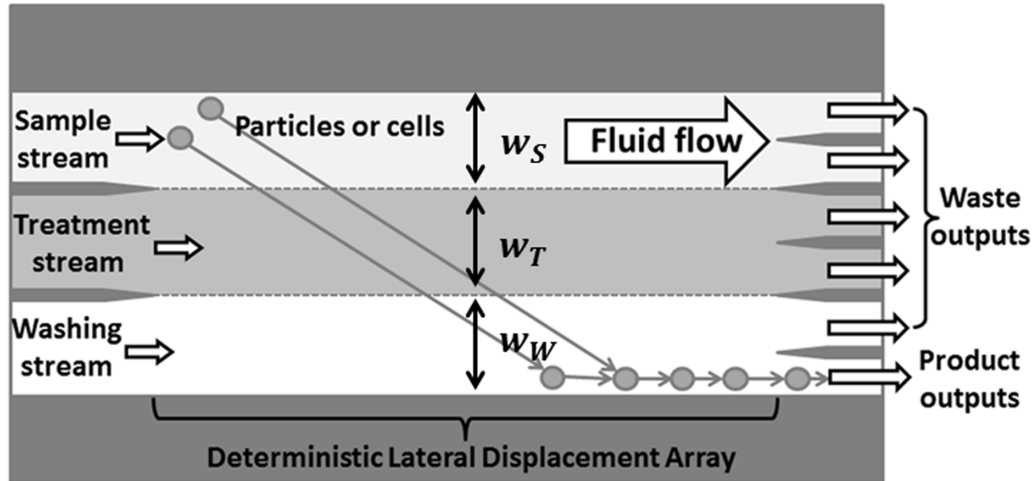


Figure 3.1: Schematic of conventional DLD array for on-chip cell preparation. Three streams driven by continuous flow: sample stream, treatment stream, and washing stream, are loaded to the device. Particles or cells from the sample stream are driven into and then out of the treatment stream to get processed, and are washed in washing stream, to yield the processed and washed cell sample.

K. J. Morton, et al. have presented a method for on-chip cell processing in a continuous-flow microfluidic chip, in which DLD arrays are used to move target cells above the critical size of the array into and then out of a treatment chemical processing stream [7]. On-chip platelet label and wash, and *E. Coli* lysis and chromosomal separation were demonstrated with this approach but not quantified for efficiency. Fig. 3.1 shows the principle of the conventional DLD array for on-chip cell preparation.

Three streams driven by continuous flow (sample stream, treatment stream, and washing stream) are loaded to the device. Particles or cells from the sample stream are driven into and then out of the treatment stream to get processed, and are washed in the washing stream, to yield the processed and washed cell sample. 3- $\mu\text{m}$  beads were directed across a stream of 0.5- $\mu\text{m}$  beads as a demonstration of this approach as shown in Fig. 3.2.

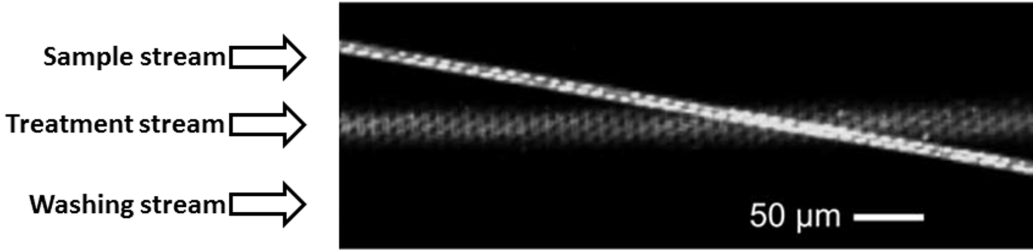


Figure 3.2: Fluorescent image of the trajectory of 3- $\mu\text{m}$  beads crossing over a stream of 0.5- $\mu\text{m}$  beads. The DLD array has 6  $\mu\text{m}$  circular posts, 4  $\mu\text{m}$  gap, migration angle  $\epsilon = 1/5$ , and 2.2  $\mu\text{m}$  critical size. The flow speed ranged from 50–500  $\mu\text{m}/\text{s}$ , with Reynolds number  $Re \ll 1$  and Péclet number  $Pe \gg 1$ . Image courtesy of K. J. Morton, et al. [7].

The diffusion of treatment chemical from the center stream of width  $w_T$  can lead to contamination of the prepared cells if it diffuses to the product output. To minimize contamination, high flow speeds are required, which limits the on-chip incubation time to the range of 10–100 ms. This is too short in nearly all cases for effective on-chip chemical processing for steps such as labelling by monoclonal antibodies and SYTO 13, and lysis which require the incubation time on the order of 5 – 30 min.

### 3.2.2 Device Performance Analysis

The on-chip incubation time for biological cells using conventional DLD array can be calculated as

$$t_{\text{incubate}} = \frac{w_T}{\epsilon v_{\text{avg}}} \tag{3.1}$$

where  $w_T$  is the width of treatment stream,  $v_{avg}$  is the average flow speed in  $y$ -direction, and  $\epsilon v_{avg}$  is approximately the flow speed in  $x$ -direction.

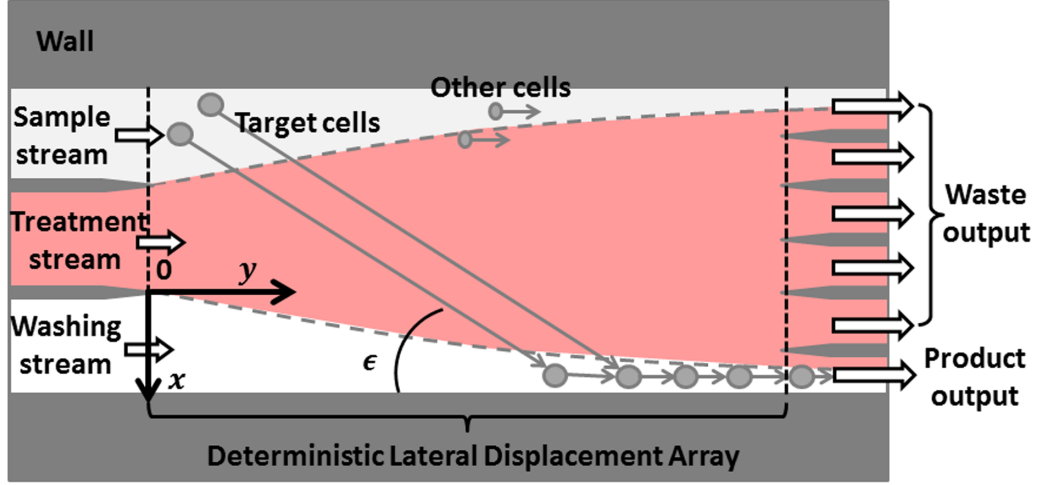


Figure 3.3: The diffusion of treatment chemical from the center treatment stream in conventional DLD array, and the coordinate system setup.

As shown in Fig. 3.3, the diffusion will introduce contamination of treatment chemical to the product output. A numerical model of chemical diffusion in DLD arrays was developed in Section 3.3.3. For a simplified estimation of the concentration of treatment chemical, we here derive a simple analytical model. We assume initially a semi-infinite concentration profile,  $C_o$  for  $x < 0$  and 0 for  $x > 0$  and that the diffusion in the  $x$ -direction can be described by the diffusion equation

$$\frac{\partial C}{\partial t} = D \frac{\partial^2 C}{\partial x^2} \quad (3.2)$$

Assuming a free boundary at the bottom and ignoring the Taylor-Aris dispersion ([48–50] see further discussion in Section 3.3.3), the solution to Eq. 3.2 at the end of the DLD array is

$$\frac{C(x, \tau_{tot})}{C_o} = 1/2(1 - \text{ERF}(\frac{x}{\sqrt{4D\tau_{tot}}})) \quad (3.3)$$

where  $ERF$  is the error function. Some  $x/\sqrt{4D\tau_{tot}}$  for various degrees of concentration at the outputs are presented in Table. 3.1.

Table 3.1:  $x/\sqrt{4D\tau_{tot}}$  for various degrees of concentration at the outputs

$C/C_o$	$x/\sqrt{4D\tau_{tot}}$
$10^{-1}$	0.91
$10^{-2}$	1.65
$10^{-3}$	2.19
$10^{-4}$	2.63

To have a desired level of contamination, for example  $0.01C_o$ , the width of washing stream  $w_W$  should be larger than  $1.65\sqrt{4D\tau_{tot}}$ , where  $\tau_{tot} = L_{tot}/v_{avg}$  is the total time for particles or cells to flow through the device. Therefore, the lower limit of flow speed can be written as

$$v_{avg} > \frac{10.9DL_{tot}}{w_W^2} \quad (3.4)$$

Bring Eq. 3.4 to Eq. 3.1, we can obtain the higher limit of incubation time that can be achieved in conventional DLD array as

$$t_{incubate} < \frac{w_T w_W^2}{10.9\epsilon DL_{tot}} \quad (3.5)$$

In this thesis, we focus on the applications for on-chip human blood cell preparation, such as isolation and labelling. Table 3.2 shows the highest incubation time calculated using Eq. 3.5 under different conditions.

The diffusion constant of  $D = 10^{-9} \text{ m}^2/\text{s}$  is close to that of R6G, ethanol, methanol, and 1-2 orders of magnitude higher than that of monoclonal antibodies [51], all commonly used in chemical and biological treatment for biological cells, such as leukocyte from human blood.  $\epsilon = 1/42$  is a typical migration value for cells larger than  $7 \mu\text{m}$ . The total length of the device is often set to be very long to effectively

Table 3.2: Incubation time can be achieved using conventional DLD arrays at different conditions

$D = 10^{-9} \text{ m}^2/\text{s}$ and $\epsilon = 1/42$			
$w_T$ ( $\mu\text{m}$ )	$w_W$ ( $\mu\text{m}$ )	$L_{tot}$ (cm)	Incubation time (ms)
50	50	3	16.1
50	100	3	64.3
100	200	3	514.2
200	200	3	1028.5
300	300	3	3471.1

concentrate the target cells due to the deformation of cells and cell-to-cell interaction which makes the target cells not always be displaced by the posts. From the calculation presented in Table. 3.2, the on-chip incubation time is in the range of 10 ms to 3.5 s for conventional DLD array. In reality, the boundary of microfluidic confinements—the boundary wall will take effect in the diffusion of treatment chemical. Because the presence of the boundary wall will block the treatment chemical to diffuse away from the device region, the contamination level of treatment chemical at the product output might be higher than that estimated using the simple approach discussed above especially when the diffusion constant of treatment chemical is high, such as R6G (experimental results in Section 3.3). Thus, the on-chip incubation time for on-chip cell preparation using conventional DLD arrays is in the order of  $\sim 100$  ms for on-chip leukocyte labelling R6G and SYTO 13 applications (see Section 3.3).

### 3.3 DLD Arrays with Separator Walls

#### 3.3.1 Principle of Operation

To achieve both long incubation time and low contamination of the excess treatment chemical, “separator walls” were introduced to increase the on-chip incubation time

and to improve the quality of washing. Cells of interest were concentrated into a treatment stream of chemical reagents at the first separator wall for extended on-chip incubation without causing excess contamination at the output due to diffusion of the unreacted treatment chemicals, and then were directed to the washing stream before final collections. The second separator wall further reduced the output contamination from diffusion to the washing stream. With this approach, we demonstrated a three-input (sample stream, treatment stream, and washing stream) microfluidic device for on-chip leukocyte staining with Rhodamine 6G (R6G, 20  $\mu\text{g}/\text{L}$ ) and washing with little output contamination. R6G molecules are commonly used staining dye in biological analysis [52–55] and have diffusion constant of  $4 \times 10^{-10} \text{ m}^2/\text{s}$  in water, close to that of ethanol, methanol, and 1-2 orders of magnitude higher than that of monoclonal antibodies [51, 56, 57], all commonly used in chemical and biological treatment.

### 3.3.2 Device Design

Fig. 3.4 demonstrates the proposed “wall-separated” DLD array design. The input consists of three streams: a sample stream (diluted blood in our experiments), a treatment stream (such as staining chemicals), and a washing stream (such as bovine serum albumin (BSA) buffer). The output consists of two streams: the product of treated and washed cells, and waste. In the central region, there is a DLD array consisting of an array of posts slightly tilted by a small angle  $\epsilon$  from the average flow direction imposed by the walls. Cells smaller than a critical size  $D_C$  will follow the stream waving around the posts in an average horizontal direction. Cells larger than this critical size will follow the axis of the post array, “bumping” off of the post in each column. The large cells move into the treatment stream to be treated and then out of the treatment stream to be washed and collected as product output (Fig. 3.4) [7].

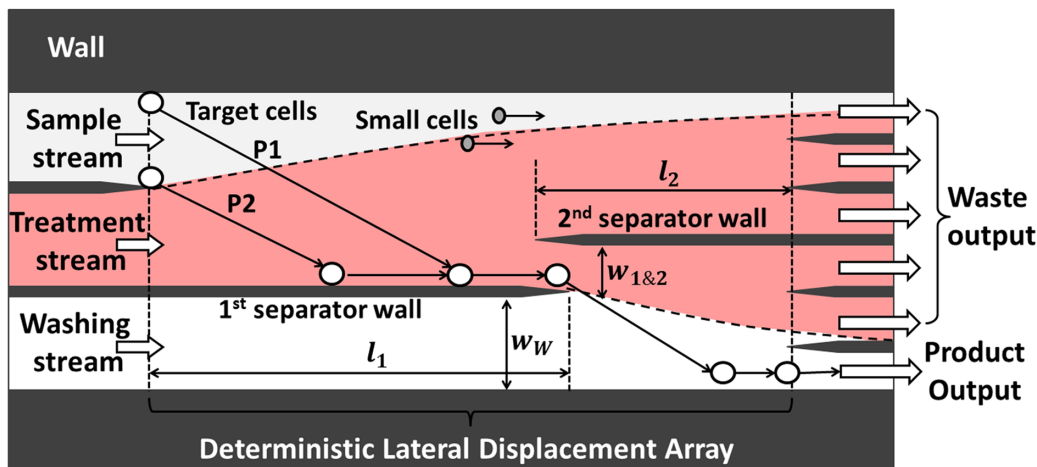


Figure 3.4: The schematic of the the wall-separated DLD array design for on-chip cell chemical processing and washing. Target cells (following paths P1 and P2) are processed and washed in a continuous fluidic flow. Separator walls reduce the diffusion of the treatment chemical, indicated by red shading, to minimize the contamination in the product output.

The innovations of this work are the “separator walls”. A first wall prevents any chemical diffusion (indicated by red shading in Fig. 3.4(a)) towards the output, while the cells are being incubated. The target cells or particles are concentrated at the first separator wall of length  $l_1 = 2$  cm, and then they are directed into the washing stream. After the first separator wall, target cells will be bumped by the DLD array and driven into and across the washing stream to be collected. The treatment stream is now free to diffuse to the product output, and the diffusion into the chip output is constrained only to this region, while the conventional DLD array has diffusion to the product output occurring all across the whole array (as shown in Fig. 3.1). The treatment chemical has shorter diffusion time in the “wall-separated” DLD array than that in conventional DLD array. The diffusion in this last region can again be suppressed by adding a second separator wall, of length  $l_2 = 1$  cm in the current design. The second separator wall reduces a portion of the chemical reagents from being able to diffuse towards the output channel. The gap ( $w_{1\&2}$ ) between the first and second separator walls is  $90 \mu\text{m}$ , which should be as small as possible to avoid

treatment chemical reaching to the washing stream, but should be larger enough to avoid the clogging of target cells.

Fig. 3.5 shows the detailed design of DLD array with separator walls created using L-edit software. The 120  $\mu\text{m}$  to 150  $\mu\text{m}$  deep DLD array has circular posts of  $S = 18 \mu\text{m}$  diameter spherical posts,  $G = 18 \mu\text{m}$  gap between the posts, and  $\epsilon = 1.36^\circ$  ( $1/42$ ), which gives a critical size ( $D_C$ ) about 6  $\mu\text{m}$  [27]. The wall edges of the DLD array are designed according to Inglis' guidelines, with a periodically varying gap between wall and posts, but which is always larger than the cell size to avoid clogging [58].

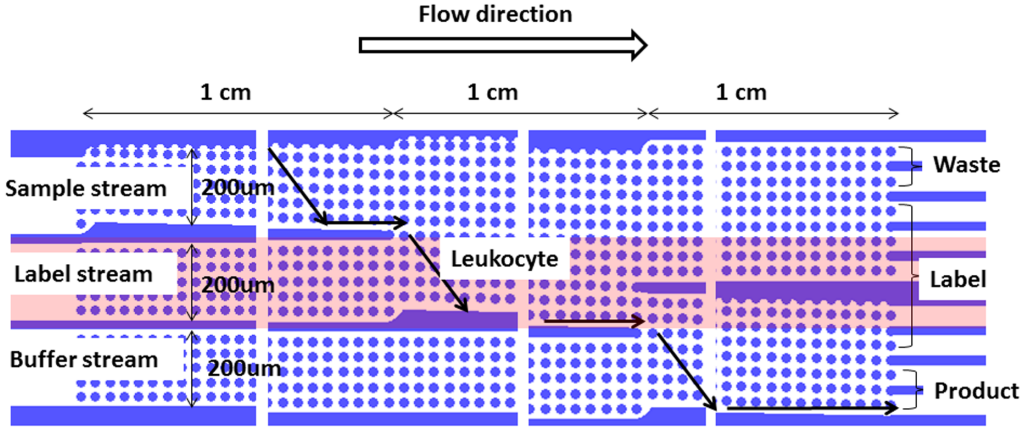


Figure 3.5: The design of DLD array with separator walls created using L-edit software. The 120  $\mu\text{m}$  to 150  $\mu\text{m}$  deep DLD array has circular post of 18  $\mu\text{m}$  diameter, and 18  $\mu\text{m}$  gap between the posts, and migration angle  $\epsilon = 1.36^\circ$  ( $1/42$ ), which gives a  $\sim 6 \mu\text{m}$  critical size.

We first tested the device with 10- $\mu\text{m}$  and 0.2- $\mu\text{m}$  beads. Fig. 3.6 shows the fluorescent beads flowing DLD array with separator walls at the input, middle, and output regions at an average flow speed of 425  $\mu\text{m}/\text{s}$ . The 10- $\mu\text{m}$  beads were first concentrated to the first separator wall, while the 0.2- $\mu\text{m}$  beads flowed directly to the waste output. After the first separator wall, the 10- $\mu\text{m}$  beads were driven to the product output to be collected.

We also tested conventional DLD arrays using 10- and 0.2- $\mu\text{m}$  beads. Fig. 3.7 displays the fake color composites of fluorescent beads flowing at the outputs of (a)



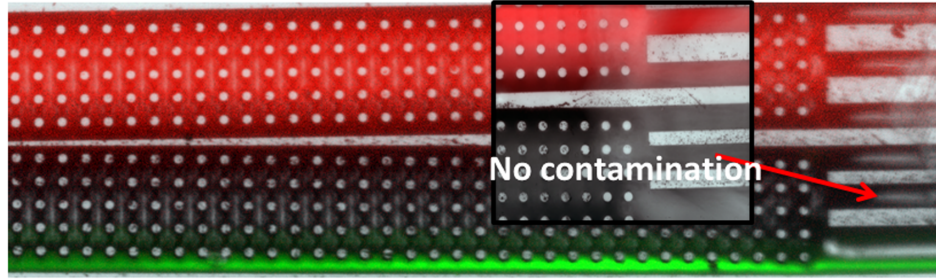
Figure 3.6: Fake color composites of fluorescent beads flowing at  $425 \mu\text{m/s}$  in DLD array with separator walls at the input, middle, and output regions.  $10\text{-}\mu\text{m}$  beads: green.  $0.2\text{-}\mu\text{m}$  beads: red.

DLD array with separator walls, and (b) conventional DLD array at an average flow speed of  $425 \mu\text{m/s}$ . Though the diffusion constant of  $0.2\text{-}\mu\text{m}$  beads is about  $\sim 10^{-12} \text{m}^2/\text{s}$ , which is about 2 orders of magnitude smaller than that of R6G, we can still observe the fluorescence intensity of  $0.2\text{-}\mu\text{m}$  beads at the output channel next to the product output channel as shown in Fig. 3.7.

### 3.3.3 Modelling of Diffusion of Treatment Chemical

The diffusion of the treatment chemical in the  $x$ -direction, defined as perpendicular to the average flow direction ( $y$ -direction, see Fig. 3.8(a)), is critical issue for the quality of prepared cells, since it will cause the contamination of the “washed” product output by the treatment chemical. There are two major factors that may complicate such

**(a) DLD array with separator walls**



**(b) Conventional DLD array**

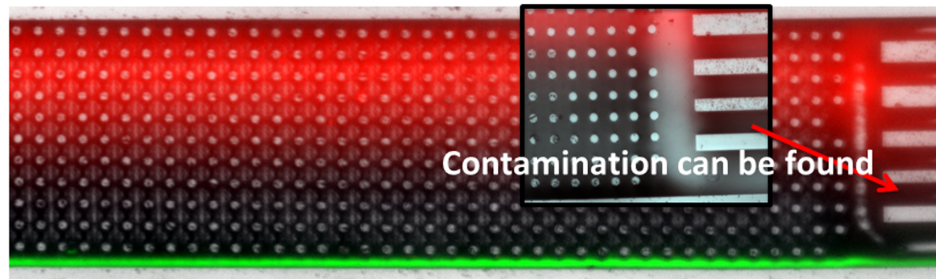


Figure 3.7: Fake color composites of fluorescent beads flowing at  $425 \mu\text{m/s}$  at the outputs of (a) DLD array with separator walls, and (b) conventional DLD array.  $10\text{-}\mu\text{m}$  beads: green.  $0.2\text{-}\mu\text{m}$  beads: red.

diffusion in the devices described: (1) Taylor-Aris dispersion and (2) the effect of the posts' boundaries. Taylor-Aris dispersion along the flow direction occurs because different streamlines in microstructures can move at different velocities. However, the average flow is along the  $y$ -direction in the DLD array. There is no net fluid flow in the  $x$ -direction and the local  $x$ -direction flow has very low flow speed [27]. Thus, classic Taylor-Aris dispersion can be effectively neglected in the  $x$ -direction [59].

The posts can suppress long-range diffusion of the treatment chemical through geometric confinement. Stochastically, for diffusion over a length scale greater than that of the post gap and gap periodicity, the diffusion of the treatment chemical in the treatment chemical in the post array can be modelled as a diffusion process with an effective diffusion constant  $D_{eff}$  in a structure without posts. When the size of the diffusing species is less than 0.1 that of the gap spacing, this  $D_{eff}$  has been measured in micropost arrays to be  $\eta D_o$ , where  $D_o$  is the diffusion constant without posts [60].

These criteria are valid for the experiments, where the size of the R6G molecule is about 1.6 nm [61] versus the post gap of 18  $\mu\text{m}$ . Given  $\eta \approx 0.80$  measured in the experiments,  $D_{eff}$  for R6G can be assumed to be  $0.80D_{R6G}$ .

To validate this effective diffusion constant, we modelled diffusion (using COMSOL numerical modelling software) from a central stream with uniform chemical concentration entering a DLD array as used in the experimental work (post diameter and gap are 18  $\mu\text{m}$ , with migration angle  $\epsilon = 1.36^\circ$ ) over one central gap of 18  $\mu\text{m}$ . The diffusion was modelled in 2-D over an array length of only 378  $\mu\text{m}$  due to practical grid limitations of COMSOL. The central stream was surrounded on top and bottom by buffer streams (chemical concentration of zero) at the input with the same flow rate per unit width. The diffusion constant of the treatment chemical is set to be  $4 \times 10^{-10}$   $\text{m}^2/\text{s}$  (the diffusion constant of R6G,  $D_{R6G}$ , which is later utilized in experiments). The figure at the left in Fig. 3.8(a) shows the simulated contour plot of the relative concentration (the ratio of the concentration of the treatment chemical to that in the input chemical stream) in a part of the DLD array with average flow speed of 25  $\mu\text{m}/\text{s}$ . The average time  $\tau$  for fluid to flow through the modelled volume is 15.1 s.

The relative concentration profile at the right boundary along the  $x$ -direction of simulation with posts (378  $\mu\text{m}$  after the input) is drawn in Fig. 3.8(b) with a red solid line. To extract an effective long-range diffusion constant, reflecting the effects of confinement, this curve was then fit with a 1-D numerical solution the diffusion equation for the same initial profile, time  $\tau = 15.1$  s, neglecting the effect of the posts, with  $D_{eff}$  as an adjustable parameter. This is shown as a blue solid line in Fig. 3.8(b):  $D_{eff} = 3.2 \times 10^{-10}$   $\text{m}^2/\text{s}$  was found to give the best fit. Because the diffusion length  $L_D = \sqrt{D_{eff}\tau} \approx 69.6$   $\mu\text{m}$  is well over the array period,  $D_{eff}$  should be valid for modelling long range diffusion. Note that the  $D_{eff}/D_{R6G}$  ratio of 0.80 is equal to the void fraction, as predicted above.

For modelling diffusion from the central treatment stream to the output channel in our actual devices, we used COMSOL to incorporate the blocking effects of the separator and outer walls. However, the complete post microstructure cannot be included because of grid size limitations, so we modelled the device without posts with the  $D_{eff}$  extracted above. We also increased the input flow rate by 20%, to compensate for the zero void fraction to give the same residence time and average flow speed as with posts. Because the flow rate in all gaps across the flow stream in the device array is the same, in the simulations with no posts we also used a “slip” wall boundary condition, so that the flow rate across the entire modelled region is the same. Fig. 3.8(a) and (b) also demonstrate the results of this simulation, showing good profile agreement over long distance with the modelling using the complete microstructure. Therefore, for the rest of this chapter, to model diffusion to the product output, COMSOL was used in a structure with no posts using  $D_{eff} = 0.80D_{RG}$ .

### 3.3.4 Diffusion of Treatment Chemical to Product Output

Simulation results of the relative concentration of the treatment chemical for devices with no separator wall, one separator wall, and two separator walls using COMSOL are shown in Fig. 3.9. The relative concentration of the treatment chemical is shown at the chip input, middle of the chip, and the chip output. The reduction of treatment chemical contamination at the product output brought by the first and second separator walls can be seen clearly from these simulation results. At average flow speed of  $100 \mu\text{m/s}$  for the design with only the first separator wall (Fig. 3.9(a)), the treatment chemical is blocked by the first separator wall, but still has enough time in the last section of the chip to diffuse unboundedly across the entire flow path, so that the 1-wall design is little better than the conventional no wall design. The contamination in the product output is calculated as the average relative concentration of the treatment chemical over the  $60\text{-}\mu\text{m}$ -wide product output channel. By implementing

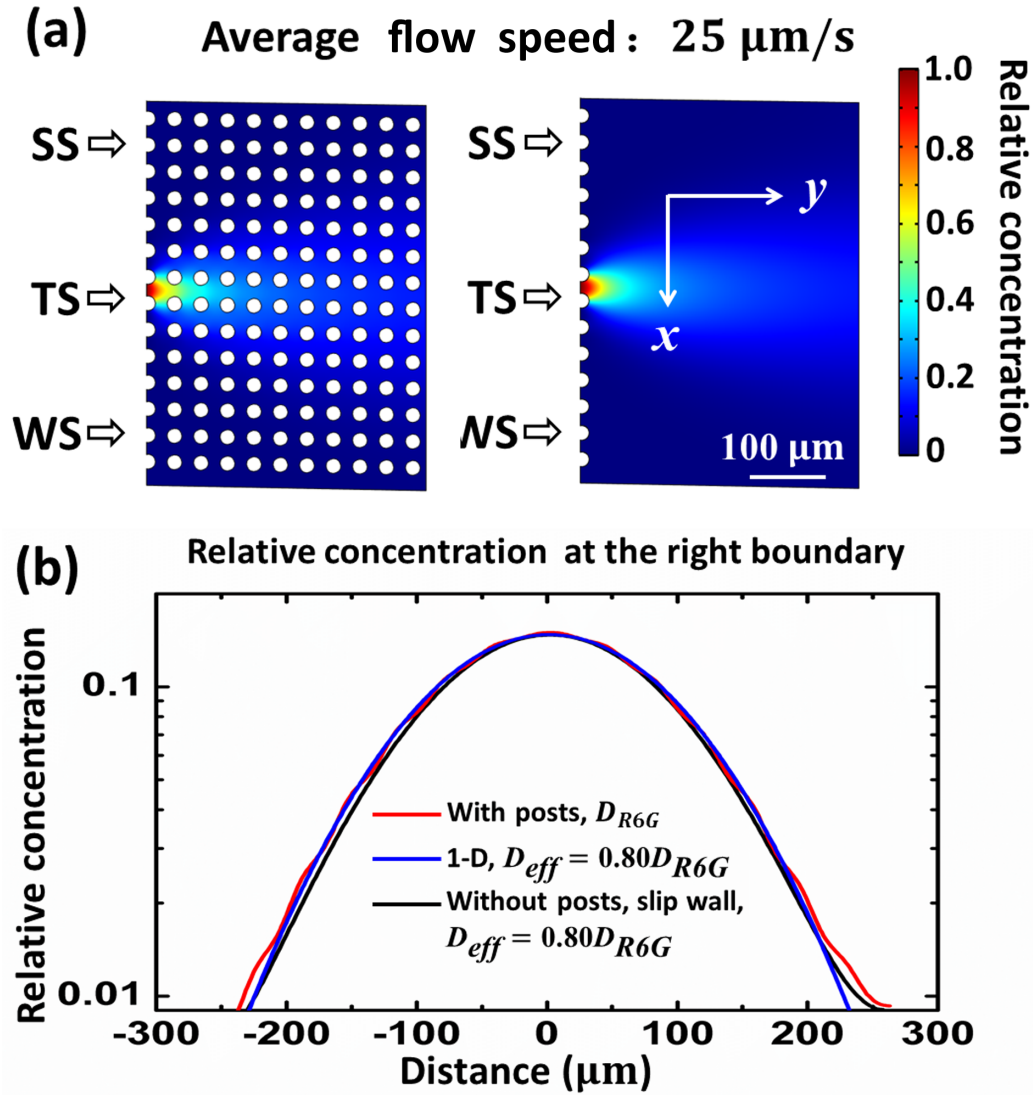


Figure 3.8: COMSOL simulations of relative concentration in channels with and without posts. SS: sample input stream, TS: treatment input stream, and WS: washing input stream. Post and gap are  $18 \mu\text{m}$ . (a) Relative concentration distribution and (b) relative concentration profile at the right boundary along  $x$ -direction at average flow speed of  $25 \mu\text{m/s}$ . “With posts” and “without posts” refer to COMSOL results using  $D_{R6G}$  and  $D_{eff} = 0.80D_{R6G}$ , respectively. “1-D” refers to a 1-D numerical solution using the same  $D_{eff}$ .

the second separator wall, this relative contamination can be reduced from 0.31 down to 0.14. With the average fluid speed of  $1 \text{ cm/s}$  (Fig. 3.9(b)), the diffusion time is reduced, but the conventional design still has an output contamination of relative

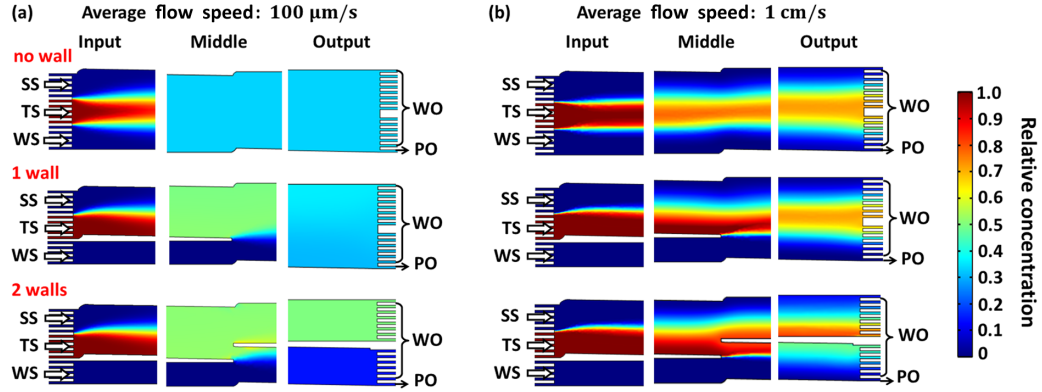


Figure 3.9: 2-D COMSOL simulations of relative concentration across devices with no separator wall, one separator wall, and two separator walls at average flow speed  $100 \mu\text{m/s}$  and  $1 \text{ cm/s}$ . WO: waste output and PO: product output. Each condition shows the input, middle, and output regions (0.8 mm long) of the devices. For  $100 \mu\text{m/s}$  ( $1 \text{ cm/s}$ ), the relative output contamination is 0.33 (0.081), 0.31 (0.022), and 0.14 (0.008) with no, 1, and 2 separator walls, respectively. The output contamination of the treatment chemical can be reduced effectively with the separator wall design.

concentration about 0.081. The output contamination is suppressed 4-fold with the first separator wall design and can be further reduced utilizing two separator walls down to 0.008, a 10-fold improvement over the design without separator walls.

We also experimentally measured the diffusion of R6G ( $20 \mu\text{g/L}$ ) in the fabricated arrays without and with separator walls by quantitative fluorescence microscopy. Similar to the simulation results, the output contamination due to the diffusion of R6G was evaluated by the average relative R6G concentration entering the product output. The relative R6G concentration is defined as the ratio of the fluorescence intensity of R6G to that of the treatment stream input, as the fluorescence intensity of R6G has a linear relation to its concentration at low concentration [62]. Fig. 3.10(a) and (b) display the fluorescence images of the input, middle, output region of DLD arrays without and with separator walls of same length, but with otherwise identical dimensions. At average flow speed  $0.86 \text{ mm/s}$ , the contamination at the product output almost reaches saturated level about 0.3 in the conventional DLD array (Fig. 3.10(a)).

In the wall-separated array, the presence of separator walls leads to a 3 fold output contamination reduction down to about 0.1 (Fig. 3.10(b)).

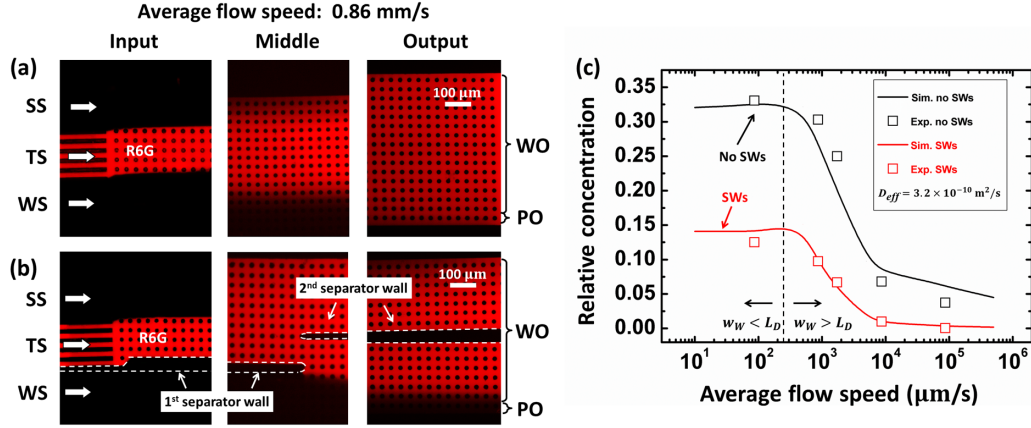


Figure 3.10: Fluorescent images of R6G flowing in the treatment stream of (a) conventional DLD array and (b) DLD array with two separator walls, showing clear reduction of contamination at the product output. The average flow speed is 0.86 mm/s. (c) Experimental and COMSOL simulation results of relative concentration versus average flow speed for both conventional (black) and wall-separated (red) DLD arrays. The open squares are experiment results measured as the ratio of the fluorescence intensity at the product output to that of the treatment stream input. The solid lines are the COMSOL simulation results. A dotted black line is drawn in (c) to point out the critical flow speed of 240  $\mu\text{m/s}$  for the conventional design. R6G concentration is 20  $\mu\text{g/mL}$ .

The experiment results at different flow velocities agree well with the numerical simulation, as shown in Fig. 3.10(c). The output contamination depends on how fast the diffusion of the treatment chemical occurs compared to the rate at which the fluid moves through the device, classically characterized by Péclet number. For a device without separator walls, a critical speed ( $v_c$ ) will be the one which the diffusion length  $L_D = \sqrt{D_{eff}\tau}$  is equal to the distance from the treatment stream to the product output location, which is  $w_W$ , the width of the washing stream, where  $\tau = L_{tot}/v_c$  is the time the fluid is in the device. Thus, a critical flow speed can be written as

$$v_c = \frac{D_{eff}L_{tot}}{w_W^2} \quad (3.6)$$

For a conventional DLD array, a vertical black dotted line in Fig. 3.10(c) indicates this critical flow speed of  $240 \mu\text{m/s}$ . At flow speed lower than  $v_c$ ,  $w_W < L_D$  and the contamination reaches a plateau. At flow speed higher than  $v_c$ ,  $w_W > L_D$  and the contamination drops.

For the “wall-separated” DLD array, the time for diffusion in the device is reduced from  $(l_1 + l_2)/v$  to  $l_2/v$ , where  $v$  is the average flow speed, and the second separator wall in the latte region of the device further prevents some treatment chemical from being able to move to the output. The improvement in the output contamination reduction is 3 to 10 fold, depending on the flow speed (Fig. 3.10(c)). For example, from the experimental results, at average flow speed  $8.6 \text{ mm/s}$ , the R6G concentration in the product output channel can be reduced from 0.07 without separator walls to only 0.01 with the implementation of separator walls.

### 3.3.5 Incubation time vs. output contamination

The incubation time is a key factor of on-chip cell processing and preparation applications. We now estimate the lower bound to the incubation time in the “wall-separated” DLD array. The cells flowing into the device at the topmost boundary will experience the minimum incubation time (P1 in Fig. 3.4(a)). The incubation time  $t_{inc}$  in the wall-separated DLD array can be estimated as

$$t_{inc} \approx \frac{w_T}{\epsilon v_{cell,DLD}} + \frac{\epsilon l_1 - w_T - w_S}{\epsilon v_{max,post-wall}} \quad (3.7)$$

where  $w_T$  and  $w_S$  are the widths of treatment stream and sample stream, respectively,  $v_{cell,DLD}$  is the cell speed in the DLD array, and  $v_{max,post-wall}$  is the maximum fluid velocity between the posts and the confining wall. When the target cells flow in the DLD array, their velocity will change periodically from fast in the gaps to slow in the open regions. To estimate the incubation time, we conservatively use the cell flow

speed in post gaps. The average flow velocity ( $v_{avg,post-post}$ ) in post gaps is about 1.62 times the average flow speed in the DLD array for the proposed geometry. The target cells which are above the critical size and thus are “bumped” by the posts at every column of obstacles will move alongside the posts as they follow the tilt angle (target cell in Fig. 3.4(b)). Assuming the large target cell moves at the flow speed of the streamline where the cell center is and a parabolic flow profile, the cell’s speed is  $v_{cell,DLD} \approx 4v_{max,post-post}(r_{cell}/g - r_{cell}^2/g^2)$ , where  $r_{cell}$  is the radius of the target cells ( $r_{cell}$  of  $3.5 \mu\text{m}$  is assumed for leukocytes), and  $v_{max,post-post} = 3/2v_{avg,post-post}$  is the maximum flow speed in the post gaps [27].

The second term of Eq. 3.7 is the additional incubation time gained by implementing the first separator wall. The incubation time can be increased by increasing the total length of the first separator wall without any penalty of the contamination of the treatment chemical in the product output. As the target cell further moves along the first separator wall, it will be driven to an equilibrium position where the wall effect lift force and the shear gradient lift force balance [63–67]. From experimental observations, the equilibrium position of leukocytes is close to the middle of the gap between the wall and the posts, where the flow speed reaches an average maximum ( $v_{max,post-post}$ ) (Fig. 3.4(b)). By design, the average  $v_{max,post-wall}$  is approximately equal to  $v_{max,post-post}$  discussed above.

Experimental and COMSOL simulation results of the relative output contamination versus calculated incubation time according to Eq. 3.7 for both conventional (black) and “wall-separated” (red) DLD arrays are shown in Fig. 3.11. For high flow speed, both incubation time and output contamination are low. They both rise as the flow speed is decreased. For a leukocyte staining test, average flow speed of  $1.7 \text{ mm/s}$  is selected (pointed out by the red dash lines) as an experimental on-chip leukocyte staining condition, with 4 s incubation time and 0.067 product output contamination relative to the concentration of the treatment chemical input. As can be seen from the

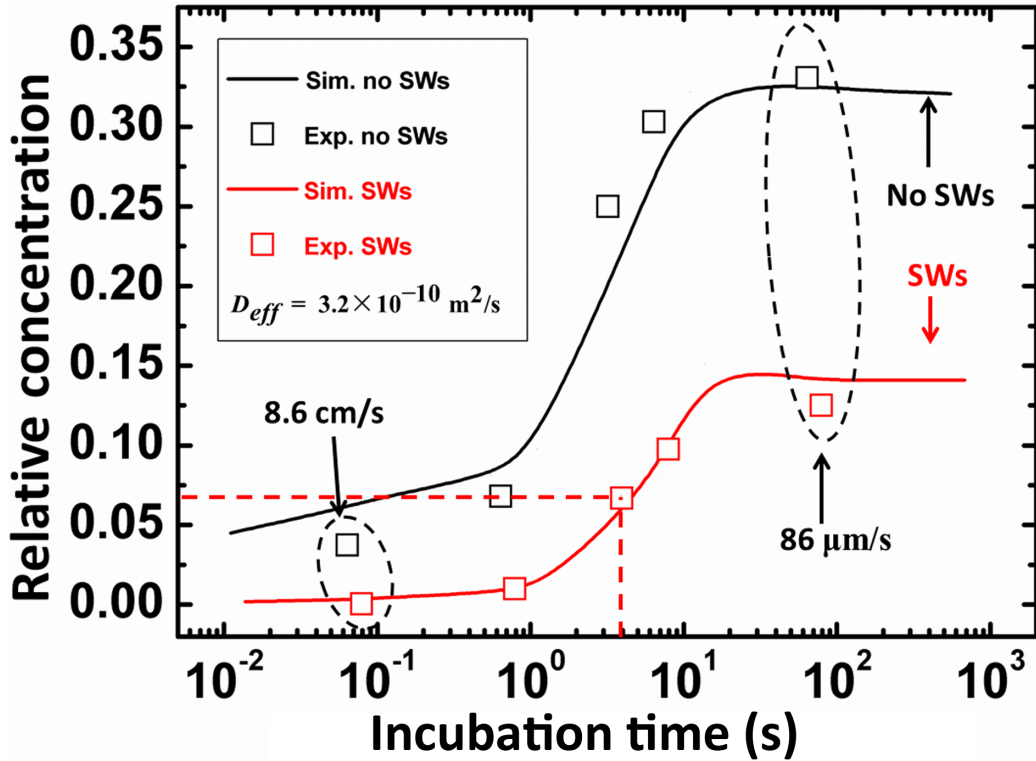


Figure 3.11: Experimental and COMSOL simulation results of relative concentration of R6G versus calculated incubation time for both conventional (black) and wall-separated (red) DLD arrays, achieved by varying the average flow speed. Qualitatively, a “good” result from an application point of view is to the lower right of the figure (low output contamination and long on-chip incubation time). The open squares are experimental results and the solid lines are the solid lines are the COMSOL simulation results. The condition for the two-separator wall design of an average flow speed of 1.7 mm/s with 4 s incubation time and 0.067 product output contamination (indicated by red dotted lines) was selected for sub-sequential staining tests.

later experiments, leukocytes can be stained with recognizable fluorescence intensity compared to very low background intensity of contamination at this condition.

We then used the wall-separated device to demonstrate on-chip staining and washing of leukocytes with R6G (20  $\mu\text{g}/\text{L}$ ), using diluted whole blood as the sample stream input. For details of the blood sample preparation procedure, see Appendix C. R6G diffuses into the cells and attaches to their mitochondria [51]. The array separates the leukocytes out of the sample stream and then directs them into the treatment

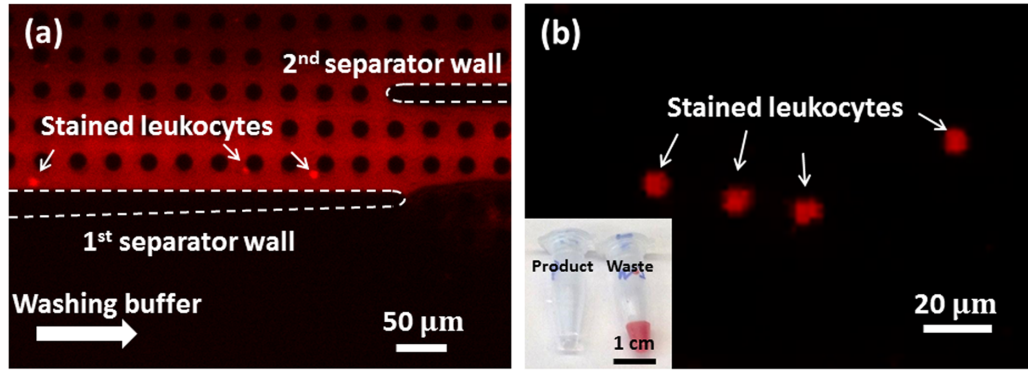


Figure 3.12: Fluorescent images of on-chip leukocyte staining with R6G with wall-separated DLD arrays using diluted human blood as the input, without any centrifugation or lysis. The average flow speed is 1.7 mm/s. View (a) shows middle region of the wall-separated DLD array where the leukocytes are passing through R6G stream and close to entering into the washing stream. View (b) shows labelled leukocytes in the output channel with negligible fluorescence background. The inset of (b) shows vials of collected product and waste outputs, showing low red blood cell level in the product.

and sub-sequential washing streams. The critical size ( $D_C$ ) is about  $6 \mu\text{m}$  in the proposed DLD array measured by fluorescent beads of different sizes, which is below the size of most leukocytes. The diameter of erythrocytes is about  $6\text{--}8 \mu\text{m}$ . However, since their distinctive biconcave shape, they align to the fluid flow to behave as small particles and are not displaced in the array, thus following the average flow direction [68–70]. Moreover, the size of the other content (platelets, proteins, etc.) of blood is mostly smaller than  $6 \mu\text{m}$ , so that only leukocytes are harvested from the sample stream. Fluorescent microscopy was used to track the paths and staining of the cells (Fig. 3.12). In the input region, no fluorescent leukocytes or other cells could be seen as the cells were not yet labelled. The leukocytes were then concentrated and incubated along the first separator wall in the middle region of the wall-separated DLD array (Fig. 3.12(a)). Finally, the labelled leukocytes are collected the product output and clearly visible (Fig. 3.12(b)). The inset of Fig. 3.12(b) shows the product output and waste output vials from one experiment of  $200 \mu\text{L}$  diluted blood. The notable

color difference suggests a good separation of leukocytes from erythrocytes. In the fluorescence image of the product output stream, little fluorescence background could be found, indicating a good staining by R6G and low contamination of unreacted R6G in the product output.

### **3.3.6 Summary of DLD Arrays with Separator Walls**

A wall-separated DLD array for integrated on-chip cell harvesting, chemical processing, and washing. The “wall-separated” design greatly improves the trade-off between long chemical treatment times and low output contamination at low flow speed, enabling both (i) increased incubation time (4 s at 1.7 mm/s flow speed and  $\sim 10^1$  times increase of the conventional DLD array without separator walls) and (ii) less contamination of treatment chemical in the product output ( $\sim 0.07$  at 1.7 mm/s flow speed and  $\sim 10^1$  times reduction than the conventional DLD array without separator walls). The first wall prevents chemical diffusion towards the output, while the cells are being incubated. The second separator wall further reduces the chemical diffusion, especially at low flow speed. Leukocytes can be separated from the whole blood, stained by R6G, and washed in a single wall-separated DLD array without any pre-processing of the blood or manual handling between steps.

## **3.4 DLD Arrays with Long Serpentine Channels**

### **3.4.1 Principle of Operation**

DLD arrays with separator walls implemented can provide more on-chip incubation time on the order of 10s and less contamination level of treatment chemical to the prepared cell samples with the same geometry (total width, length, post diameter, gap, etc.) as conventional DLD arrays. However, the increased incubation time is still not suitable for preparation applications that require very long processing time (10–30

min) [14, 15]. To have long enough on-chip incubation time and less contamination of treatment chemical, we introduced long serpentine channels to the DLD arrays.

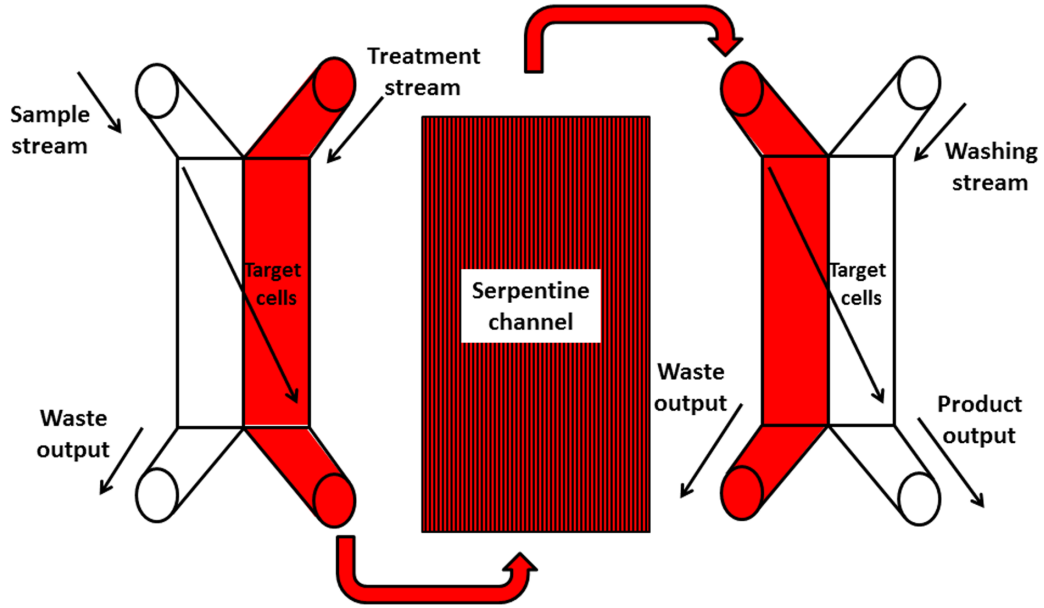


Figure 3.13: Schematic of DLD arrays with a very long serpentine channel for on-chip incubation. Two DLD arrays and one serpentine channel are integrated together. The first DLD array harvests the target cells and directs them to a very long serpentine channel to be processed by a treatment stream. The second DLD array drives the target cells out of from the mixture of treatment chemicals and target cells, and then into a clean washing stream, to yield the processed and washed target cells.

Fig. 3.13 shows the schematic of the proposed device. Two DLD arrays and one serpentine channel are integrated together. A first DLD array harvests and concentrates the target cells from the sample stream and directs them into a treatment chemical processing stream. The concentrated incubation mixture of treatment chemical and cells feeds into the very long serpentine channel for a long incubation time. A final washing step is performed in a second DLD array, which moves the cells from the incubation mixture into a clean buffer for the output product. The long serpentine channel enables long incubation time and reasonably high flow rates to achieve low contamination of the output (processed and washed leukocytes) by the treatment chemical. In this chapter, we first discussed the design and the fluidic control of the

proposed device, and then presented on-chip leukocyte labelling with R6G using this approach as a demonstration

### 3.4.2 Device Design

The first challenge is the decreased recovery efficiency of target cells. The loss of target cells can be attributed to: 1. clogging of target cells in the DLD array [71]; 2. deformation of target cells such that their size smaller than the critical size; and 3. non-optimized device design such that the critical size is larger than the small target cells. For a device of one type of DLD array and optimized post design,  $\sim 80\%$  recovery efficiency of target cells be achieved [72]. Thus,  $\sim 60\%$  of target cells can be retrieved after running through two cascaded DLD arrays. The recovery efficiency is down by 20%.

For higher recovery efficiency of target cells, 3-zone DLD array was utilized, which has recovery efficiency  $\sim 99\%$  for leukocyte applications [73]. Fig. 3.14(a) demonstrates the fabricated symmetric 3-zone DLD array using conventional microfabrication techniques. The array is 120  $\mu\text{m}$  deep, 1.8 mm wide (0.89 mm wide for one-side array), and 3.71 cm long. Array 1 is 1.22 cm long with  $S_1 = 28 \mu\text{m}$  diameter circular posts,  $G_1 = 17 \mu\text{m}$  gaps, migration  $\epsilon_1 = 1/10$ , which gives a critical size about 7.9  $\mu\text{m}$ . Array 2 is 1.11 cm long with  $S_2 = 19 \mu\text{m}$  diameter circular posts,  $G_2 = 11 \mu\text{m}$  gaps, migration  $\epsilon_2 = 1/10$ , which gives a critical size about 5.1  $\mu\text{m}$ . Array 3 is 1.38 cm long with  $S_3 = 12 \mu\text{m}$  diameter circular posts,  $G_3 = 8 \mu\text{m}$  gaps, migration  $\epsilon_3 = 1/10$ , which gives a critical size about 3.7  $\mu\text{m}$ . Leukocytes larger than 7.9, 5.1 and 3.7  $\mu\text{m}$  will be concentrated in the central channel in Array 1, 2, and 3 respectively. The central channel is a channel of 20  $\mu\text{m}$  width to avoid clogging of leukocytes in the sub-sequential arrays. We tested the 3-zone DLD array with SYTO 13 labelled leukocytes,  $\sim 90\%$  of input leukocytes can be recovered. Fig. 3.14(a) and (b) show

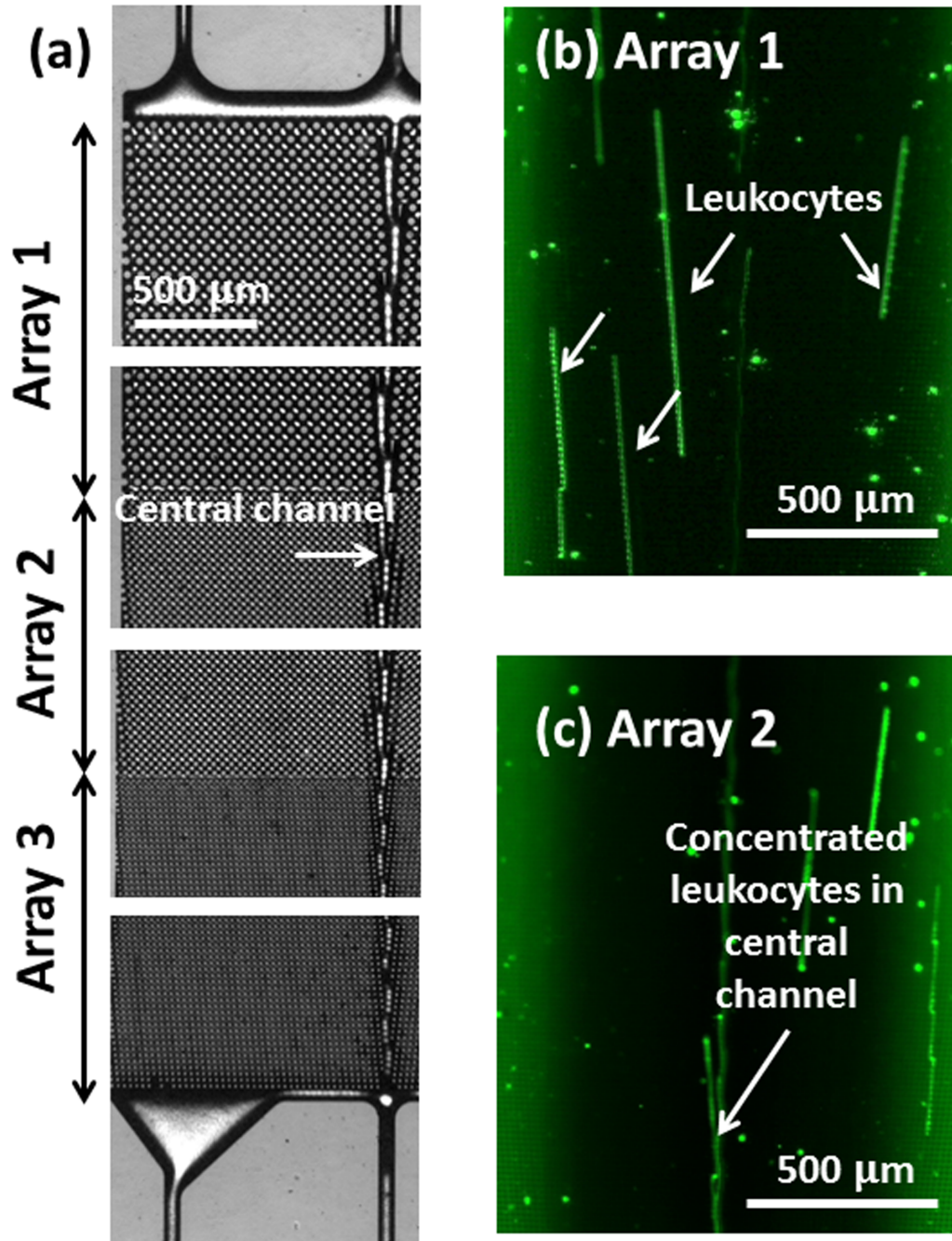


Figure 3.14: (a) Symmetric 3-zone DLD array fabricated using conventional micro-fabrication techniques. Only the left part of the arrays is shown. The total device is 120  $\mu\text{m}$  deep, 1.8 mm wide (0.89 mm wide for one-side array), and 3.71 cm long. Three zones of DLD arrays of different post diameters and gaps are placed sequentially (b) Fluorescence image of SYTO 13 labelled leukocytes flowing in Array 1. Leukocytes larger than the 7.9  $\mu\text{m}$  critical size were directed to the central channel. (c) Fluorescence image of SYTO 13 labelled leukocytes flowing in Array 2, as more leukocytes were concentrated in the central channel.

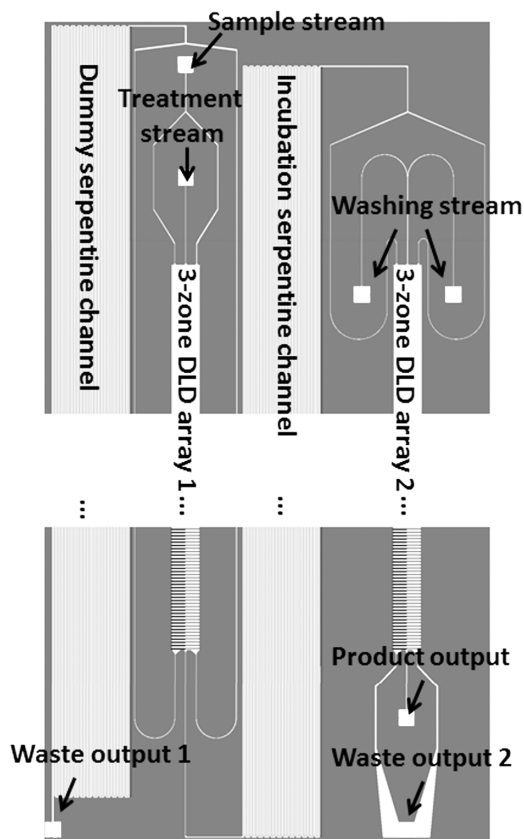


Figure 3.15: Design of 3-zone DLD arrays with long serpentine channels created using L-edit software. The incubation serpentine channel is 25 straight channels of  $100\ \mu\text{m}$  wide,  $100\ \mu\text{m}$  gaps, and 6.15 cm long connected together (153.8 cm long in total). The dummy serpentine channel is of the same design as of the incubation serpentine channel to balance the output fluidic resistances of the waste outputs and the central product output of the first 3-zone DLD array. The dummy serpentine channel simplifies the process for determining the desired input flow rates as shown in Section 3.4.3.

the SYTO 13 labelled leukocytes flowing in Array 1 and 2 respectively. Clearly, more leukocytes were concentrated in the central channel in Array 2 than Array 1.

The second challenge lies in the design of the integrated device. Fig. 3.15 displays the design of 3-zone DLD arrays with two long serpentine channels. The incubation serpentine channel is 25 straight channels of 100  $\mu\text{m}$  wide, 100  $\mu\text{m}$  gaps between two adjacent channels, and 6.15 cm long connected together (153.8 cm long in total). A second serpentine channel of the same design as of the incubation serpentine channel (dummy serpentine channel) was introduced to the integrated design to balance the fluidic resistances of the waste outputs and the central product output of the first 3-zone DLD array as shown in Fig. 3.15. As shown in Section 3.4.3, the dummy serpentine channel will simplify the design of the integrated device and the process for determining the right fluidic control parameters.

### 3.4.3 Flow Control

The device was driven by continuous flow of syringe pumps. The flow rates of sample stream, treatment stream, washing stream should be set carefully, otherwise undesired flow pattern could take place, such as the washing stream back-flow into the incubation serpentine channel. To find the correct input flow rates, we proposed the following approach.

Fig. 3.16 shows the fluidic analogous circuit model. The syringe pumps are represented by two current source  $F_1$  and  $F_2$ , unit:  $\text{m}^3/\text{s}$ .  $F_1$  consists of the sample and treatment stream, while  $F_2$  is the washing stream. Flux  $F_{S2}$  flows through the incubation serpentine channel to the second 3-zone DLD array, and  $F_{S1} = F_1 - F_{S2}$  goes through the dummy serpentine channel.  $P_1$  and  $P_2$  are the fluid pressures before and after the incubation serpentine channel. Suppose  $F_{S2} = \gamma F_1$ , we can obtain  $F_2$  by solving the following equations

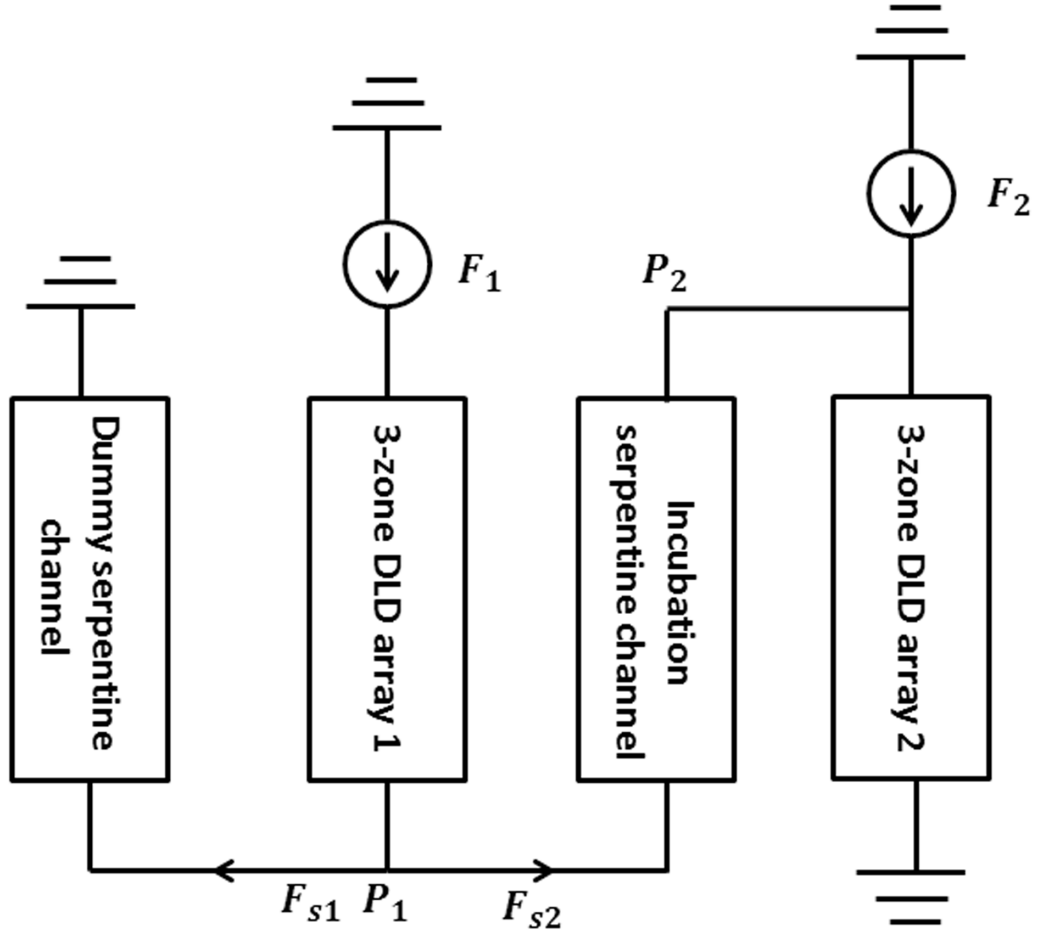


Figure 3.16: Fluidic analogous circuit model of DLD arrays with serpentine channels.

$$\left\{ \begin{array}{l} F_{S2} = \gamma F_1 \\ F_{S1} = F_1 - F_{S2} \\ P_1 = F_{S1} R_S \\ P_2 = (F_{S2} + F_2) R_D \\ P_1 - P_2 = F_{S2} R_S \end{array} \right. \quad (3.8)$$

The solved  $F_2$  can be written as

$$F_2 = \frac{(1 - 2\gamma)R_S - \gamma R_D}{R_D} F_1 \quad (3.9)$$

where  $R_S$  and  $R_D$  are the fluidic resistances of the serpentine channel and 3-zone DLD array respectively.

For a simple rectangular geometry with parabolic flow applied, the fluidic resistance  $R$  can be calculated as [74]

$$R = \frac{12\mu L}{W^3 H} \quad (3.10)$$

where  $\mu$  is the dynamic viscosity of the fluid,  $L$  is the length,  $W$  is the width, and  $H$  is the depth of the rectangular geometry with  $H \gg W$ . For a DLD array with circular posts, the fluidic resistance can be estimated as [74]

$$R \approx \frac{4.6\mu L_{tot}}{W_{tot} G^2 H_{tot}} \quad (3.11)$$

Table.3.3 shows the fluidic resistances of the DLD arrays in the 3-zone DLD array and serpentine channel calculated using Eq. 3.10 and 3.11, assuming  $\mu = 1 \times 10^{-3}$  Pa·s.

Table 3.3: Calculated fluidic resistances of DLD arrays and serpentine channels

	<b>Fluidic resistance</b> <b>(<math>10^{12}</math> Pa·s/m<sup>3</sup>)</b>
Array 1	0.9
Array 2	2.0
Array 3	4.6
3-zone DLD array in total	7.5
Serpentine channel	153.8

The target cells flowing in the long serpentine channel accounts for the most of on-chip incubation. Thus we can estimate the on-chip incubation time ignoring the

Table 3.4: Calculated input flow rates and on-chip incubation time for DLD arrays with serpentine channels

$F_1$ ( $\mu\text{L}/\text{min}$ )*	$\gamma$	$F_2$ ( $\mu\text{L}/\text{min}$ **)	Incubation time (min)
10	1/4	100	7.4
10	1/10	163	18.5
20	1/2.5	75	2.3
20	1/4	200	3.7
20	1/10	326	9.3
200	1/3	1300	0.3

\* flow rate of sample stream = flow rate of treatment stream =  $\frac{1}{2}F_1$

\*\* flow rate of washing stream =  $F_2$

processing time in the DLD array

$$t_{incubate} = \frac{V_S}{\gamma F_1} \quad (3.12)$$

where  $V_S = 18.5\mu\text{L}$  is the volume of serpentine channel. Table 3.4 shows the input flow rates calculated using Eq. 3.9 and incubation time using Eq. 3.12 for DLD arrays with serpentine channels. 0.3 to 20 min can be achieved by varying the flow rates. The sample and treatment stream flow rates were set to be 1:1 to form  $F_1$ , and  $F_2$  was set according to Eq. 3.9 for experiments.

### 3.4.4 Experimental Results

We first tested the recovery efficiency of the proposed device. 1:3 diluted blood sample with leukocytes pre-labelled with SYTO 13 was used as the input sample. For detailed blood preparation protocols, see Appendix C. The recovery efficiency was measured as the ratio between the number of leukocytes collected at the product output to that of the input sample via hemocytometer counting. Five experiments at three different conditions were conducted and the results are listed in Table 3.5.

Table 3.5: Recovery efficiency of leukocytes measured in DLD arrays with serpentine channels

$F_1$ ( $\mu\text{L}/\text{min}$ )*	$F_2$ ( $\mu\text{L}/\text{min}$ **)	$\gamma$	Recovery efficiency (%)
20	75	1/2.5	71
20	75	1/2.5	83
20	75	1/2.5	75
20	200	1/4	62
20	326	1/10	56

\* flow rate of sample stream = flow rate of treatment stream =  $\frac{1}{2}F_1$

\*\* flow rate of washing stream =  $F_2$

As shown in Table 3.5, the recovery efficiency was affected by the fraction (determined by the flow rate of washing stream) flowing to the second 3-zone DLD array for a fixed sample and treatment stream flow rate. When  $\gamma = 1/2.5$ , the recovery efficiency was about  $\sim 75\%$ . However, as  $\gamma$  decreased, the recovery efficiency also decreased to 62% and 56% for  $\gamma = 1/4$  and  $\gamma = 1/10$  respectively.

We then presented the on-chip leukocyte labelling with R6G (20  $\mu\text{g}/\text{mL}$ ) using the proposed device. Fig. 3.17 displays the fluorescence images of on-chip leukocyte labelling with R6G using DLD arrays with serpentine channels at different positions. The 1:3 diluted blood sample without pre-labelling was loaded to the device (“Blood in” in Fig. 3.17). No visible leukocytes (white blood cells, WBCs) can be observed (Fig. 3.17(a)). The leukocytes were concentrated to the incubation serpentine channel to be labelled, while the red blood cells and plasma were flowing directly to the waste outputs. After leaving the incubation serpentine channel, leukocytes were then directed to the product output (Fig. 3.17(e)). The unreacted label (R6G) also moved to the waste outputs. The contamination of R6G in the prepared cells was measured as the remaining fluorescence intensity in the collected cell sample solution (background fluorescence intensity) to that of the treatment stream (“Label in” in

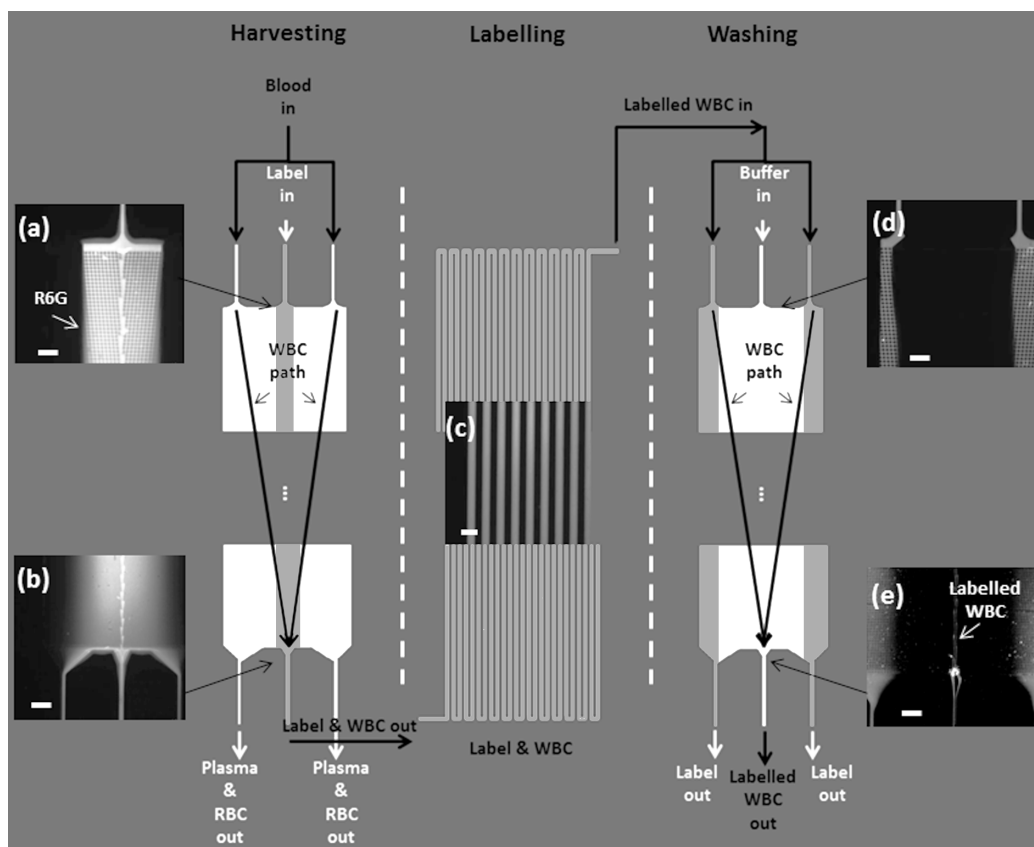


Figure 3.17: Fluorescence images of on-chip leukocyte labelling with R6G ( $20 \mu\text{g}/\text{mL}$ ) using DLD arrays with serpentine channels. (a) The input region of sample and treatment streams at the first 3-zone DLD array. (b) The output region of the first 3-zone DLD array. (c) The middle region of incubation serpentine channel. (d) The input region of the second 3-zone DLD array. (e) The output region of the second 3-zone DLD array. The labelled leukocytes (white blood cell, WBC) were concentrated to the product output. The scale bar is  $200 \mu\text{m}$ .

Fig. 3.17). The contamination results together with the on-chip incubation time at different conditions were listed in Table 3.6.

Comparing Table 3.5 and 3.6, we can see that the device performance was affected by the washing stream flow rate for a fixed flow rate of sample and treatment streams. When the device running with low washing stream flow rate, the device showed high recovery efficiency  $\sim 75\%$ , 2.3 min incubation time, and 0.02 contamination of R6G in prepared cells. While when the washing stream was loaded at  $326 \mu\text{L}/\text{min}$ , the

Table 3.6: Contamination and on-chip incubation time for leukocyte labelling with R6G using DLD arrays with serpentine channels

$F_1$ ( $\mu\text{L}/\text{min}$ )*	$F_2$ ( $\mu\text{L}/\text{min}$ **)	Incubation time (min)	Contamination
20	75	2.3	0.02
20	200	3.7	0.001
20	326	9.3	0.001

\* flow rate of sample stream = flow rate of treatment stream =  $\frac{1}{2}F_1$

\*\* flow rate of washing stream =  $F_2$

recovery efficiency decreased to 56%, but the incubation time increased to 9.3 min, and the contamination reduced to 0.001.

### 3.4.5 Summary of DLD Arrays with Serpentine Channels

An incubation serpentine channel was introduced to two connected 3-zone DLD arrays for on-chip chemical processing of leukocytes. The first 3-zone DLD array separated the leukocytes from the other content of the diluted blood sample. The concentrated leukocytes were then directed to the incubation serpentine channel for on-chip incubation. The on-chip washing was performed via the second 3-zone DLD array. For a simplified design of this integrated device, a dummy serpentine channel was introduced as well to balance the fluidic resistances at the outputs. A fluidic analogous circuit model was developed to determine the flow rates of the sample, treatment, and washing streams. We demonstrate on-chip leukocyte labelling with R6G with this proposed device.  $\sim 75\%$  recovery efficiency of leukocytes (similar to conventional DLD array with one type of geometry), 2.3 min on-chip incubation ( $200 \times$  the conventional DLD array, and  $20 \times$  the DLD array with separator walls), and 0.02 contamination of R6G ( $\sim 1/7 \times$  the conventional DLD array, and  $\sim 1/3 \times$  the DLD array with separator walls). For a longer on-chip incubation time and lower contamination, the flow rate through the serpentine channel can be decreased. This can be

done without increasing the output contamination by increasing the washing stream flow rate in the second 3-zone DLD array for the final cell recovery. However, the recovery efficiency decreased significantly as the washing stream flow rate goes up.

### 3.5 Summary and Outlook

In this chapter, we tried to develop a microfluidic system driven by continuous flow for on-chip cell preparation using DLD arrays. The device proposed by K. J. Morton, et al. [7] utilizing conventional DLD arrays can be used for on-chip platelet labelling with R6G and on-chip cell lysis. However, there was no microfluidic structure to control the diffusion of treatment chemical, thus the diffusion of treatment chemical took place all through the array. For on-chip preparation of leukocytes from raw blood, the conventional DLD arrays can only provide  $\sim 10\text{--}100$  ms to achieve desired level of contamination of treatment chemical in the prepared cells ( $\sim 0.01$  the concentration of treatment chemical at the input of treatment stream).

To resolve the trade-off between incubation time and the contamination of treatment chemical, we first introduced two separator walls to the conventional DLD array. The target cells were first concentrated at the first separator wall for an extended on-chip incubation. The first separator wall also confined the diffusion of treatment chemical in a smaller region to reduce the contamination of treatment chemical. By implementing the second separator wall, the diffusion of treatment chemical can be further suppressed when the flow speed was low. We demonstrated on-chip leukocyte labelling with R6G ( $20\ \mu\text{g}/\text{mL}$ ) with a 4 s incubation and  $\sim 0.067$  contamination at the product output.

We then tried to further increase the incubation time with an integrated device of two symmetric 3-zone DLD arrays and two very long serpentine channels. The first DLD array harvested the leukocytes from a diluted blood sample into a central

channel. The concentrated leukocytes were then directed to the incubation serpentine channel for long time on-chip incubation. The second 3-zone DLD array was used to perform the on-chip washing to remove the unreacted labels. A dummy serpentine channel was placed at the outputs of the first 3-zone DLD array to balance the fluidic resistances. We developed an analogous circuit model to determine the correct flow rates of the sample, treatment, and washing stream for on-chip cell preparation. On-chip leukocyte labelling with R6G (20  $\mu\text{g}/\text{mL}$ ) was demonstrated using this device with a 2.3 min incubation and  $\sim 0.02$  contamination.

Though the DLD arrays with serpentine channels can provide much longer on-chip incubation time with low contamination level of treatment chemical, the device has the following three major disadvantages. The first is the large area of the device, which increases cost. The design discussed in this thesis is  $3.6 \text{ cm} \times 7 \text{ cm}$  which is  $\sim 8\times$  area of a conventional DLD array or a DLD array with separator walls. The second is the implementation of two DLD arrays, limiting the recovery efficiency. To overcome this disadvantage, a multi-zone DLD array can be used. However, this increases the area consumption. As discussed in Section 3.4.4, to have high recovery efficiency, the fraction of fluid flowing to the incubation serpentine channel ( $\gamma$ ) should be set large enough to capture most cells (a typical value ranges from  $1/5$  to  $1/2.5$ ). To have low contamination of treatment chemical, the flow rate of the washing stream in the DLD array ( $F_2$ ) should be set high enough ( $>100 \mu\text{L}/\text{min}$ ). Since  $F_1$  (the flow rate of sample and treatment stream) is proportional to  $F_2$ , the on-chip incubation time is thus often  $<10$  min according to Eq. 3.12, to have desired recovery efficiency and contamination level. The third is the large consumption of treatment chemical due to the large void volume in the device ( $\sim 50 \mu\text{L}$ , two three-zone DLD arrays and two long serpentine channels) which requires a large volume of treatment chemical to fill the device before experiment and to be kept flowing during the entire incubation time, which in many cases should be on the order of 10 min.

## Chapter 4

# On-Chip Chemical Processing of Biological Cells by Capture and Release Using Microfluidic Trap Arrays

### 4.1 Introduction

The previous work for on-chip preparation of biological cells using DLD arrays can only provide  $\sim 5$  min on-chip incubation to have desired level of contamination of the treatment chemical ( $\sim 0.01$  the concentration of input treatment chemical stream). Further, the devices with longest incubation time required large areas, and because they were “continuous-flow”, the amount of treatment chemicals (e.g. monoclonal antibodies) increased with the incubation time.

In this chapter, we demonstrate a new approach, trapping cells on-chip and introducing the treatment chemicals to the trapped cells, rather than a “continuous-flow” approach. A. Huebner, et al. have demonstrated a simple 2-dimensional trap struc-

ture for droplet trapping, incubation and release for enzymatic and cell-based assays [10]. 90% of captured droplets can be released from the trap structure, although the capture efficiency is extremely low:  $> 90\%$  of droplets just pass through the trap array. A 3-dimensional trap structure of similar idea is proposed by D. Di Carlo, et al. for on-chip cell culture and single-cell analysis for enzyme concentrations, kinetics, and inhibition [11, 12]. Again the capture efficiency of cells is still very low. Interestingly, a modified 3-dimensional trap structure has shown a capture efficiency of 90% of incoming cells [13]. But the improvement of capture efficiency is not explained well in this paper and this 3-dimensional trap structure is not capable for cell release for further chemical process and analysis, such as fluorescence-activated cell sorting (FACS) and DNA sequencing. However, the simple device design, straightforward operation steps, and potentials in achieving both high capture and release efficiency of particles and cells make this idea attractive. The basic structure was described in Section 2.3 and is introduced again in Section 4.2.

Inspired by these works, we propose a novel 3-dimensional microfluidic trap structure for on-chip chemical processing of cells by capture and release. There is a critical gap  $G_C$  between the trap structure and Pyrex glass lid. When cells larger than the critical gap move against the traps, they will be physically captured due to their size. On the other hand, when a flow applied from the other direction, a fluidic force along the flow direction will push the cells out of the trap structure. Particles or cells can be captured (Fig. 4.1a), labeled (or processed by other chemicals) (Fig. 4.1b), washed (Fig. 4.1c), and released (Fig 2d) for further analysis and process. Unlike DLD arrays, target cells are immobilized by the trap structures and then processed by sequentially loading treatment chemical, washing, and releasing streams, other than being directed through multiple fixed functional regions.

The proposed structure has streamlined shape which minimizes clogging of cells in capture and release steps. The rectangular shaped traps described in Ref. [11–13]

will exert a large mechanical force against the flow direction on cells moving close to the traps, which will greatly decrease the moving speed of cells. When cells flowing in low speed, there is a high chance for them to stick to each other and form clots since they have more time to form the adhesion bonds. However, the streamline shaped traps described in this thesis, on the other hand, will apply less mechanical force against the flow direction on cells than rectangular shaped traps especially in release steps, leading to a reduced clogging of cells. The trap structure arrays are built and tested using leukocytes, with different load flow speeds, incubation times, and release flow speeds.  $\sim 85\%$  of cells are captured independent of the input flow speed. The release efficiency depends on the incubation time, with over  $\sim 80\%$  of captured cells released for up to 20 min incubation, and on-chip labelling and washing with STYO 13 is demonstrated. Qualitative models are developed as guidance for designing the proposed trap structure and to explain the increased performance over previous approaches.

## 4.2 Device Design

Fig. 4.2 shows the 3-D microfluidic trap structure schematic designed and tested in this thesis. When a flow is input against the trap structure, cells of size above the critical gap  $G_C$  flowing in the fluid will be physically captured (Fig. 4.2(a)). While, when a flow is input from the other direction, a net force will be applied on the cells through this critical gap to release the cells from the trap structure (Fig. 4.2(b)). Fig. 4.3(a) shows the side view schematic of the trap structure, with a critical gap  $G_C$  between the trap to Pyrex glass lid in a channel of  $H_{tot}$  height. Fig. 4.3(b) displays the top view schematic of the microfluidic trap array. In our experiments, the open region of the trap structure is  $W_1 = 18 \mu\text{m} \times L_1 = 15 \mu\text{m}$ , which is large to capture most leukocytes (10 to 20  $\mu\text{m}$  diameter [75]), circulating tumor cells (CTCs, 8 to 15

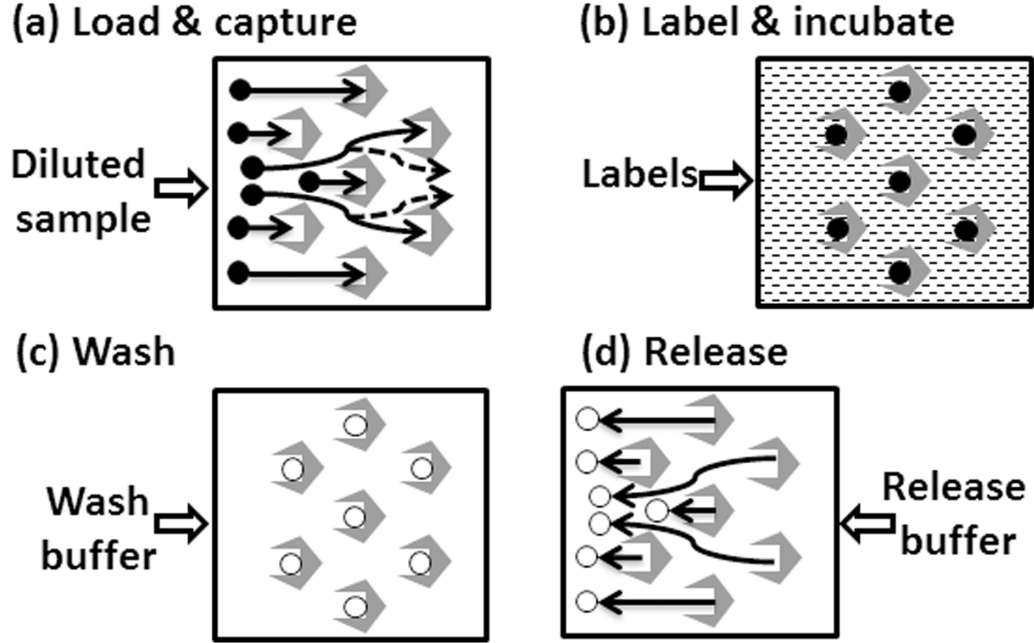
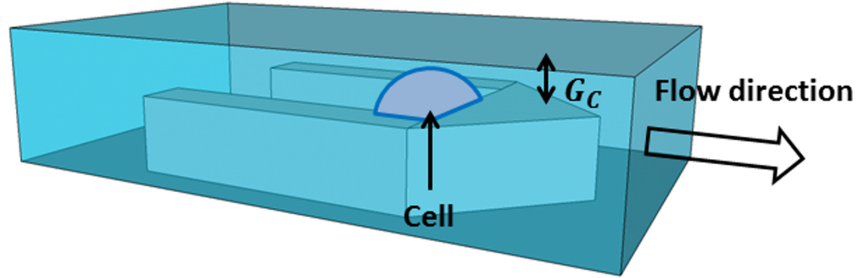


Figure 4.1: Operations for on-chip labelling of biological cells using the proposed microfluidic device: (a) Load the cell sample to the device and physically capture the cells (b) Input the process chemical (labels) to the device and incubate. (c) Rinse with wash buffer to remove the unbound labels. (d) Release the processed cells from the device.

$\mu\text{m}$  diameter [44, 46]), etc. An isosceles triangle of  $L_2 = 10 \mu\text{m}$  height and  $W_2 = 25 \mu\text{m}$  base is placed next to the open region to reduce clogging during the release step. The entire trap structure fits a square of  $25 \mu\text{m}$  edge. The trap array has a  $P_x = 50 \mu\text{m}$  spacing in  $x$ -direction and a  $P_y = 10 \mu\text{m}$  spacing in  $y$ -direction. Each device unit,  $L_{unit} = 450 \mu\text{m}$  long, consists of 1 column of support pillars for the lid and 8 columns of microfluidic traps. The support pillars are circular posts of  $D_s = 80 \mu\text{m}$  diameter,  $G_s = 80 \mu\text{m}$  gap between each two posts, and a  $G_{st} = 50 \mu\text{m}$  gap to the trap array. The purpose of support pillars is to avoid the deformation of the Pyrex glass lid (anodically bonded to the pillars and channel walls), to maintain tight control of the critical gap across the device channel. Four devices (Fig. 4.3(e)) were used in parallel in each experiment. Each device of width  $2 \text{ mm}$  contains 53 device units, providing  $7 \times 10^4$  traps in total.

### (a) Trap cell



### (b) Release cell

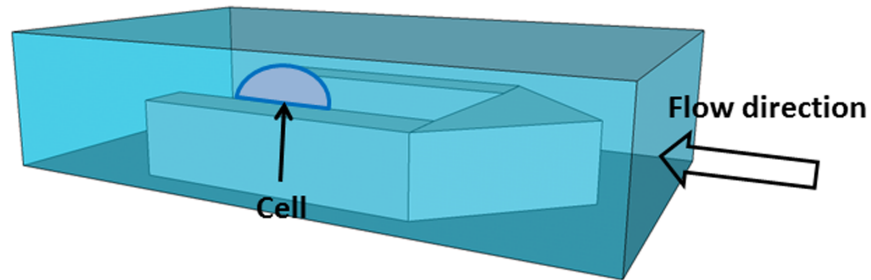


Figure 4.2: Schematic of 3-D microfluidic trap structure, where the lid would be on the top of the 3-D boxed region shown in the figures. There is a critical gap  $G_C$  between the trap structure and lid layer. (a) When a flow is input against the trap structure, cells of size larger than  $G_C$  flowing in the fluid will be physically captured. (b) When a flow is input from the other direction, a net force will be applied on the cells through this critical gap to release the cells from the trap structure.

## 4.3 Leukocyte Capture

For leukocyte experiments, 6- $\mu\text{m}$  critical gap devices were used. Deformation of cells, which normally are 15–20  $\mu\text{m}$  in diameter, in shear flow enables them to pass through 8 to 10  $\mu\text{m}$  gaps [76], and some cells of diameter  $\sim 20 \mu\text{m}$  will get stuck if the critical gap is too small ( $> 20\mu\text{m}$  deep channel is required. The trap structure is 14  $\mu\text{m}$  tall, so the lower bound to the critical gap is 6  $\mu\text{m}$ ). RBC-lysed SYTO 13-stained leukocyte solutions of  $2 \times 10^5$  cells/mL concentration were loaded at 46  $\mu\text{m/s}$ , 460  $\mu\text{m/s}$ , or 4.6 mm/s average flow speed for 5 min. Four devices were used in each experiment providing 69,536 traps. The input volume of diluted leukocyte sample was 2  $\mu\text{L}$  ( $\sim 400$  cells), 20  $\mu\text{L}$  ( $\sim 4,000$  cells), and 200  $\mu\text{L}$  ( $\sim 40,000$  cells) for input

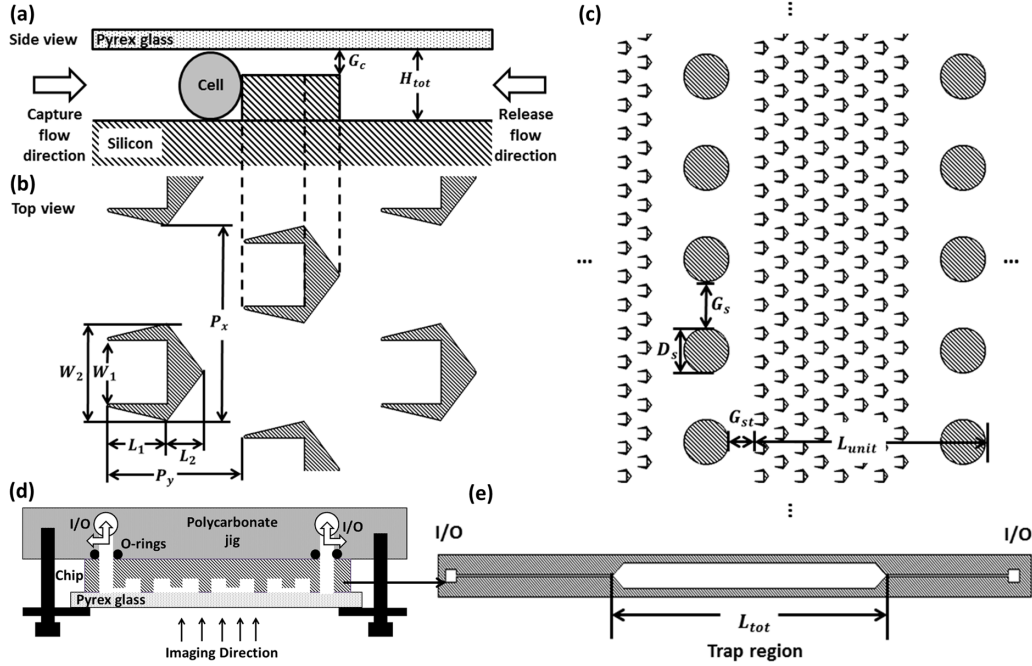


Figure 4.3: (a) Side view schematic of the trap structure, with a critical gap  $G_C$  between the trap to Pyrex glass lid in a channel of  $H_{tot}$  height. (b) Top view:  $P_x = 50 \mu\text{m}$  and  $P_y = 35 \mu\text{m}$ . (c) Each device unit, ( $L_{unit} = 450 \mu\text{m}$  long), consists of 1 column of support pillars, and 8 columns of microfluidic traps. (d) Schematic of the experimental setup. (e) Each device of width 2 mm contains 53 device units, providing  $7 \times 10^4$  traps in total.

flow speed of  $46 \mu\text{m/s}$ ,  $460 \mu\text{m/s}$ , or  $4.6 \text{ mm/s}$ , respectively. Fig. 4.4 shows the time sequence of leukocyte capture at an average flow speed of  $460 \mu\text{m/s}$ . The images are 10 s apart with a 10 ms exposure time. From the capture experiments, we can see that most traps capture approximately one cell at a time. Fig. 4.5 shows the experimental results of the capture efficiency of devices with  $6 \mu\text{m}$  critical gap of different flow speeds measured as  $1 - n_{escape}/n_{tot}$ , where  $n_{escape}$  is the number of leukocytes passing through the device and  $n_{tot}$  is the number of total input leukocytes.  $46 \mu\text{m/s}$ ,  $460 \mu\text{m/s}$ , and  $4.6 \text{ mm/s}$  input speeds had 5, 20, and 100 experiments, respectively. Each experiment was conducted by inputting  $0.7 \mu\text{L}$  stained leukocyte sample solution and then counting the number of escaping leukocytes at the outputs. The capture efficiencies were 84.1%, 83.7%, and 84.8% for  $46 \mu\text{m/s}$ ,  $460 \mu\text{m/s}$ , and  $4.6 \text{ mm/s}$  input

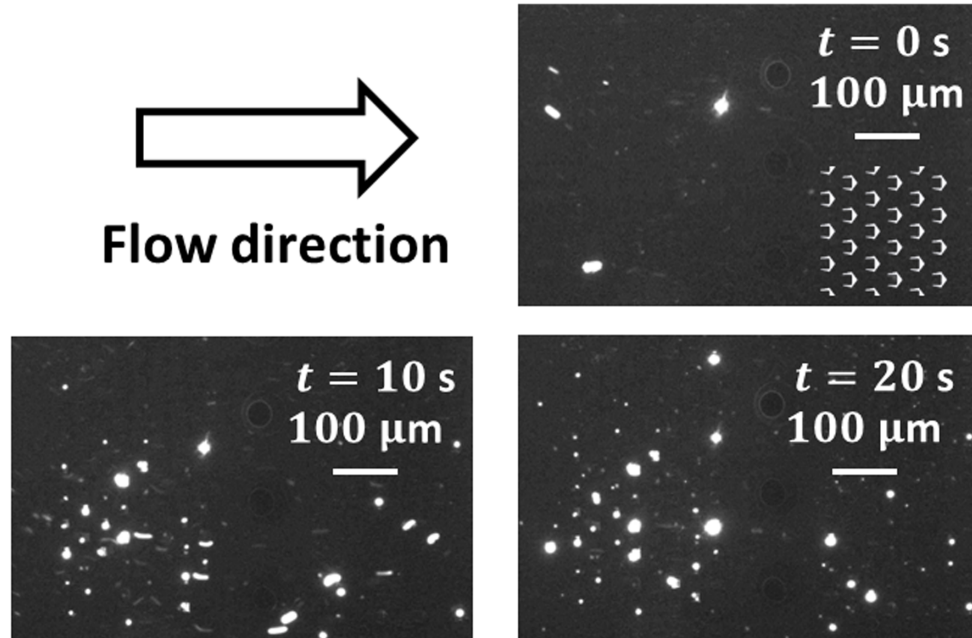


Figure 4.4: Time sequence of leukocyte capture at an average flow speed of  $460 \mu\text{m/s}$ . A pre-stained leukocyte sample solution was used. The inset in the bottom right of the top right image shows the outline of the traps.

speeds respectively, almost as high as the 90% in Ref .[10]. The increased input speed did not have a significant impact on the leukocyte capture efficiency.

#### 4.4 Leukocyte Labelling with SYTO 13 and Washing

An unstained leukocyte sample solution was first input at  $460 \mu\text{m/s}$  for 5 min to trap cells. A diluted SYTO 13 labelling solution ( $25 \mu\text{M}$ ), a nucleic acid stain, was then loaded to the device at  $460 \mu\text{m/s}$ . Fig. 4.6(a)–(c) shows the time sequence of leukocyte on-chip labelling with SYTO13. The images were taken at  $t = 0$  s, when labelling solution just arrived at the observed region,  $t = 20$  s, and  $t = 50$  s respectively with a 10 ms exposure time. The total incubation time was  $\sim 1$  min for this experiment. During the incubation period, no labelling solution is flowing,

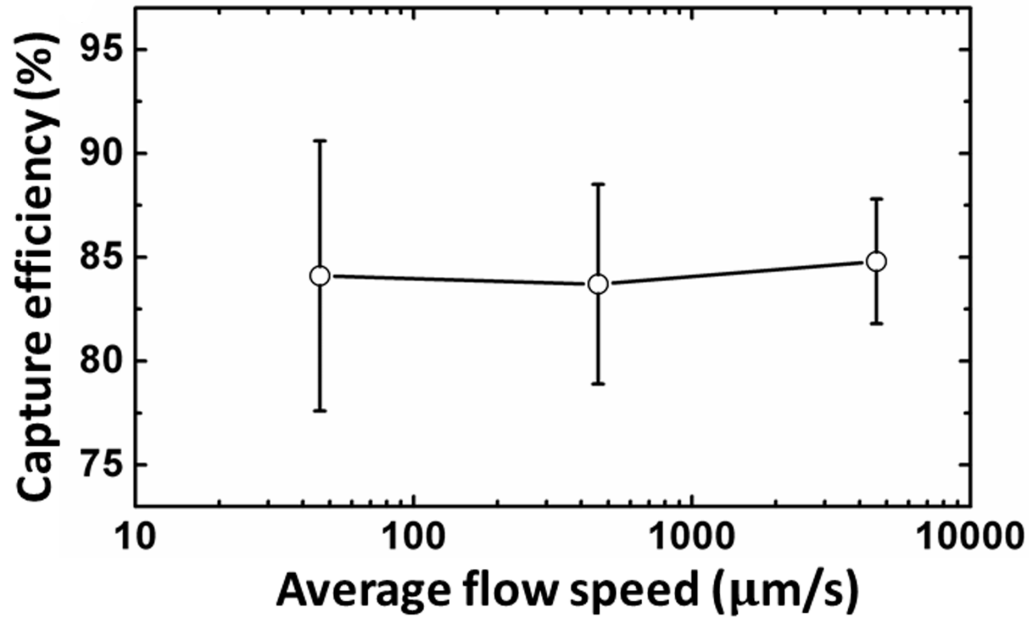


Figure 4.5: Experimental capture efficiency of leukocytes in devices with  $6 \mu\text{m}$  critical gap at different flow speeds.  $46 \mu\text{m/s}$ ,  $460 \mu\text{m/s}$ , and  $4.6 \text{ mm/s}$  input speeds had 5, 20, and 100 experiments respectively. Each experiment was conducted via inputting  $0.7 \mu\text{L}$  leukocyte sample solution and then counting the number of escaping leukocytes at the outputs.

leading to a much lower use of labels compared to the continuous-flow approaches discussed in previous chapters, especially for long incubation times. After labelling, the leukocytes were washed with wash buffer at  $460 \mu\text{m/s}$  for 5 min (Fig. 4.6(d)). The background fluorescence noise (intensity outside of the traps) was decreased  $10^3$  by the wash step (Fig. 4.6(c)–(d)). Fig. 4.7 demonstrates the total fluorescence intensity (the sum of fluorescence intensities of each pixel within the captured leukocytes) of the obtained movies at different incubation times. The total fluorescence intensity initially increased very quickly, and began to saturate after  $\sim 30 \text{ s}$ , consistent with off-chip labelling results [77].

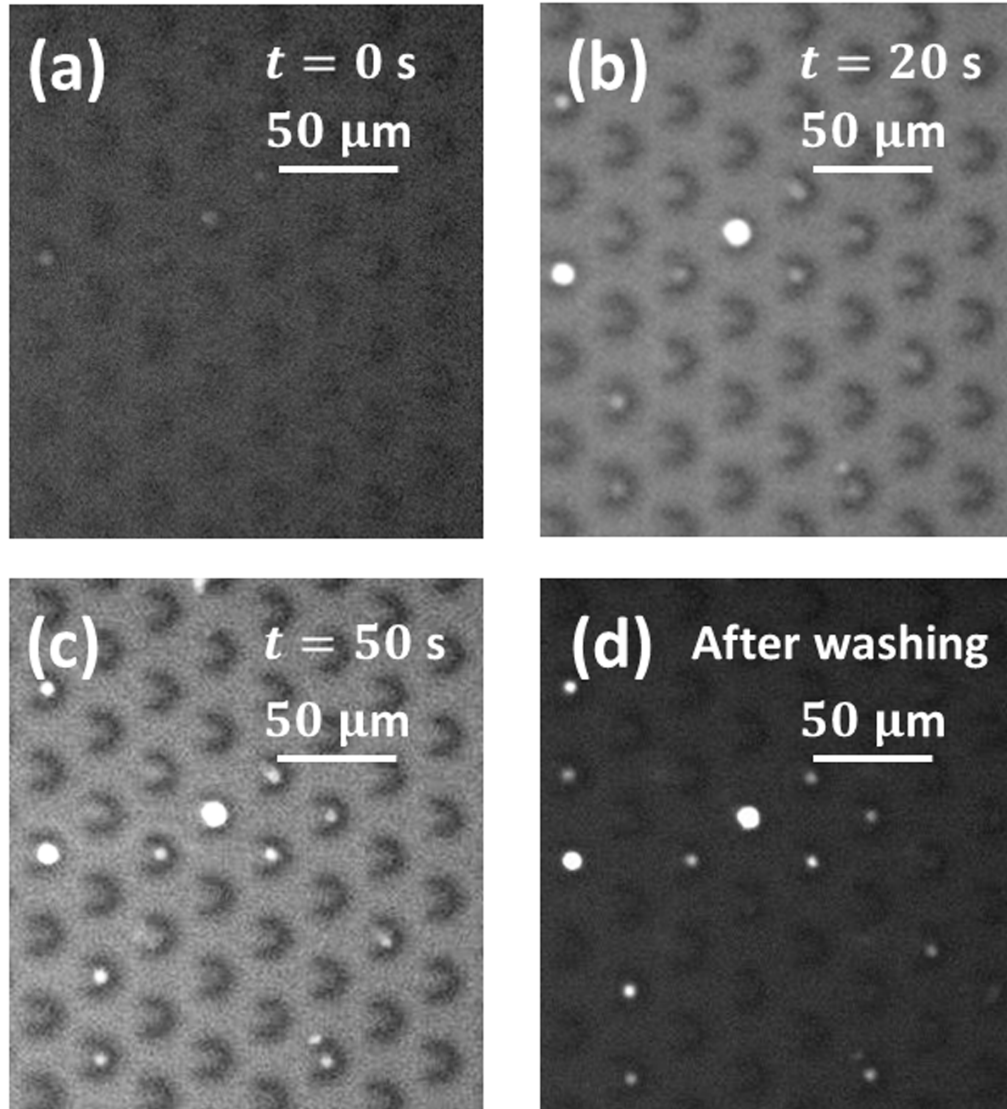


Figure 4.6: (a)–(c) Time sequence of on-chip leukocyte labelling with SYTO 13 after a load & trap step at average flow speed of  $460 \mu\text{m/s}$  for 5 min. An unstained leukocyte sample solution was used and the images were taken at  $t = 0$  s (when labelling solution just arrived at the observed region), 20 s, and 50 s respectively. (d) Fluorescence image of the same point of view after 5 min washing at  $460 \mu\text{m/s}$ .

## 4.5 Leukocyte Release

Eight sets of experiments were conducted to investigate the release of leukocytes from the traps. The load step for all the experiments was done at  $460 \mu\text{m/s}$  for 5 min. After the load step, the leukocytes were on-chip incubated for 1 min, 5 min, 10 min

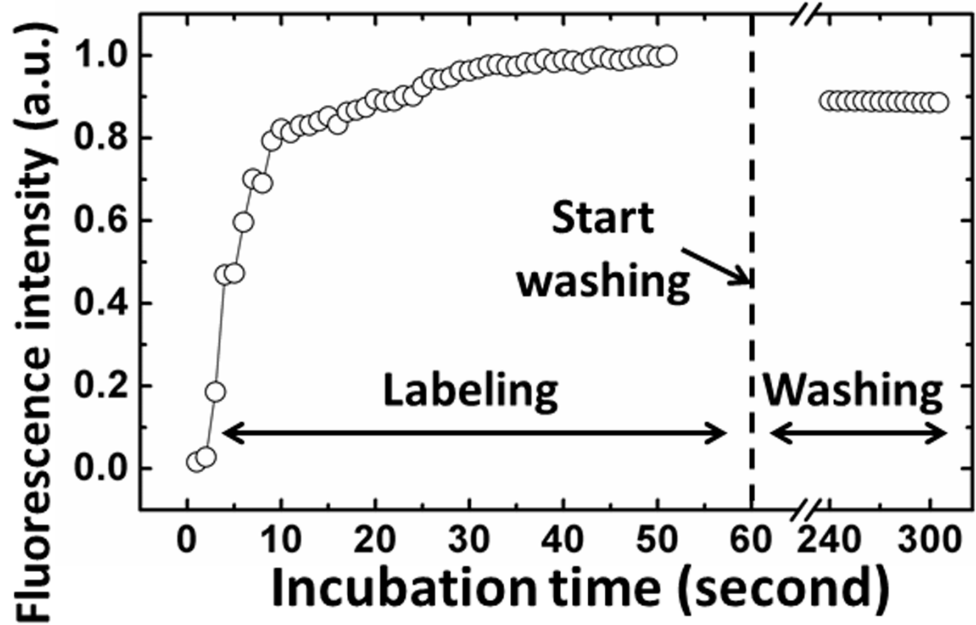


Figure 4.7: The total fluorescence intensity (sum of fluorescence intensity of each pixel within captured cells) vs. time for SYTO 13 leukocyte labelling and washing in the proposed trap array.

and 20 min and then released at 4.6 mm/s and 9.2 mm/s. Fig. 4.8 shows the time sequence of leukocyte release at an average speed of 4.6 mm/s after a load step at average flow speed of  $460 \mu\text{m/s}$  for 5 min and an on-chip incubation for 5 min. The images are 10 s apart with a 10 ms exposure time. At  $t = 0$  s, the white dots in the top right image of Fig. 4.8 are the trapped cells. The bottom left image of Fig. 4.8 is  $t = 10$  s where the white lines are time-lapse images of cells moving from right to left. At  $t = 20$  s, the white dots in the bottom right image of Fig. 4.8 are remaining cells stuck in the traps. Fig. 4.9 displays the experimental results of percentage of the number of released leukocytes to the number of captured leukocytes, defined as  $1 - n_{remain}(t)/n_{ini}$ , where  $n_{remain}(t)$  is the number of remaining leukocytes at time  $t$  and  $n_{ini}$  is the number of captured leukocytes at the beginning of the release step. For short incubation time,  $\leq 5$  min,  $\sim 99\%$  of captured leukocytes can be released for both 4.6 mm/s and 9.2 mm/s release flow speeds in 20 min. However as the incubation

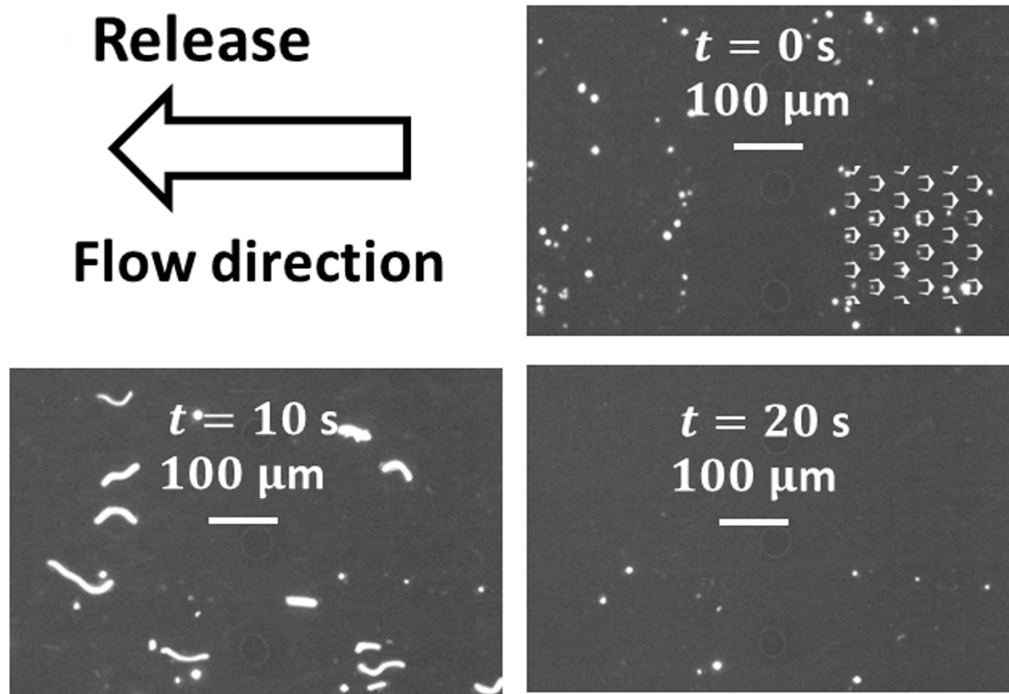


Figure 4.8: Time sequence of leukocyte release at an average speed of 4.6 mm/s after a load step at average flow speed of 460  $\mu\text{m/s}$  for 5 min and an on-chip incubation of 5 min. A pre-stained leukocyte sample solution was used and the images are 10 s apart with a 10 ms exposure time. At  $t = 0$  s, the white dots in the top right image are the trapped cells. The bottom left image is  $t = 10$  s where the white lines are time-lapse images of cells moving from right to left. At  $t = 20$  s, the white dots in the bottom right image are remaining cells stuck in the traps. The inset in the bottom right of the top right image is the outline of traps within  $200 \mu\text{m} \times 200 \mu\text{m}$ .

time increases, the cells were harder to release, and the higher release flow speed (9.2 mm/s) outperformed a lower 4.6 mm/s release speed. Leukocytes gradually form adhesion bonds to substrates surface and to the other cells [78–80]. The adhesion bonds between cells and substrates apparently increases the resistance force when release the captured cells. Therefore, higher release flow speed is required for long on-chip incubation. The adhesion bonds between cells make them to aggregate and form clots which cannot be easily released even for high flow speed. For 20 min incubation, 22% and 14% of the total captured leukocytes were not released for in 20 min at 4.6 m/s and 9.2 mm/s respectively. To the best of our knowledge, this

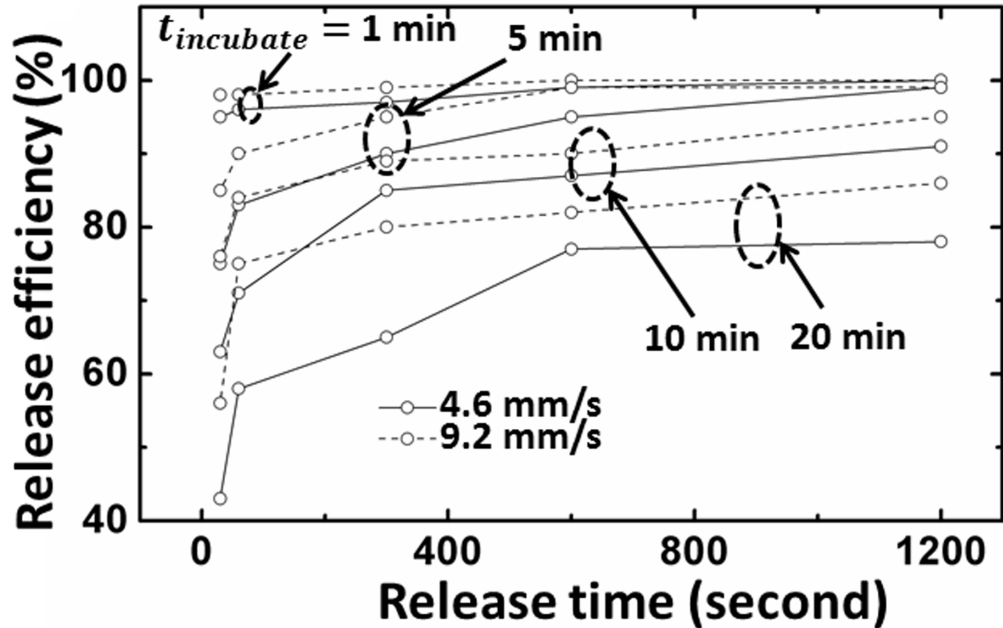


Figure 4.9: Experimental results of release efficiency for different release time after 1 min, 5 min, 10 min, and 20 min incubation at 4.6 mm/s and 9.2 mm/s release flow speeds.

is the first work studying the leukocyte release efficiency of this type of structures at different on-chip incubation times and flow speeds. For the demonstrated device, the release efficiency  $\sim 99\%$  is better than previous work (70% to 90% [13]) for short incubation time, and  $\sim 80\%$  for up to 20 min incubation in 20 min release.

## 4.6 Modelling of Cell Capture

Previous works have shown that the microfluidic trap devices can capture 70%–90% of the incoming cells [13]. However, there is need of good theoretical models as a guide for the trap structure design. A fully filled trap array is preferred for cell analysis and culture applications which often requires much more particles or cells (number of particles or cells  $\ll$  number of traps) to fill in all the traps [11, 12]. In other words, the

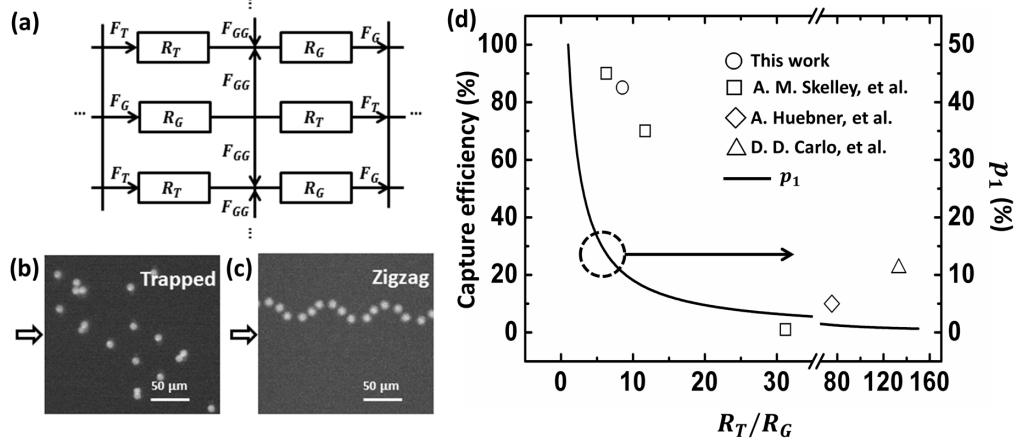


Figure 4.10: (a) Fluidic analogous circuit model of the proposed device to explain 2 typical flow patterns of particles: zigzag (always flow in the  $F_{GG}$ ) and trapped (stopped by the microfluidic traps). (b) Trapped  $10 \mu\text{m}$  beads in the device. (c) Integration of 17 frames of fluorescence images of a  $10 \mu\text{m}$  bead following the zigzag trajectory around the microfluidic traps. (d) Experimental results of capture efficiency (axis on the left) and the calculated  $p_1$  (solid line, axis on the right, the probability of particles captured by the first column of traps) as a function of  $R_T/R_G$ . Open circle: this work; open squares: Ref. [13]; open diamond: Ref. [10]; open triangle: Ref. [11, 12] (supposing  $10^6$  cells/mL concentration).

capture efficiency of particles or cells is low. In this chapter, we provide a qualitative model to better explain the achieved high capture efficiency of the proposed device.

#### 4.6.1 “One-Column” Model

Fig. 4.10(a) demonstrates the fluidic analogous circuit model of the trap array. The flux going through the trap and the gap between the traps are  $F_T$  and  $F_G$  respectively, and can be calculated as

$$F_T = \frac{\Delta P}{R_T} \quad (4.1)$$

$$F_G = \frac{\Delta P}{R_G} \quad (4.2)$$

where  $\Delta P$  is the pressure drop,  $R_T$  and  $R_G$  is the fluidic resistances of the trap structure and the gap respectively. Two fluxes  $F_{GG}$  separating from  $F_G$  will join  $F_T$  to form a new flux  $F_G$  through the next gap.

As discussed in Chapter 1, however, we repeat the concepts of Reynolds and Péclet number here for convenience. The Reynolds number in the trap region can be calculated as,

$$Re = \frac{\rho v_{avg} D_H}{\mu} \quad (4.3)$$

where  $\rho \approx 1$  g/mL is the density of the fluid,  $G_x = 25$   $\mu\text{m}$  is the gap between two traps,  $D_H = (2H_{tot}G_x)/(H_{tot} + G_x) \approx 22.2\mu\text{m}$  is the hydraulic diameter for critical gaps  $G_C = 6$   $\mu\text{m}$ , and  $\mu \approx 1 \times 10^{-3}$  Pa·s is the dynamic viscosity of the fluid. For the average flow speed ranges from 46  $\mu\text{m/s}$  to 9.2 mm/s,  $Re$  is of the order of  $10^{-3}$  to  $10^{-1}$ , so viscous forces are dominant and inertial forces can be neglected. The Péclet number describes the ratio between the advective and the diffusive transport rate of the particles, which is calculated as

$$Pe = \frac{v_{avg} L_D}{D} \quad (4.4)$$

where  $L_D = \sqrt{Dt}$  is the characteristic diffusion length,  $t = P_y/v_{avg}$  is the time fluid flow through the trap region and the gap between two adjacent columns of traps in  $y$ -direction,  $D = k_B T/3\pi\mu d_P$  is the diffusion constant of the particles,  $k_B$  is the Boltzmann constant,  $T$  is the temperature (300 K), and  $d_P$  is the particles diameter. For  $v_{avg}$  from 46  $\mu\text{m/s}$  to 9.2 mm/s and  $d_P = 10\mu\text{m}$ ,  $Pe$  is of the order of  $10^2$  to  $10^3$ . The diffusion of the particle is negligible [24].

Because  $Re \ll 1$  and  $Pe \gg 1$ , we can assume the particle moves at the flow speed and direction of the streamline where the particle center is. Intuitively, if a particle (assuming a size larger than the critical gap) in flow  $F_T$ , it will be captured in the first column (Fig. 4.10(b), trapped 10  $\mu\text{m}$  beads). A particle in  $F_G$  will not be

captured. Therefore, the probability  $p_1$  that a particle is captured in a first column, assuming all empty traps and an uniform distribution of input particles, will just be the probability that the particle moves in  $F_T$

$$p_1 = \frac{F_T}{F_T + F_G} = \frac{1}{1 + \frac{R_T}{R_G}} \quad (4.5)$$

The solid line on the right in Fig. 4.10(d) shows the predicted  $p_1$  for one column of the array for previous work (Open circle: this work; open squares: Ref. [13]; open diamond: Ref. [10]; open triangle: Ref. [11, 12] (supposing  $10^6$  cells/mL)) as a function of  $R_T/R_G$ .  $R_T/R_G$  was calculated in each case as  $F_G/F_T$  within a small part of the total trap arrays using COMSOL software with periodic boundaries applied to avoid computational complexity. The experimental capture efficiencies for entire array in each case are also plotted (left axis). The model predicts the trends of higher observed experimental trapping efficiency with small  $R_T/R_G$  and low capture efficiency at large  $R_T/R_G$ . The experimental numbers for the full arrays are consistently higher of course due to multiple columns in which the particles or cells may be captured.

#### 4.6.2 “Three-Column” Model with Wall Interaction Consideration

Note that for regular trap arrays, where each row is vertically displaced from the previous one by 50% of the vertical trap period, if a particle is in the  $F_{GG}$  flux (flux from the gap between traps to the gap of next column of traps), it will wave (zigzag) around from column to column, staying in the gaps to never be captured (Fig. 4.10(c), an integration of 17 frames of fluorescence images of a  $10 \mu\text{m}$  bead following the zigzag trajectory around the traps). Such an ideal case rarely happens for long arrays as cells are captured, the trap fluidic resistance  $R_T$  increases with time in some traps, so that the cells will likely be displaced from the  $F_{GG}$  flow and end up in a trap. This

suggests randomly arranging traps from column to column, to break up any potential  $F_{GG}$  flow, which was not attempted in this work.

A more sophisticated model was developed and applied to our geometry. The above model ignored the fact that the particles (of finite size) will interact with the unmovable boundaries when they move against the trap structure. Fig. 4.11 shows the schematic of flow field at the center plane of the proposed device channel. The streamlines were extracted from 3-D COMSOL simulations. The flow within the gap between two adjacent traps can be separated into five regions: A: Trap region where particles larger than the critical height will flow directly to the trap and get captured; B: Wall assisted trap 1 region where particles will hit the boundaries of the trap structure and will be pushed by the flow into the trap; C: Zigzag region where particles will moves around the traps and wont be captured; D: Wall assisted trap 2 region where particles will flow around the first column of traps but will flow into Wall assisted trap 1 region of the next column of traps; E: Excluded region where particles cannot exist due to mechanical forces by the trap structure boundaries. When particles size is large, it will be more likely pushed by the trap boundary into the center Trap and Wall assist trap 1 region, which will give rise to increased capture efficiency. Due to periodicity, once the particle moves into the Zigzag region, it will always follow the zigzag trajectory assuming no particle-to-particle interactions and no diffusion of the particle. Therefore, using symmetry, the probability that a particle get trapped flowing through the gap  $G_x$  is

$$p_2 = 1 - \frac{\int_{z_2}^{z_1} u(x)dx}{\int_0^{G_x/2} u(x)dx} \quad (4.6)$$

where  $z_1$  and  $z_2$  are the boundaries of Zigzag region, and  $u(x)$  is the flow profile between the gap. Noted that particles flowing to Excluded region will be pushed to Wall assisted trap 2 region by the trap boundaries. For simplicity, parabolic flow

profile can be used when Reynolds number is much smaller than 1 [81]. The total capture efficiency can thus be calculated as

$$\eta = p_1 + (1 - p_1)p_2 \quad (4.7)$$

The first term is the probability that the particle get trapped by the first column of traps and the second term is the probability that the particle get trapped by the next two columns of traps.

Here we use a simple geometric approach to estimate  $z_1$  and  $z_2$ : extending the boundary of the trap structure of  $d_P/2$  to a point, and then looking back along the streamline from this point to the position  $z_1$  within the gap between two traps. The boundary  $z_2$  can be found using the same method as founding  $z_1$ , as showing in Fig. 4.11. For the proposed device and using the coordinate setup in Fig. 4.11,  $z_1 = 8.5 \mu\text{m}$  and  $z_2 = 6.6 \mu\text{m}$ . So the capture efficiency  $\eta = 82.6\%$  calculated using Eq. 4.7, which is in good agreement with the experiment results.

Note that this model only considered the first three columns of traps, which again should be viewed as an estimation of capture efficiency of the proposed trap array, however with better accuracy than the  $p_1$  estimation that only considered the first column of traps. The estimated capture efficiency using this model was  $\sim 3\%$  and  $\sim 10\%$  smaller than that of experimental results of leukocytes (see Section 4.3) and  $10 \mu\text{m}$  beads (see Section 4.7) measured at the end of the entire device respectively. This difference between theoretical and experimental results can be attributed to the ignoring of filled traps (higher fluidic resistances) and periodically presented support pillars.

However, this model can provide us the information about the trap array performance when changing the experimental conditions. Fig. 4.12 shows the simulated capture efficiencies of particles of different diameters in  $6\text{-}\mu\text{m}$  critical gap trap array

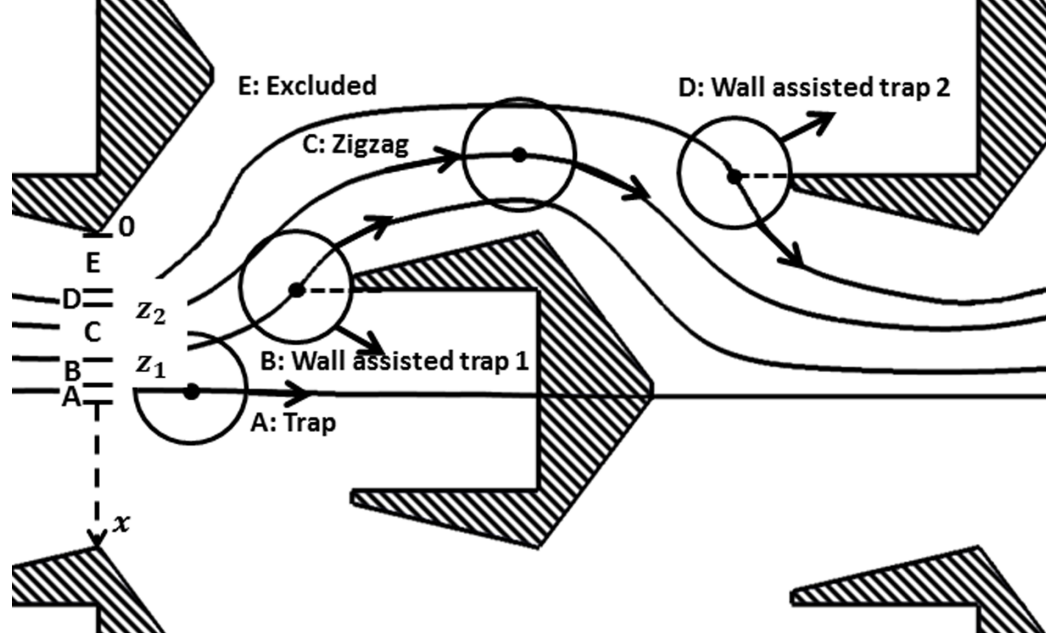


Figure 4.11: Schematic of flow field at the center plane of the proposed device channel. The streamlines were extracted from COMSOL simulations. The fluid flowing through the gap in x-direction can be separated into 5 regions: “Trap”, “Wall assisted trap 1”, “Zigzag”, “Wall assisted trap 2”, and “Excluded”. The circles are of  $10 \mu\text{m}$  diameter.

using this approach. We can see that the capture efficiency increases as the particle diameter increases. The capture efficiency of particles smaller than  $6 \mu\text{m}$  is zero due to the simple fact that they can flow through the critical gap. While particles larger than  $\sim 14 \mu\text{m}$  can be captured 100% by the  $6\text{-}\mu\text{m}$  critical gap trap array, because they will be mechanically displaced by the trap structures to the “Trap” region in the middle of the gaps.

Therefore, to have high capture efficiency, small  $R_T/R_G$  and large particle size are preferred. The former requires large critical gap  $G_C$ . However, as discussed in previous section, cells can pass through the critical gap due to deformation, which gives the upper limit of  $G_C$ . The latter asks for small gap  $G_x$  between two traps, which could introduce clogging when multiple cells flow through the gap. Thus, the no-clogging condition gives the lower limit of  $G_x$ . Using this approach, we can quickly

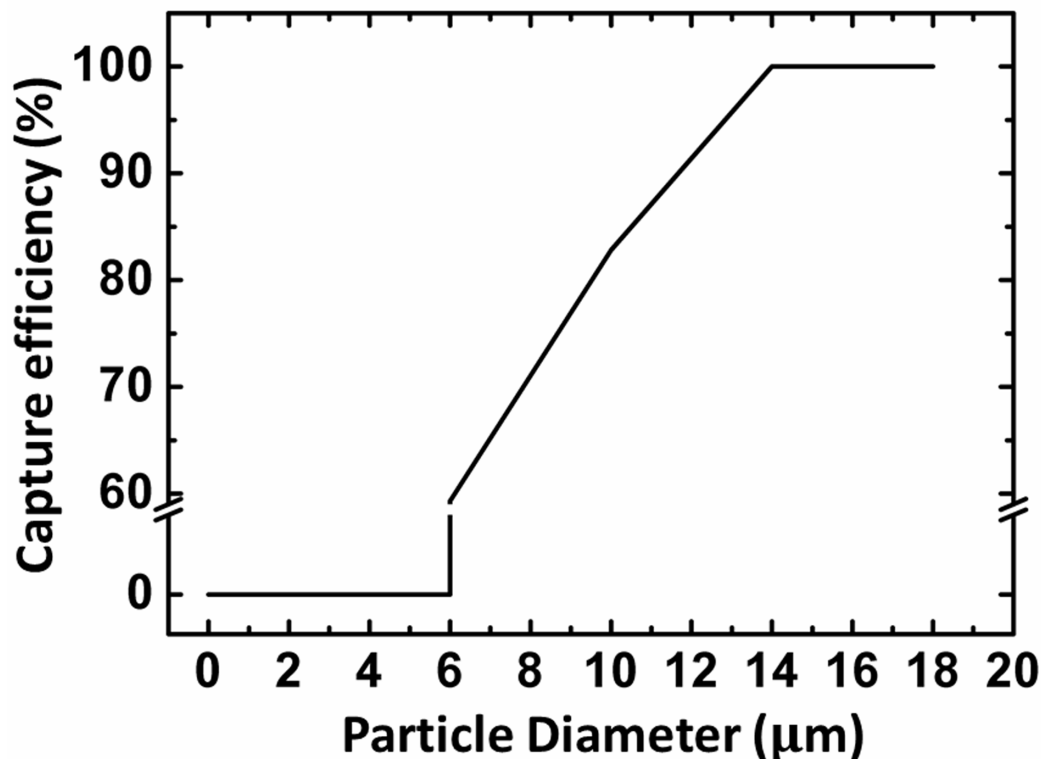


Figure 4.12: The simulated capture efficiencies of particles of different diameters in  $6\text{-}\mu\text{m}$  critical gap trap array using the three-column geometric approach and Eq. 4.7.

modify the design of the proposed device for other automated on-chip cell chemical processing.

## 4.7 Capture Efficiency vs. Device Length

The model developed in Section 4.6 predicted that once the cells or particles flowed into the “zigzag” region, they will always move within in the “zigzag” region. However, an increase in capture efficiency as particles further flowing into the trap array was observed from the experiments. Fig. 4.13(a) shows the measured capture efficiency at the 5th, 10th, 20th, and 53rd device unit of three devices (Device # represents the experimental results measured using device #). To measure the capture efficiency, we first loaded  $10\ \mu\text{L}$  of  $8 \times 10^4$  /mL  $10\text{-}\mu\text{m}$  bead solution to the  $6\text{-}\mu\text{m}$

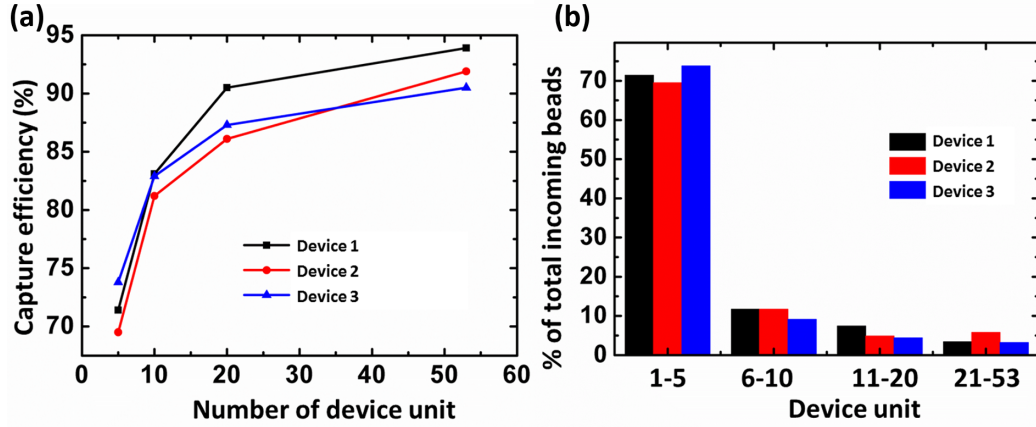


Figure 4.13: (a) Capture efficiency at 5th, 10th, 20th, and 53rd device unit and (b) percentage of total incoming beads captured in 1st–5th, 6th–10th, 11th–20th, and 21st–53rd device units measured in three 6- $\mu\text{m}$  critical gap trap arrays (device 1–3) after loading 10  $\mu\text{L}$  of  $8 \times 10^4$  /mL 10- $\mu\text{m}$  bead solution.

critical gap trap arrays ( $\sim 800$  beads loaded), and then loaded the buffer solution to push the bead solution through the device at 1  $\mu\text{L}/\text{min}$  ( $\approx 460$   $\mu\text{m}/\text{s}$ ). The camera was fixed at the 5th, 10th, 20th, and 53rd (the end of the device) to count the number of beads passing through. There were 328 traps in each device unit. The measured efficiency was about  $\sim 70\%$  at the 5th device unit, and gradually increased to  $\sim 90\%$  at the end of the device channel. Fig. 4.13(b) displays the percentage of total incoming beads captured in 1st–5th, 6th–10th, 11th–20th, and 21st–53rd device units respectively. Most ( $\sim 70\%$ ) of the total incoming beads were captured in the first five device units, while 6th–10th, 11th–20th, and 21st–53rd device units captured about 10%, 5%, 5% of the total incoming beads respectively ( $\sim 90\%$  total capture efficiency). The model predicted capture efficiency for 10- $\mu\text{m}$  beads in 6- $\mu\text{m}$  critical gap device was 82.6% which was about  $\sim 10\%$  smaller than the experimental values. The deviation between the theoretical and experimental results can be attributed to the following two factors. The first is the changing fluidic resistance of filled traps. Once the trap is filled with target cells, the fluidic resistance will increase so that more flux of fluid will flow to the unfilled traps. The second is the presence of support pillars which

can mechanically push the beads to the other streamlines, increasing the probability that the beads to be trapped.

Therefore, to obtain the “zigzag” region’s position, the effects of filled trap structures and the periodically presented support pillars should also be taken into consideration, which gives a capture efficiency of leukocytes and 10  $\mu\text{m}$  about 85% and 90% respectively using the 6- $\mu\text{m}$  critical gap trap array. The leukocytes have a mean cell volume of 187  $\mu\text{m}^3$ , and a standard deviation of 38  $\mu\text{m}^3$  measured using channelyzer system [82]. If we assume a spherical conformation of leukocytes, then leukocytes of 6  $\mu\text{m}$  have cell volume of  $\pi D_{cell}^3/6 = 113.1\mu\text{m}^3$ , where  $D_{cell}$  is the cell diameter. Therefore, leukocytes of diameter smaller than 6  $\mu\text{m}$  (cell volume smaller than 113.1  $\mu\text{m}^3$ ) are about 2.6% of total leukocytes, which means 97.4% of leukocytes are of diameter larger than 6  $\mu\text{m}$  – the critical gap. If we plug in the capture efficiency of 10- $\mu\text{m}$  beads using 6- $\mu\text{m}$  critical gap trap arrays (90%), we can match the capture efficiency of leukocytes to be 97.4% $\times$ 90%  $\approx$  87.7%, which is very close to the leukocyte capture efficiency measured experimentally using 6- $\mu\text{m}$  critical gap trap arrays.

## 4.8 Modelling of Cell Release

The release of particles or cells was difficult in previous works because the trap structures dont have a streamlined shape to avoid clogging and dont have enough open area to have large fluidic force applied on the particles to overcome the resistance force. Some cells, for example leukocytes, form adhesion bonds to the substrate surface, and among themselves to form cell clots in shear flow [78–80], which requires large fluidic force to break the adhesion bonds to release such cells and short incubation time before they start to aggregate. The rectangular shaped traps presented in previous works [11–13] will exert a large mechanical force against the flow direction on cells, when they moving close to the traps, which will greatly decrease the moving speed

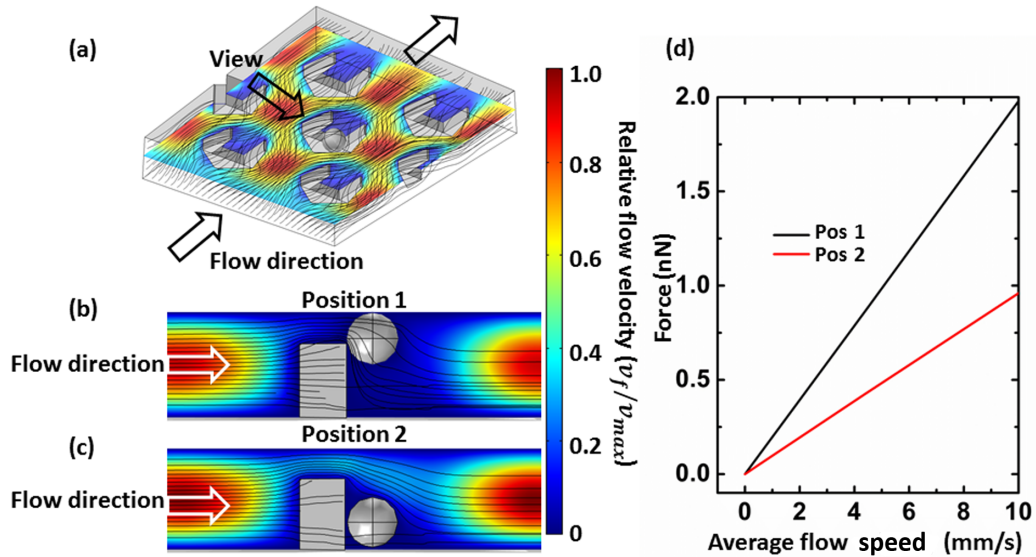


Figure 4.14: (a) Schematic of the COMSOL simulation setup when release a  $10\text{-}\mu\text{m}$  diameter bead and the flow direction. Two positions of particles are evaluated: (b) “Position 1”: bead locating against the Pyrex glass and (c) “Position 2”: bead locating against the silicon surface of the proposed device channel. (d) The simulated release force on a  $10\text{-}\mu\text{m}$  bead at “Position 1” and “Position 2” in  $6\text{-}\mu\text{m}$  critical gap device.

of the cells. When cells flowing in low speed, there is a high chance for them to stick to each other and form clots since they have more time to form the adhesion bonds. However, the streamline shaped traps described in this thesis, on the other hand, will apply less mechanical force against the flow direction on cells than rectangular shaped traps especially in release steps, leading to a reduced clogging of cells.

COMSOL simulations were conducted to estimate the fluidic force applied on particles along the flow direction. Fig. 4.14(a) shows the flow direction and COMSOL simulation setup where a particle is placed in the center of a trap structure. The black arrow labelled with “view” points out the direction of view of Fig. 4.14(b) and (c). Two positions of particles were studied: Fig. 4.14(b) shows particles trapped against the Pyrex glass lid where they receive the maximum fluidic force and Fig. 4.14(c) shows particles located at the bottom of the trap where they receive the minimum fluidic force. Force required to break up the adhesion bonds between cells and different

surfaces ranges from 10 pN to 10 nN [83]. Therefore, the calculated results might be used as a guide to decide the proper release flow rates, if the strength of the adhesion bonds between target cells and surface is known.

Fig. 4.14(d) shows the simulated release force via integration of the total stress along the flow direction on a 10- $\mu\text{m}$  particles surface in a 6- $\mu\text{m}$  critical gap device and various average flow speeds. The fluidic force has a linear relation with the average flow speed, which is consistent with low Reynolds number flow condition where the inertial terms are negligible in the Navier-Stokes equations describing the viscous fluid flow. In the on-chip leukocyte preparation experiments, we tested applying average flow speeds of 4.6 mm/s and 9.2 mm/s to release captured cells in the devices with 6  $\mu\text{m}$  critical gap. The release forces for 10- $\mu\text{m}$  particles are 0.88 nN at “Position 1” and 0.43 nN at “Position 2”, and 1.80 nN at “Position 1” and 0.87 nN at “Position 2” for 4.6 mm/s and 9.2 mm/s release flow speeds respectively.

## 4.9 On-Chip Chemical Processing of Fixed/Permeabilized Cell Samples Using Microfluidic Trap Arrays

### 4.9.1 Introduction

Fixation is often performed in the preparation of biological cells for analytical tests and observations such as electron microscopy [84–86], Raman spectroscopy [87], atomic force microscopy [88], and flow cytometry [89]. After fixation, the biological cells are preserved from decay – autolysis or putrefaction. Fixation terminates any ongoing biochemical reactions, and may also increase the mechanical strength or stability of the treated cells, thus changing the physical properties of the prepared cells. The increase in the mechanical strength or stability (larger Young’s modulus and shear modulus) makes the cells behave more like solid beads in the shear flows,

and enables us to model the cells with simple models, and to process the cells with fewer secondary effects.

After fixation, especially fixation with cross-linking agents such as formaldehyde and glutaraldehyde, a permeabilization step is required to remove the cellular membrane lipids to allow large molecules like antibodies to get inside the cell for intracellular labelling and analysis [90].

Table 4.1: Fixed and permeabilized cell samples

<b>Cell line</b>	<b>Size (<math>\mu\text{m}</math>)</b>	<b>Concentration (/mL)</b>
Unstained K562	13 – 16 [91]	$1.8 \times 10^6$
SYTO 13 stained K562	13 – 16 [91]	$1.5 \times 10^6$
Unstained TF1	$\sim 15$ [92]	$1.8 \times 10^6$
SYTO 13 stained TF1	$\sim 15$ [92]	$1.8 \times 10^6$
Unstained CEM	10 – 14 [93]	$2.9 \times 10^6$
SYTO 13 stained CEM	10 – 14 [93]	$2.0 \times 10^6$

Here we used fixed and permeabilized cells as the target cells to test the performance of the proposed trap arrays with on-chip labelling by SYTO 13 as a demonstration. Fixed and permeabilized cell samples were prepared by our collaborators Min Jung Kim and Prof. Curt Civin (University of Maryland School of Medicine), and shipped to us on ice. For detailed fixation and permeabilization protocols, see Appendix D. Three types of different cancer cell lines were used to be fixed and permeabilized: K562 (myelogenous leukemia cell line), TF1 (erythroleukemia cell line), and CEM (T lymphoblastoid cell line). Table 4.1 lists the fixed/permeabilized cell samples’ information. Since the fixed cells are of 10 – 16  $\mu\text{m}$  and they are more stable with higher mechanical strength, 8- $\mu\text{m}$  critical gap trap arrays were used to have higher capture efficiency and less on-chip clogging.

### 4.9.2 Capture and Release of Fixed/Permeabilized Cells

We first examined the recovery efficiency of the 8- $\mu\text{m}$  critical gap trap arrays using the fixed/permeabilized cell samples. Four devices were used in each experiment, providing 69,536 traps (17,384 traps/device) in total. The fixed/permeabilized cell samples were first 1:10 diluted with 1% kolliphor/PBS buffer and then were loaded to the device at 20  $\mu\text{L}/\text{min}$  (average flow speed 2.3 mm/s) . After the loading step, the captured cells were on-chip incubated for 5 min. The solution at the output reservoir was collected as the “waste”. Pipettes were then used to wash and collect all the remaining liquids in the input and output reservoirs to avoid contamination in the release step. Finally, buffer solution was input from the other direction to release the captured cells at 40  $\mu\text{L}/\text{min}$  (average flow speed 4.6 mm/s) for 10 min to yield the “product” at the output reservoir (the input of loading step).

The “waste” and “product” solution was stored in sterile microcentrifuge tubes and shipped back on ice to University of Maryland School of Medicine for fluorescence-activated cell sorting (FACS) analysis using their flow cytometry facilities.

Fig. 4.15 shows the forward and side scatter plots of the input sample (the first column), “waste” (the second column), and “product” (the third column) of (a) K562, (b) TF1, and (c) CEM cell samples using flow cytometry. Forward scatter correlates with cell size and side scatter is proportional to the granularity of the cells. In this manner, cell populations can often be distinguished based on differences in their size and granularity. As shown in Fig. 4.15, data points categorized in the “Viable” gate are fixed/permeabilized cells, while data points located in the “Beads” gate are counting beads (CountBright Absolute Counting Beads, purchased from Thermo Fisher Scientific, Inc.) of known concentration which were used to measure the cell count in the input sample, “waste”, and “product” solution. Only the forward and side scatter (no fluorescence channels in this case) were considered, because some cells were not fluorescently labelled.

Table 4.2: Recovery efficiency of fixed/permeabilized cells using trap arrays

<b>Name</b>	<b>Total volume (<math>\mu</math>L)</b>	<b>Cell count</b>	<b>Percentage (%)</b>
Experiment 1: fixed/permeabilized K562 cells			
Input sample	130	20,643 cells	100
Waste	90	1,544 cells	7.5
Product	330	11,781 cells	57.1
Clogged	N/A	N/A	35.4
Experiment 2: fixed/permeabilized K562 cells			
Input sample	130	17,932 cells	100
Waste	90	800 cells	7.5
Product	330	10,562 cells	58.9
Clogged	N/A	N/A	33.6
Experiment 3: fixed/permeabilized TF1 cells			
Input sample	140	27,331 cells	100
Waste	90	367 cells	1.3
Product	350	15,904 cells	58.2
Clogged	N/A	N/A	40.5
Experiment 4: fixed/permeabilized TF1 cells			
Input sample	150	21,122 cells	100
Waste	85	184 cells	0.9
Product	345	12,273 cells	55.5
Clogged	N/A	N/A	43.6
Experiment 5: fixed/permeabilized CEM cells			
Input sample	120	33,269 cells	100
Waste	90	583 cells	1.8
Product	345	21,698 cells	65.2
Clogged	N/A	N/A	33.0
Experiment 6: fixed/permeabilized CEM cells			
Input sample	140	11,668 cells	100
Waste	90	151 cells	1.3
Product	325	6,572 cells	56.3
Clogged	N/A	N/A	42.4

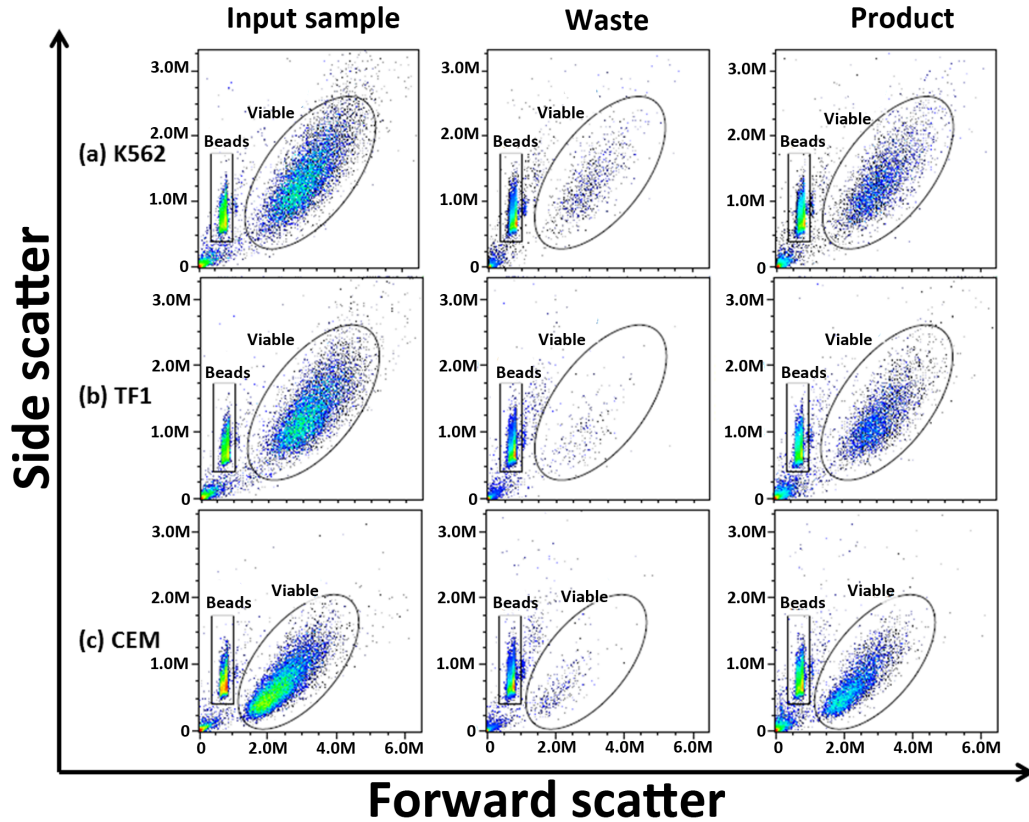


Figure 4.15: Forward and side scatter plots of fixed/permeabilized (a) K562, (b) TF1, and (c) CEM cells. The first, second, and third column is the input fixed/permeabilized cell samples, waste, and product, respectively. The data points categorized in the “Viable” and “Beads” gate are recognized cells and counting beads respectively.

Table. 4.2 shows the detailed experimental results of the fixed/permeabilized cell samples. The recovery efficiency was about 60% for K562, TF1, and CEM cells (the ratio between total cell counts in the “product” solution and the input sample). We can see the cells in the “waste” solution were only <10% of the input sample, indicating 30 – 45% of the input cells were clogged in the device (the results in the “clogged” row of Table. 4.2 was calculated based on the “product” and “waste” cell count). Noted that the number of fixed/permeabilized cells loaded to the device was 5 – 10 × larger than the number of leukocytes loaded to the device (~4,000 leukocytes were input to four devices of 69,536 traps) discussed in previous sections due to the

requirement of flow cytometry analysis, which typically requires  $>10^4$  cells. We later found that on-chip clogging of cells would happen as more cells were input into the device, leading to difficulties in releasing the captured cells (see Section 4.9.4). This clogging may be responsible for the lower cell recovery efficiencies compared to the much higher ( $> 85\%$ ) values of leukocyte recovery efficiency presented in Section 4.5.

### 4.9.3 On-Chip Labelling of Fixed/Permeabilized Cells with SYTO 13

We then tested on-chip labelling with SYTO 13 of fixed/permeabilized cell samples using the  $8\text{-}\mu\text{m}$  critical gap trap arrays. The experimental procedure was similar to that discussed in Section 4.9.2, however, with several changes described as following. Two devices were used in each experiment, providing 34,768 traps (17,384 traps/device) in total, compared to 69,536 traps in Section 4.3. The fixed/permeabilized cell samples were first 1:10 diluted with 1% kolliphor/PBS buffer and then were loaded to the device at  $10\ \mu\text{L}/\text{min}$  for 15 min (average flow speed  $2.3\ \text{mm}/\text{s}$ ) for a total of 25,000 to 45,000 cells. Next the labelling solution (1:200 diluted SYTO 13 in 1% kolliphor/PBS buffer,  $25\ \mu\text{M}$ ) was input to the arrays at  $10\ \mu\text{L}/\text{min}$  for 15 min. The solution at the output reservoir was collected as the “waste”. Pipettes were then used to wash and collect all the remaining liquids in the input and output reservoirs to avoid contamination in the release step. Finally, buffer solution was input from the other direction to release the captured cells at  $20\ \mu\text{L}/\text{min}$  (average flow speed  $4.6\ \text{mm}/\text{s}$ ) for 20 min to yield the “product” at the output reservoir (the input of loading step).

Fig. 4.16 shows the side scatter and SYTO 13 fluorescence intensity plots of on-chip labelling of fixed/permeabilized (a) K562, (b) TF1, and (c) CEM cells. The data points were selected from the “Viable” gate in the forward and side scatter plots as shown in Fig. 4.15. The first column represents the input sample where only a few data points are located in the “SYTO 13 +” gate, meaning most of the input cells were

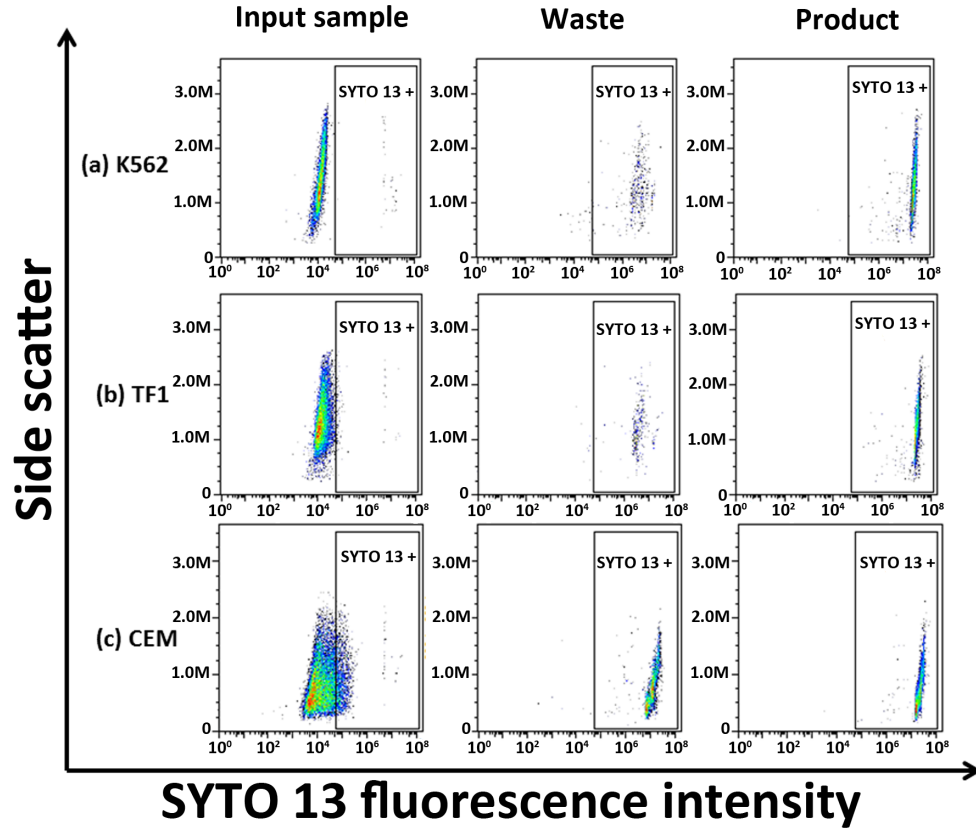


Figure 4.16: Side scatter and SYTO 13 fluorescence intensity plots of on-chip labelling of fixed/permeabilized (a) K562, (b) TF1, and (c) CEM cells. The first, second, and third column is the input fixed/permeabilized cell samples, waste, and product, respectively. The data points were selected from the “Viable” gate in the forward and side scatter plots.

not SYTO 13 fluorescent. The second and third column is the plots of “waste” and “product” solution, respectively.  $\sim 100\%$  of data points are “SYTO 13 +” (labelled by SYTO 13) with an average fluorescence intensity of  $10^6 - 10^7$ . As a comparison, we also performed the conventional 30 min off-chip SYTO 13 labelling of the K562, TF1, and CEM cells with side scatter and SYTO 13 fluorescence intensity plots shown in Fig. 4.17 (for detailed protocols, see Appendix D). The average fluorescence intensity was also about  $10^6 - 10^7$ , however, with a more spread distribution along SYTO 13 fluorescence intensity axis. While the distribution in on-chip labelling plots

(Fig. 4.16) along SYTO 13 fluorescence intensity axis was much narrower, indicating more uniformly labelled cells were prepared using the on-chip labelling conditions.

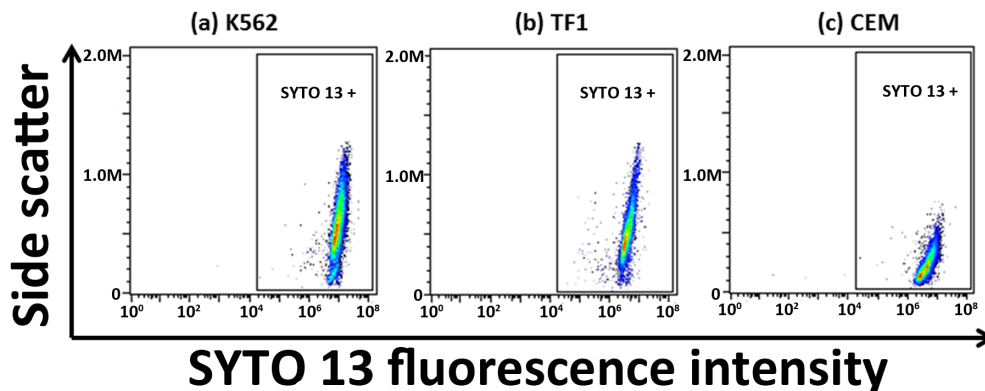


Figure 4.17: Side scatter and SYTO 13 fluorescence intensity plots of conventional 30 min off-chip labelling of fixed/permeabilized (a) K562, (b) TF1, and (c) CEM cells. The data points were selected from the “Viable” gate in the forward and side scatter plots.

The recovery efficiency results of on-chip labelling of fixed/permeabilized cells are listed in Table 4.3. The recovery efficiency ranged from 40% to 56% with about 40% of input cells clogged in the devices, which is similar to the results listed in Table 4.2 where cells were just loaded and released, but not on-chip labelled. Since the experiments conducted in Section 4.9.2 and this section were 2 weeks apart, using the same input cell samples, the similar experimental results indicated better stability of the fixed/permeabilized cells, which is one of the major advantages of fixed/permeabilized cells over unfixed cells.

#### 4.9.4 Clogging of Fixed/Permeabilized K562 Cells in Trap Arrays

As mentioned in Section 4.9.2 and Section 4.9.3, about 40% of input cells were stuck in the array which can neither be collected at the “waste” solution or be released from the trap arrays. The experimental results showed that the clogging of cells

Table 4.3: Recovery efficiency of on-chip labelling of fixed/permeabilized cells using trap arrays

<b>Name</b>	<b>Total volume (<math>\mu\text{L}</math>)</b>	<b>Cell count</b>	<b>Percentage (%)</b>
Experiment 1: fixed/permeabilized K562 cells			
Input sample	150	25,248 cells	100
Waste	350	1,278 cells	5.1
Product	370	14,075 cells	55.7
Clogged	N/A	N/A	39.2
Experiment 2: fixed/permeabilized TF1 cells			
Input sample	150	34,811 cells	100
Waste	350	932 cells	2.7
Product	380	18,895 cells	54.3
Clogged	N/A	N/A	43.0
Experiment 3: fixed/permeabilized CEM cells			
Input sample	150	43,816 cells	100
Waste	370	9,116 cells	20.8
Product	380	17,312 cells	39.5
Clogged	N/A	N/A	39.7

would happen when the total number of input cells was too large. The number of fixed/permeabilized cells (25,000 to 45,000 cells) were input to two devices (34,768 traps) was about 5 – 10 times larger than that of leukocyte experiment (4,000 leukocytes loaded to four devices of 69,536 traps) due to the requirement of flow cytometry to have convincing and readable plots ( $\sim 10^4$  data points). The clogging of cells usually started within the first device unit and then gradually spread all over the entire input region. Once the clogging was formed, it blocked the cells to flow into the trap arrays and prevented the cells to be released in the releasing step.

We investigated this on-chip clogging of cells by loading different numbers of SYTO-13-labelled fixed/permeabilized K562 cells to the trap arrays with camera fixed at the first device unit. In each experiment, two 8- $\mu\text{m}$  critical gap trap arrays were

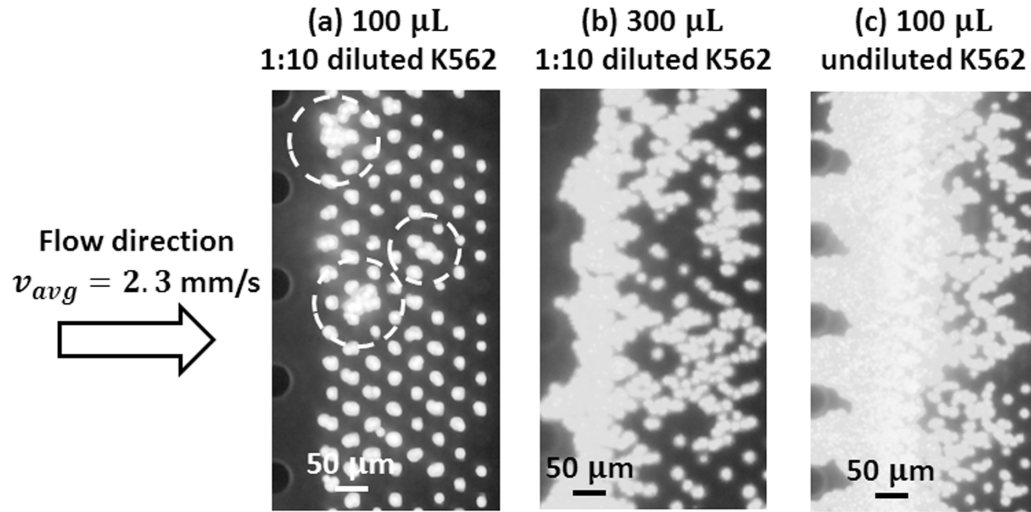


Figure 4.18: Fluorescence images of different numbers of fixed/permeabilized K562 cells loaded to 8- $\mu\text{m}$  critical gap trap arrays at the first device unit: (a) 100  $\mu\text{L}$  1:10 diluted, (b) 300  $\mu\text{L}$  1:10 diluted, and (c) 100  $\mu\text{L}$  undiluted fixed/permeabilized K562 cells. The average input flow speed is 2.3 mm/s.

used. Fig. 4.18 shows the fluorescence images of capture of fixed/permeabilized K562 cells under different conditions at the first device unit using 8- $\mu\text{m}$  critical gap trap arrays. The average input flow speed was set to be 2.3 mm/s. Fig. 4.18(a) is 100  $\mu\text{L}$  1:10 diluted fixed/permeabilized K562 cells loaded to the trap array – about  $2 \times 10^4$  cells were input to the trap array. Most of the traps only captured one cell. However, there were traps that captured more than one cell (dashed circle in Fig. 4.18(a)), which can be viewed as “seeds” for formation of cell clots. We then loaded 200  $\mu\text{L}$  more 1:10 diluted fixed/permeabilized K562 cells to the trap arrays –  $6 \times 10^4$  cells in total. A clear “wall” of clogged cells can be viewed at the beginning at the first device unit with most of the traps capturing more than one cell (Fig. 4.18(b)). Fig. 4.18(c) is 100  $\mu\text{L}$  undiluted fixed/permeabilized K562 cells were input to the trap array – about  $2 \times 10^5$  cells in total. The clogging of cells spread all over the first device unit. Few cells can flow across this barrier and it was very difficult to release the clogged cells.

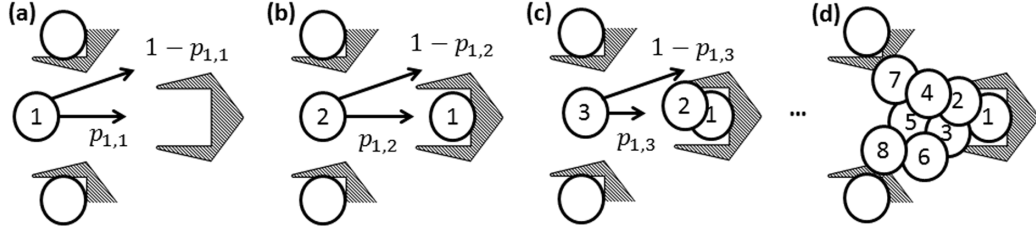


Figure 4.19: Possible mechanism of on-chip clogging of cells in trap array. Suppose the previous column of traps are filled with cells, the “first” cell has a probability  $p_{1,1}$  and  $1 - p_{1,1}$  to be and not to be captured by the trap, respectively (a). If the “first” cell is not captured, then the next coming cell becomes the “first” cell. When the trap captures the “first” cell, the “second” cell has a probability  $p_{1,2}$  and  $1 - p_{1,2}$  to be and not to be captured by the trap, respectively (b). Again, if the “second” cell is not captured, then the next coming cell becomes the “second” cell. When the number of input cells is large enough, the trap has a probability  $\sim 100\%$  to capture the “second” cell. Similarly, we can infer that the trap has a probability  $\sim 100\%$  to capture the “third”, “fourth”, etc. cell. Once the trap captures enough cells, it become a “seed” for clogging formation (d).

Here we developed a simple qualitative model to describe the clogging formation of cells. As shown in Fig. 4.19, assume the previous column of traps are filled with cells, the “first” cell coming to the trap has a probability  $p_{1,1}$  and  $1 - p_{1,1}$  to be and not to be captured by the trap, respectively. Here  $p_{1,1} \approx p_1 = R_T / (R_T + R_G)$ . Thus,  $p_{1,1} \approx 10.5\%$  and  $16.1\%$  for  $6$  and  $8\text{-}\mu\text{m}$  critical gap trap arrays, respectively. If the “first” cell is not captured, then the next coming cell becomes the “first” cell. When the trap captures the “first” cell, the “second” cell has a probability  $p_{1,2}$  and  $1 - p_{1,2}$  to be and not to be captured by the trap, respectively. Again, if the “second” cell is not captured, then the next coming cell becomes the “second” cell.  $p_{1,2}$  is usually a small value, because most open region of the trap is filled by the “first” cell. However, if the number of input cells is large enough, the trap has a probability  $\sim 100\%$  to capture the “second” cell. Using the same approach, we can infer that the trap can capture the “third”, “fourth”, etc. cell with  $\sim 100\%$  probability if the number of input cells is large enough. When the trap captures enough cells, it becomes a “seed” for clogging formation of cells, as shown in Fig. 4.19(d).

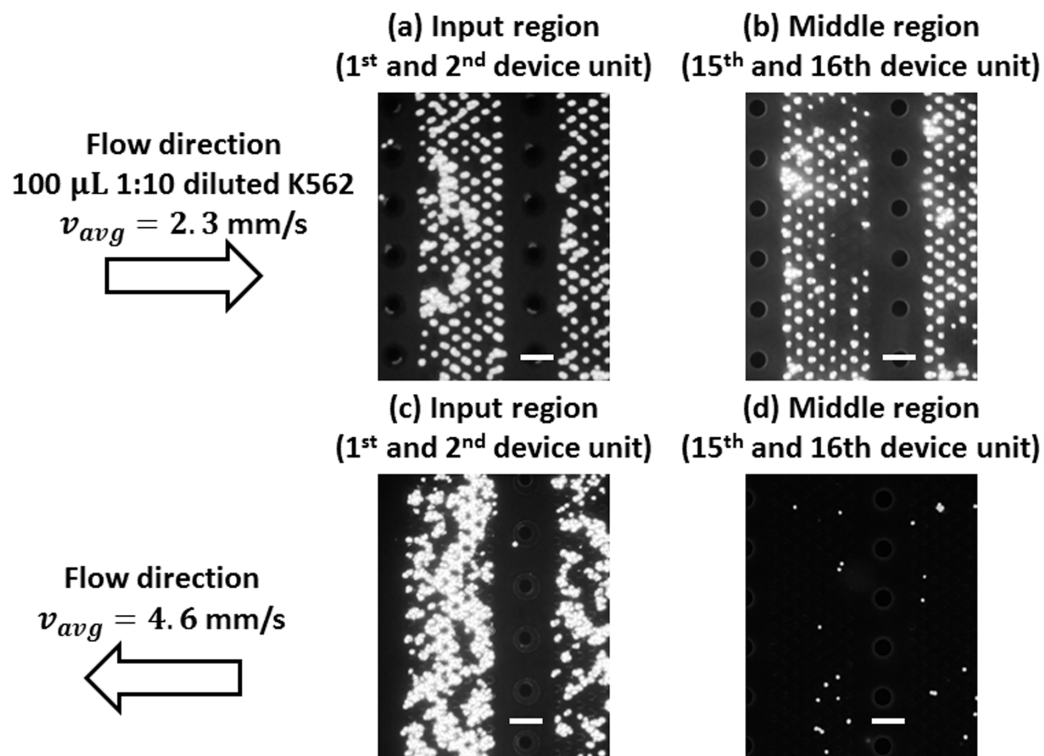


Figure 4.20: Release of fixed/permeabilized K562 cells from 8- $\mu\text{m}$  critical gap trap arrays after loading 100  $\mu\text{L}$  1:10 diluted fixed/permeabilized K562 cells to the device. The loading and releasing flow speed is 2.3 mm/s and 4.6 mm/s, respectively. (a) and (c) are the input region (1<sup>st</sup> and 2<sup>nd</sup> device unit) after loading and after releasing, respectively. (b) and (d) are the middle region (15<sup>th</sup> and 16<sup>th</sup> device unit) after loading and after releasing, respectively. The scale bar is 100  $\mu\text{m}$ .

Release of cells from the clogged trap arrays is difficult. Microscopic observation of the product solution showed that there were only a few cells can be recovered from the trap array under conditions shown in Fig. 4.18(b) and (c). The condition shown in Fig. 4.18(a) was similar to that tested in Section 4.9.2 and Section 4.9.3 where 100 – 150  $\mu\text{L}$  1:10 diluted fixed/permeabilized cells were input. We tried to release fixed/permeabilized K562 cells from 8- $\mu\text{m}$  trap arrays after loading 100  $\mu\text{L}$  1:10 diluted fixed/permeabilized K562 cells at 2.3 mm/s flow speed (10  $\mu\text{L}/\text{min}$  flow rate) to the device. The release was flowing the buffer from the other direction at 4.6 mm/s average flow speed for 20 min. Fig. 4.20(a) and (b) show the input region (1<sup>st</sup> and 2<sup>nd</sup> device unit) and middle region (15<sup>th</sup> and 16<sup>th</sup> device unit) of the trap array

after the loading step. Fig. 4.20(c) and (d) show the input and middle region after the releasing step. We can see that most of the cells can be released from the middle region of the device. However, the cells aggregated at the beginning of the device (Fig. 4.20(c)). The clogging formed in the releasing step can be attributed to the fact that more cells will pass through the input region than the middle region during the releasing step. As cells flowing together, they are likely to form clots that cannot be released from the device. The clogging of cells in the releasing step accounts for the 40% of the input cells that cannot be recovered from the device described in Section 4.9.2 and Section 4.9.3.

To avoid the on-chip clogging of cells during the loading and releasing steps, one might try either decreasing the number of input cells or increasing the number of trap arrays used. However, the former is limited by the requirement of analysis methods (often more prepared cells are preferred). The latter will increase the total area consumption, thus limited by the fabrication technology. Another approach could be better design of the trap structure such that each trap can only contain one cell, which however is difficult due to the huge variations among biological cells. One better strategy can be varying the gap size of device units. For example, we can set a large value of the vertical gap size of the first several device units, so the traps of the first several device units will have a very low probability to capture cells. The large gaps also provide large open area for cells to flow through in the releasing step. We then gradually decrease the vertical gap size along the device. Therefore, the later traps will have a higher probability to capture cells. As a result of this arrangement, the clogging at the beginning of the device can be avoided, and an overall high recovery efficiency can be achieved.

## 4.10 Summary and Outlook

A microfluidic device has been demonstrated for on-chip cell chemical processing via capture and release using array of trap structures, with streamlined shapes to avoid clogging in capture and release steps and support pillars between two adjacent device units to control the critical gap. A qualitative model was developed to help better understand and design the proposed trap structure array. We demonstrated that  $\sim 84\%$  leukocyte capture efficiency and  $\sim 99\%$  release efficiency can be achieved with moderate flow speeds and on-chip incubation times, and a model was presented to explain the devices superior performance. On-chip leukocyte labelling with SYTO13 and washing using the proposed devices showed similar results to conventional off-chip labelling.

Then we examined fixed/permeabilized cells as target cells with on-chip SYTO 13 labelling for flow cytometry analysis as a demonstration. The on-chip labelling showed better results (more uniformly labelled cells) than conventional 30-min off-chip labelling. However, the recovery efficiency was about 40 % to 60 %. Due to the requirement of flow cytometry analysis, 5 – 10 times more cells were input to the trap array, often leading to on-chip clogging of cells. A qualitative model was developed to explain the possible mechanism of on-chip clogging with solutions to resolve this problem.

These results suggest the device could be used for automated processing to replace many conventional steps for the preparation of cells for flow cytometry and other analytical measurements.

A comparison of the trap structure for on-chip cell chemical processing with the three continuous-flow approaches of Chapter 3 is presented in Section 6.2.

# Chapter 5

## Concentrating Genomic-Length DNA Using DLD Arrays

### 5.1 Introduction

After the extraction and lysis of cells, DNA sequencing can be performed to read out the genomic information of the prepared cells. The first step in mapping and sequencing a genome, or parts of it, is typically extraction and purification of genomic-length double stranded DNA molecules. These extremely long molecules have contour lengths of 10-1000  $\mu\text{m}$ , and there are basically two ways to sort and concentrate them according to length: (i) by gel electrophoresis at very low fields (and correspondingly long, multiday run times) to avoid elongation of the spherical random coils that these molecules form in solution [94], (ii) by full elongation either in crossed fields [95, 96] or via stretching in nanochannels [97].

While stretching of the DNA, either in post arrays or in nanochannels, is an attractive technology that is rapidly growing in popularity [98], it does not easily scale to high single-molecule throughput, which is needed for preparative work [99]. However, most techniques that do not deliberately stretch the DNA rely on a conformation of

the molecule that is as close to spherical as possible. Indeed, the first attempt to sort DNA in a nanofabricated device [100] failed precisely because DNA is so easily elongated in shear fields. Thus, the shear elongation of very long DNA molecules is not only a fascinating problem in polymer physics, its understanding and modulating is also of great impact in biotechnology where failure to control the shear moduli in large biopolymers can be very costly.

Here we raise and control the shear modulus of coils of genomic-length DNA well enough to concentrate them up to 87-fold at high speed and continuous flow using DLD arrays. This is the first step towards high-speed, high-throughput sorting of such DNA according to length with the same technology.

Our collaborators Ezra S. Abrams and T. Christian Boles at Sage Science, Inc. suggested the use of polyethylene glycol (PEG) to compact the DNA (Section 5.3), and Jonas N. Pedersen and Henrik Flyvbjerg at Department of Micro- and Nanotechnology, Technical University of Denmark contributed to the theoretical analysis (Section 5.5).

## 5.2 Device Design

Fig. 5.1 shows a schematic of the proposed device. It is fabricated in silicon by conventional photolithography technology and deep anisotropic etching. For details of the array construction and fabrication see Appendix B. Fig. 5.1(a) demonstrates DLD array design with migration angle  $\theta=3.8^\circ$ , post size of  $6.3 \mu\text{m}$ , and gap size of  $1.7 \mu\text{m}$ . The array is of circular posts arranged in rows tilted towards the central wall. Fig. 5.1(b) shows the schematic of the device. The real device is 21 times longer than wide, 1.4 mm wide,  $10 \mu\text{m}$  deep, and symmetric about the central wall. A low-concentration DNA solution enters through the ten inlet channels, flows through the central DLD array region where it is concentrated from 87 channels on each side to 1

on each side, and leaves through the 17 outlet channels. The three output channels closest to the wall are the product outlets.

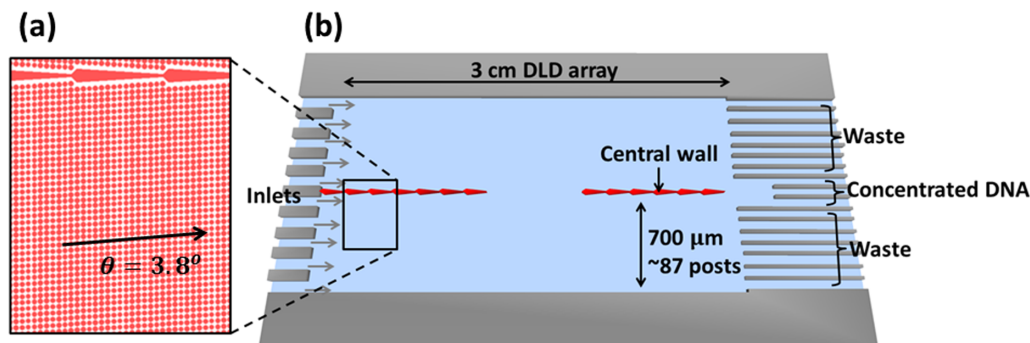


Figure 5.1: DNA concentrator using DLD arrays with migration angle  $\theta=3.8^\circ$ . (a) Array of circular posts arranged in rows that are tilted towards the central wall, which is also shown. (b) Schematic of the device. (The real device is 21 times longer than wide, 1.4 mm wide, 10  $\mu\text{m}$  deep, and symmetric about the central wall.) DNA molecules enter via the inlet region, concentrate along the central (red) wall, and are collected at the product outlets. All particles that follow the  $3.8^\circ$ -tilted rows of posts, have concentrated at the central wall when they flowed 1 cm into the device, for they have flowed 1 cm into the array, for a net concentration of  $\times 87$  before exiting the device.

The separation method of DLD array relies on particles being globular, and not easily deformable by the flow. Minimal deformation is important because particles should be pushed (bumped) into adjacent stream lines by posts blocking their flow along stream lines, giving rise to nonhydrodynamic forces which break time and velocity inversion symmetry. Particles too small or too soft will follow the laminar flow in its zigzag trajectory around posts. A coiled polymer “particle” (such as genomic-length DNA) may elongate along the flow lines in response to the shear forces that it encounters in the array. If it is elongated so much that its short axis is shorter than the critical size, it will follow the zigzag path of the flow lines through the array, and hence not displace laterally.

### 5.3 PEG Compacts DNA by Depletion Force

Polyethylene glycol (PEG) is often used for DNA compaction and precipitation [101–105]. The centers of PEG molecules cannot come closer to a DNA strand than the radius of a PEG molecule. Thus each DNA molecule is surrounded by a zone that is depleted of centers of PEG molecules: PEG is restricted to the complement of these depletion zones. When depletion zones overlap, they take up less space, and hence their complement is larger. This increase in PEG-accessible volume increases the entropy of the PEG solution, which lowers its free energy. This causes an entropic force that favors increasing overlaps between depletion zones. At low number concentrations  $c$  of PEG, the pressure that compress overlapping depletion zones is  $ck_B T$  [106]. This compression of depletion zones results in DNA compaction. Therefore PEG’s presence causes an attractive depletion force [107] between surfaces less than one PEG diameter apart and hence between such parts of DNA in a coil that can come close to each other (Fig. 5.2).

The possibility of using depletion force to hold long DNA molecules in a relatively firm globular confirmation should allow use of rapid, scalable continuous-flow methods for DNA manipulation [108, 109]. One such application pursued in this thesis is a “DNA concentrator” which should concentrate genomic-length DNA molecules. Fig. 5.3 shows the micrograph composite of purified 166 kbp T4 DNA in a solution with 10% PEG (w/v) in a flow with a peak speed of  $30 \mu\text{m/s}$ . The DNA concentrates along the central wall as it moves through the DLD array.

### 5.4 Experimental Results

For details of the DNA preparation procedure, see Appendix E. Fig. 5.4 shows fluorescent micrographs of purified 166 kbp T4 DNA under different conditions in the DLD array. At zero fluid speed and with no PEG in the solution, DNA is in a glob-

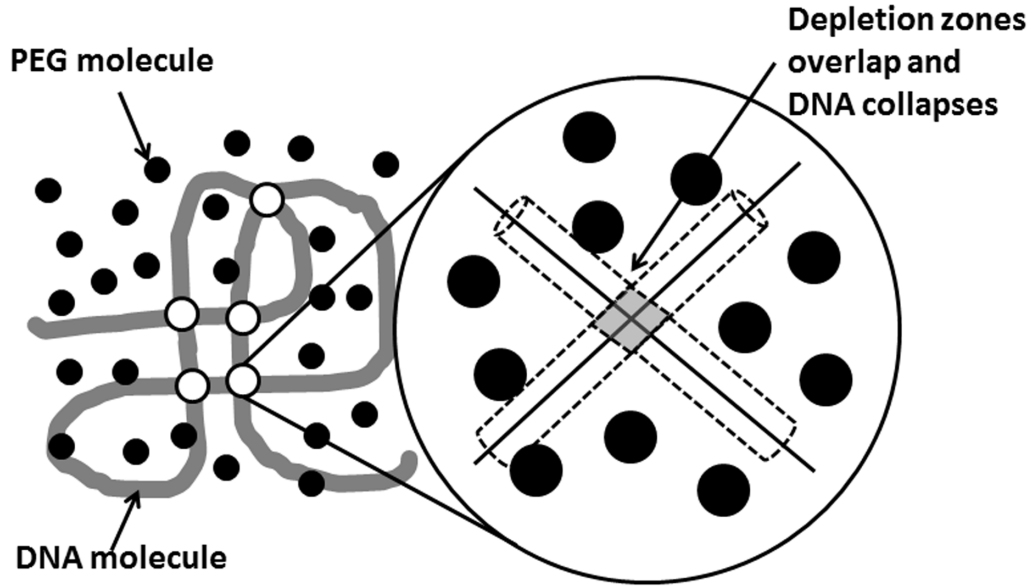


Figure 5.2: Depletion force induced by PEG crowding. The centers of PEG molecules cannot come closer to a DNA strand than the radius of a PEG molecule. Thus each DNA molecule is surrounded by a zone that is depleted of centers of PEG molecules: PEG is restricted to the complement of these depletion zones. When depletion zones overlap, they take up less space, and hence their complement is larger. This increase in PEG-accessible volume increases the entropy of the PEG solution, which lowers its free energy. This causes an entropic force that favors increasing overlaps between depletion zones. At low number concentrations  $c$  of PEG, the pressure that compresses overlapping depletion zones is  $ck_B T$  [106]. This compression of depletion zones results in DNA compaction.

ular conformation as expected, only slightly deformed by the presence of the posts (Fig. 5.4(a)). The blue concentric circles have radii of 1 and 2  $\mu\text{m}$ , respectively.

Now consider a fixed fluid flow of, say, 20  $\mu\text{m/s}$  peak speed between posts. The flow shears in the bump array because of the flow’s no-slip boundary condition at the surfaces of the posts. Without PEG in the solution, videos of DNA’s motion through the array show that the DNA changes dynamically between globular and elongated conformations, as previously observed in shear flows [110]. We use the easily measured extent of the molecule in the direction of the flow to characterize its conformation (Fig. 5.5), while its transverse extent, which triggers the “bumping” or “zigzag” mode, is difficult to measure.

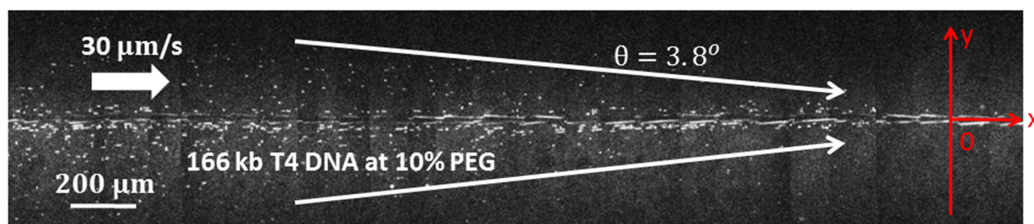


Figure 5.3: Micrograph composite of purified 166 kbp T4 DNA in a solution with 10% PEG (w/v) in a flow with a peak speed of  $30 \mu\text{m/s}$ . The DNA concentrates along the central wall as it moves through the DLD array.

Fig. 5.4(b) shows an example of a molecule sheared at a peak flow speed of  $v_{x,max} = 20 \mu\text{m/s}$  and elongated up to  $17 \mu\text{m}$ , i.e.,  $\sim 30\%$  of its contour length. The effective width of the sheared molecule is smaller than the critical size of the DLD array, and consequently, the DNA molecule follows a zigzag path through the array. No lateral displacement takes place (gray area in Fig. 5.6).

Adding PEG to the solution qualitatively changes the behavior of the DNA in the array. For a flow rate of  $20 \mu\text{m/s}$ , even 5% PEG makes the conformation of DNA less extended, with length  $\sim 8 \mu\text{m}$  (Fig. 5.4(c)). This conformation “bumps” through the array, moving along a tilted row of posts (white area in Fig. 5.6), in contrast to the motion without added PEG (Fig. 5.4(b)). However, increasing the PEG concentration to 15% diminishes the size of the DNA to a value below the critical size of the DLD array, and the DNA follows the flow again. Thus to concentrate DNA at the central wall, the PEG concentration must be tuned so the DNA can resist the shear force in the gaps between the posts, but remains sufficiently large to bump at the posts—the PEG concentration must be within the white area in Fig. 5.6. Fig. 5.4(e) and (f) show two micrograph composites of DNA flowing at 10% and 5% PEG concentrations respectively, and the flow speeds are  $30 \mu\text{m/s}$  and  $50 \mu\text{m/s}$  respectively. Therefore (e) is within the white area in Fig. 5.6, and DNA follows the migration angle of the tilted array in a “bumping” trajectory. While (f) is in the gray area in Fig. 5.6. The

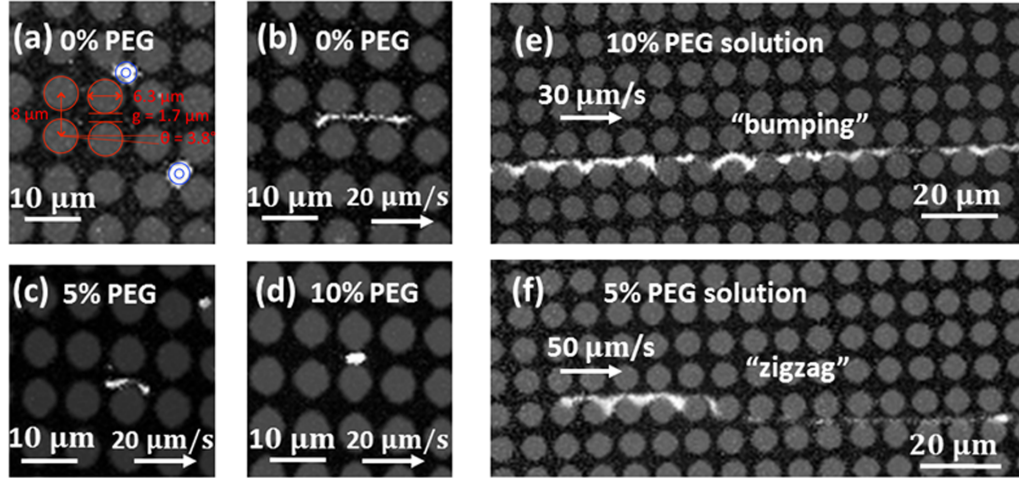


Figure 5.4: Purified 166 kbp T4 DNA in DLD array. (a) No PEG added and no flow. The DNA coils up to a sphere like object, slightly deformed by the posts. The concentric circles have radii  $R_g = 1 \mu\text{m}$  and  $2R_g$ , respectively, with  $R_g$  the estimated radius of gyration. (b), (c), (d) 0%, 5%, and 10% PEG concentrations, respectively, all at flow speed  $20 \mu\text{m/s}$ . In (b) the DNA is elongated by the shear flow and reaches a length of  $\sim 17 \mu\text{m}$ , i.e.,  $\sim 30\%$  of its contour length. It follows the flow through the array. With PEG present, (c), (d), DNA is stretched less by the shear flow. At high PEG concentrations, DNA can maintain a globular conformation in the shear flow; hence, it behaves like a solid particle and is laterally displaced deterministically. (e) and (f) micrograph composites of DNA flowing at 10% and 5% PEG concentrations respectively. (e) The flow speed is  $30 \mu\text{m/s}$  and DNA follows the migration angle of the tilted array in a “bumping” trajectory. (f) The flow speed is  $50 \mu\text{m/s}$ . The elongation of DNA makes its short axis shorter than the critical size of DLD array. Thus, the DNA follows the flow through the array in a “zigzag” trajectory.

elongation of DNA makes its effective width smaller than the critical size of DLD array. Thus, the DNA follows the flow through the array in a “zigzag” trajectory.

## 5.5 Theory

A coarse statistical model of a DNA molecule in solution is provided by a freely jointed chain of  $N = L/\kappa$  segments, where  $L$  is the contour length of the DNA,  $\kappa = 2L_p$  its Kuhn length, and  $L_p$  its persistence length [111]. For T4 DNA molecules stained with YOYO-1,  $L \approx 1.12 \times 56 \mu\text{m} \approx 63 \mu\text{m}$  [112] and  $L_p = 0.050 \mu\text{m}$ , which

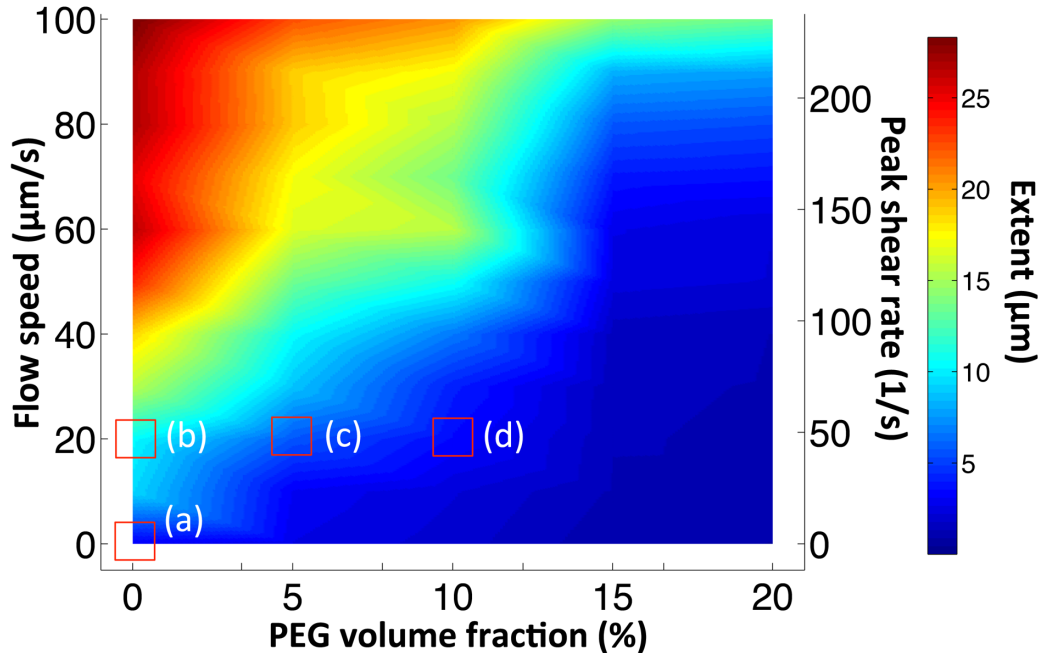


Figure 5.5: Measured map of the average extent along the flow for 166 kbp T4 DNA as a function of PEG concentration and peak flow speed or peak shear rate. This map is based on experimental data recorded at 30 points in the 2-D space, those marked with circles in Fig. 5.6. Letters (a)-(d) refer to panels in Fig. 5.4. The right  $y$ -axis (peak shear rate) was calculated from the flow speed (left  $y$ -axis) using Eq. 5.1.

gives  $N \approx 630$  segments. Without PEG in the solution and no flow, this simple model for the DNA conformation predicts that DNA forms a coil that is described as a three-dimensional random walk with  $N$  steps, each step equal to a Kuhn length. This leads to a Gaussian density distribution. The radius of gyration for the coil is  $R_g = \sqrt{R_0^2/6} = \sqrt{\langle \mathbf{R} \rangle^2 / 6} = 2L_p\sqrt{N/6} \approx 1\mu\text{m}$  [111], where  $\mathbf{R}$  is the end-to-end distance of the molecule. Although this estimate is a lower bound for the size of the molecule since excluded volume effects are not included [113], the diameter of the molecule is larger than the gap between the posts, and it is much larger than the critical size  $D_c \approx 0.7\mu\text{m}$  for hard spheres. Fig. 5.4(a) shows how the posts deform the DNA coil even in the absence of flow. In the presence of a fluid flow, DNA molecules experience a shear stress from the flow's shear [27]. This shear deforms the DNA as observed in Fig. 5.4(b). According to theory [114], DNA will elongate when the

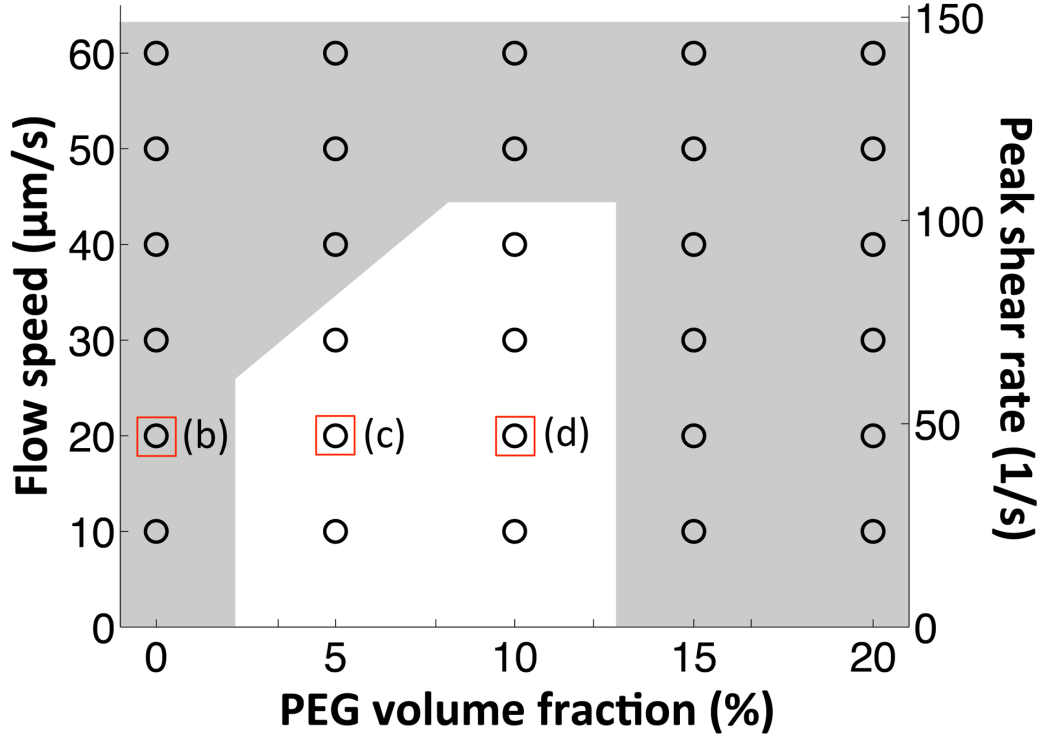


Figure 5.6: Map showing which PEG concentrations and flow speeds or peak shear rates will concentrate 166 kbp T4 DA (white area) or not (gray area) in the bump array in Fig. 5.4. The map is based on measurements done at the value marked with open circles. The transition between concentrated output or not is abrupt as a function of the PEG concentration and flow speed because of the large number of posts encountered by a molecule passing through the array. Letters (b)-(d) refer to panels in Fig. 5.4.

Weissenberg number  $Wi = \dot{\gamma}\tau \simeq 1$ , where  $\dot{\gamma}$  is the applied shear rate, and  $\tau$  is the natural relaxation rate of the polymer. Assuming a parabolic flow profile in gaps of width between posts [9],  $v_x(y) = v_{x,max}[1 - (1 - 2y/g)^2]$  for  $0 < y < g$ , and the shear rate in the gap is

$$\dot{\gamma} = \frac{dv_x}{dy} = \frac{4v_{x,max}}{g}\left(1 - \frac{2y}{g}\right). \quad (5.1)$$

That is, the shear rate varies linearly with position between the peak value  $\pm 4v_{x,max}/g$  at the post walls, and vanishes at the center of the gap. To estimate the relaxation time, we use the scaling relation [114]

$$\tau \simeq \frac{0.2\eta R_{coil}^3}{k_B T} \quad (5.2)$$

where  $\eta = 8.9 \times 10^{-4}$  Pa·s is the viscosity of water, and  $R_{coil}$  is the unperturbed coil radius. Setting  $R_{coil}$  equal to the average end-to-end distance  $R_0$  gives the relaxation time  $\tau \approx 0.7$  s. This relaxation time depends crucially on the value of  $R_{coil}$ , so we compare it with experimental relaxation times for  $\lambda$ -DNA molecules at viscosities  $\eta_\lambda$  60 and 220 times larger than water's [110]. Assuming the scaling relation in Eq. 5.2 holds and that the size  $R_{coil}$  of the molecules scales as the square-root of the contour length, we can estimate a relaxation time for a T4-DNA molecule in water from the relation

$$\tau_{T4} = \frac{\eta_{water}}{\eta_\lambda} \left( \frac{\sqrt{L_{T4}}}{\sqrt{L_\lambda}} \right)^3 \tau_\lambda \quad (5.3)$$

where  $L_\lambda = 22\mu\text{m}$  is the contour length of a  $\lambda$ -DNA molecule stained with one YOYO-1 molecule per 4 bp [112]. The measured relaxation times are  $\tau_\lambda = 6.3$  and 19 s at the two viscosities. That gives  $\tau_{T4} = 0.5$  and 0.4 s, respectively, in good agreement with our estimate.

For  $\tau = 0.7$  s, the corresponding Weissenberg numbers are in the range  $\pm(1.6\text{s}/\mu\text{m})v_{x,max}$ . Even for the lowest experimentally controllable flow velocities,  $v_{x,max} \sim 10\mu\text{m/s}$ , is  $Wi \gg 1$  except in a small region around the center of a gap. So the DNA will undergo a coil-stretch transition when passing through a gap, and no lateral displacement will occur. Now consider the effect of adding a small flexible polymer, such as PEG, to a solution containing DNA. Then the depletion force explained in Fig. 5.2 sets in. As the concentration of PEG is increased, the DNA undergoes a coil-globule transition [104]. This changes the radius of the DNA molecule from the coil value  $R_g$  at zero PEG to a much smaller value  $R_m$ . The transition has been described both theoretically [107, 115] and experimentally [102]. The latter showed that the coil-globule transitions happens at a PEG concentration

in the range from 11% to 19% with a possible first-order transition, i.e., with a coexisting phase.

A simple estimate for the minimum radius  $R_m$  that can be reached by depletion forces is

$$\frac{4\pi}{3}R_m^3 = Nv_c \quad (5.4)$$

where  $v_c \approx \kappa^2 w$  is the excluded volume of a Kuhn segment [113], and  $w = 10$  nm is the effective diameter of DNA. Here it is, plausibly, assumed that the persistence length  $L_p$  and effective diameter  $w$  of the DNA are not changed by the compacting caused by the depletion forces. For T4-DNA molecules, the expected value is  $R_m \approx 0.25\mu\text{m}$ . This is approximately a factor of four smaller than the aqueous value, and about 3 times larger than the radius both of T4 DNA compacted with PEG-A and visualized with transmission electron microscope [116], and of the T4 capsid head [117]. Importantly, this estimate is also significantly lower than the critical size  $D_c \approx 0.7\mu\text{m}$ .

## 5.6 Discussion

From the map in Fig. 5.5, we can understand the DNA molecules' behavior in DLD arrays. For PEG concentrations higher than 10%-15%, DNA molecules have the globular conformation and will not be concentrated at the central wall in the DLD array used here. They are too small. So instead, they zigzag through the array, following flow lines. For lower PEG concentrations the situation is more complex. Without PEG, the DNA is sheared by even the smallest accessible flow speeds and becomes elongated, to lengths of 10  $\mu\text{m}$  or more as seen in Fig. 5.5. In a window of moderate PEG concentrations (5%-10%) and moderate flow speeds ( $v_{x,max} \lesssim 40\mu\text{m/s}$ ), the DNA molecules are displaced laterally and concentrate at the central wall (Fig. 5.6). At these PEG concentrations, the critical peak shear rate  $4v_{x,max}/g$  is  $\sim 100$   $\text{s}^{-1}$ .

The parameter regime for which concentration occurs depends on the geometry of the array. Consider, e.g., decreasing the gap size  $g$  while not reducing  $v_{x,max}$  proportionally. That will increase the peak shear rate ( $\pm 4v_{x,max}/g$ ) in the gap, which will (i) lower the maximum flow speed ensuring separation and (ii) increase the PEG concentration needed to prevent the DNA from shearing. Decreasing the gap size  $g$  will also decrease the critical size  $D_c$  of the array [27], which leads to bumping at higher PEG concentrations. In summary, the white area in Fig. 5.6 is shifted towards higher PEG concentrations and lower flow speeds.

## 5.7 Summary and Outlook

We have demonstrated how the extent and shear modulus of DNA conformations can be controlled by depletion force. This control was put to practical use in a DLD array that consequently could concentrate DNA molecules in a continuous flow: The DNA was concentrated to a single bump channel, i.e., 87-fold concentration before exiting—with throughput up to  $0.25 \mu\text{L/h}$  (at  $40 \mu\text{m/s}$  in white area in Fig. 5.6). One can increase the concentration by more than a factor 87 by using a wider array, which also will increase the throughput.

As a potential application, purification of DNA from enzymatic reactions used to produce next-generation DNA sequencing libraries typically require a series of enzymatic processing steps, each step ending with purification of the DNA products away from the modifying enzyme. Since the processing enzymes are orders of magnitude smaller than their DNA substrates, DLD arrays provide a promising mechanism for DNA purifications in a flow-based microfluidic system. At the right combination of flow speed and PEG concentration, processed DNA products will bump laterally through the DLD array, preferably into collection channels containing enzyme-free

buffer, while the enzymes follow the laminar flow path straight down the array, away from the DNA.

# Chapter 6

## Conclusion

### 6.1 Summary

We hope to develop a system for on-chip preparation of biological cells using microfluidic arrays with high recovery efficiency, long on-chip incubation time, and low contamination of the treatment chemical in the prepared cells for a broad range applications.

We first discussed the development of a microfluidic system driven by continuous flow for on-chip cell preparation using DLD arrays. The device first presented by K. J. Morton, et al. [7] utilizing conventional DLD arrays can be used for on-chip platelet labelling with R6G and on-chip cell lysis. However, there was no microfluidic structure to control the diffusion of treatment chemical, thus the diffusion of treatment chemical happened all through the array. For on-chip preparation of leukocytes from raw blood, the conventional DLD arrays can only provide  $\sim 10\text{--}100$  ms to achieve desired level of contamination of treatment chemical in the prepared cells ( $\sim 0.01$  the concentration of treatment chemical at the input of treatment stream).

To resolve the trade-off between incubation time and the contamination of treatment chemical, two separator walls were introduced to the conventional DLD array.

The target cells were first concentrated along the first separator wall for an extended on-chip incubation. The first separator wall also confined the diffusion of treatment chemical in a smaller region to reduce the contamination of treatment chemical. By implementing the second separator wall, the diffusion of treatment chemical can be further suppressed when the flow speed was low. We demonstrated on-chip leukocyte labelling with R6G ( $20 \mu\text{g}/\text{mL}$ ) with a 4 s incubation and  $\sim 0.067$  relative output contamination (and  $\sim 1$  s incubation with  $\sim 0.02$  relative output contamination) at the product output.

To further increase the incubation time, an integrated device of two symmetric 3-zone DLD arrays and two very long serpentine channels was proposed. The first DLD array harvested the leukocytes from a diluted blood sample into a central channel. The concentrated leukocytes were then directed to the incubation serpentine channel for long time on-chip incubation. The second 3-zone DLD array was used to perform the on-chip washing to remove the unreacted labels. A dummy serpentine channel was placed at the outputs of the first 3-zone DLD array to balance the fluidic resistances. We developed an analogous circuit model to determine the correct flow rates of the sample, treatment, and washing stream for on-chip cell preparation. On-chip leukocyte labelling with R6G ( $20 \mu\text{g}/\text{mL}$ ) was demonstrated using this device with a 2.3 min incubation and  $\sim 0.02$  relative output contamination, an increase of  $\sim 100\times$  over the separator wall design and  $> 1,000\times$  of the simple design for similar levels of relative output contamination. While this is a significant improvement, many applications require another factor of 10 increase in incubation time, to reach 10 – 20 min.

We then discussed the development of a microfluidic device for on-chip cell chemical processing via capture and release using array of trap structures: streamlined shapes avoiding clogging in capture and release steps and support pillars between two adjacent device units to control the critical gap. A qualitative model was devel-

oped to help better understand and design the proposed trap structure array. We demonstrated that  $\sim 84\%$  leukocyte capture efficiency and  $\sim 99\%$  release efficiency can be achieved with moderate flow speeds and on-chip incubation times, and a model was presented to explain the devices superior performance. On-chip leukocyte labelling with SYTO13 and washing using the proposed devices as a demonstration showed similar results to conventional off-chip labelling. Fixed/permeabilized cell samples were also examined using  $8\text{-}\mu\text{m}$  critical gap trap arrays with on-chip SYTO 13 labelling for flow cytometry analysis as a demonstration. The on-chip labelling showed better results than conventional 30 min off-chip labelling in terms of labelling uniformity. A possible mechanism of on-chip clogging, which leads to decreased recovery efficiency, was discussed and modelled with solutions proposed to resolve this problem.

Finally, We demonstrated concentrating genomic-length DNA using microfabricated DLD arrays via depletion force introduced by PEG molecule crowding. The DNA was concentrated to a single bump channel, i.e., 87-fold concentration before exiting—with throughput up to  $0.25\ \mu\text{L}/\text{h}$  ( $40\ \mu\text{m}/\text{s}$  flow speed in the array). One can increase the concentration by more than a factor 87 by using a wider array, which also will increase the throughput. This study is the first step toward high-speed and high-throughput DNA concentration using DLD arrays.

## **6.2 Comparison between DLD and Trap Arrays for On-Chip Preparation of Biological Cells**

Recovery efficiency, incubation time, and contamination are the three major parameters that we used to evaluate the device performance for on-chip cell preparation throughout this thesis. Table 6.1 shows the experimental results for on-chip leukocyte preparation of these three parameters of conventional DLD array, DLD array

with separator walls, DLD array with serpentine channels, and trap array described in this thesis. The contamination is evaluated as the relative output contamination, which is the ratio of the concentration of the treatment chemical at the product output to that of the treatment chemical at the treatment stream input. These results suggest these devices could be used for automated on-chip preparation of biological cells to replace many conventional steps for the preparation of cells for flow cytometry and other analytical measurements.

Table 6.1: Summary for on-chip leukocyte preparation using microfluidic arrays

<b>Name</b>	<b>Recovery efficiency (%)</b>	<b>Incubation time</b>	<b>Relative output contamination</b>
Conventional DLD array	~ 85%	10–100 ms	0.01–0.1
DLD array with separator walls	~ 85%	1–10 s	0.01–0.1
DLD arrays with serpentine channels	50–72%	1–10 min	0.001–0.01
Trap array	70–85%	1–20 min	0.001

Note that the trap array has similar recovery efficiency and contamination level of treatment chemical as DLD arrays, however, with longer on-chip incubation time. It is also better to run the trap array with only one type of input cell – the target cells, due to the fact that once the trap structure is filled with the target cell, the other cells could also be captured by the trap even if their size is smaller than the critical gap. Therefore, the trap arrays cannot totally replace the DLD arrays for applications of on-chip preparation of biological cells. A better strategy could be harvesting the target cells using DLD arrays and then processing them using trap arrays with a properly designed fluidic control system.

Another concern for on-chip preparation of biological cells is the amount of treatment chemicals used to effectively process the cells. The amount of treatment chem-

Table 6.2: Chemical use for different processes using off-chip approach, DLD arrays with serpentine channels or trap arrays

Name	SYTO 13 ( $\mu\text{L}$ )*	Monoclonal Antibodies ( $\mu\text{L}$ )**
Off-chip labelling	5	20
DLD arrays with serpentine channels	20	2,000
Trap array	$\sim 5$	$\sim 20$

\* off-chip labelling with SYTO 13: Add 5  $\mu\text{L}$  SYTO 13 to 1 mL raw blood and incubate for 10 min at room temperature.

\*\* off-chip labelling with monoclonal antibodies: Add 20  $\mu\text{L}$  monoclonal antibodies to 20  $\mu\text{L}$  leukocyte enriched solution (leukocytes of 1 mL raw blood are concentrated into 20  $\mu\text{L}$  solution) and incubate for 10 min at room temperature.

ical should be used for different labelling processes using off-chip approach, DLD arrays with serpentine channels or trap arrays is listed in Table 6.2. The off-chip labelling protocols were provided by our collaborators Min Jung Kim and Prof. Curt Civin at University of Maryland School of Medicine. These labelling processes require an incubation of 10 min, so only the DLD arrays with serpentine channels and trap arrays are considered here. The off-chip leukocyte labelling with SYTO 13 protocol is adding 5  $\mu\text{L}$  SYTO 13 to 1 mL raw blood and then incubating the solution at room temperature for 10 min. Therefore, the SYTO 13 is 1:200 diluted. To achieve comparable on-chip labelling results, the concentration of treatment chemical and incubation time should be kept the same. For DLD arrays with serpentine channels, the sample input was usually 1:4 diluted blood solution to avoid on-chip clogging of cells, and the treatment chemical stream was running at the same flow rate as that of the sample stream. Therefore, to process 1 mL raw blood using DLD arrays with serpentine channels, 4 mL 1:200 diluted SYTO 13 solution should be input to on-chip label the leukocytes assuming all treatment chemical will flow to the incubation serpentine channel, which is 20  $\mu\text{L}$  SYTO 13 without dilution. The protocol for off-chip leukocyte labelling with monoclonal antibodies is adding 20  $\mu\text{L}$  monoclonal

antibodies to 20  $\mu\text{L}$  leukocyte enriched solution (leukocytes of 1 mL raw blood are concentrated into 20  $\mu\text{L}$  solution) and then incubation at room temperature for 10 min. Therefore, the monoclonal antibodies are 1:2 diluted. Again, to achieve comparable on-chip labelling results, 4 mL 1:2 diluted monoclonal antibodies should be input to the DLD arrays with serpentine channels, which is 2 mL monoclonal antibodies and is not practical since monoclonal antibodies are often expensive. Unlike the continuous flow driven DLD arrays, during the on-chip labelling using trap arrays, treatment chemical solution is not flowing or flowing at very low flow rate to keep a stable concentration of the treatment chemical for better labelling results. Therefore, the amount of treatment chemical should be used for on-chip chemical processing using trap arrays is about the same as or slightly more than that used in off-chip labelling.

### **6.3 Future Work**

This thesis focused on the on-chip preparation of cells and DNA for later analysis. Most of the work focused on on-chip leukocyte preparation using DLD arrays and trap arrays. The device designs were optimized for this application. However, there are many other cell types whose preparation steps for measurement and analysis might be replaced by the proposed approaches, such as bacteria, circulating tumor cells (CTCs), and fungi cells. Different types of biological cells could have different properties: bacteria may be more likely to stick to the silicon posts, CTCs deform easily in shear flows, etc. Therefore a better understanding of the target cells is important for developing such on-chip preparation applications.

The experimental results in this thesis have shown that high-speed and high-throughput applications for on-chip preparation of biological cells using microfluidic arrays are possible, however there is still a great room for device integration and

optimization. For higher recovery efficiency, more arrays of different design with different critical sizes can be integrated together. For higher flow speed, more device can be run in parallel, where the balance of fluidic resistances of the devices, and the device yield rate (devices usually are fabricated on a single wafer) are critical.

Right now, the devices are made of silicon, which is prohibitively expensive. A more suitable material can be cheap, easy-obtained, and biodegradable plastics. The development of corresponding fabrication methods to have accurate feature size as designed is thus important.

# Appendix A

## Publications and Presentations

### A.1 Peer-reviewed Publications

- **Y. Chen**, R. H. Austin, and J. C. Sturm, “On-chip chemical processing of biological cells by capture and release using microfluidic trap arrays” (in preparation).
- C. I. Civin, T. Ward, A. M. Skelley, K. Gandhi, Z. Lee Peilun, C. R. Dosier, J. L. D’Silva, **Y. Chen**, M. J. Kim, J. Moynihan, et al., “Automated leukocyte processing by microfluidic deterministic lateral displacement”, *Cytometry Part A* 89, no.12 (2016): 1073–1083.
- **Y. Chen**, J. D’Silva, R.H. Austin, and J.C. Sturm, “Microfluidic chemical processing with on-chip washing by deterministic lateral displacement arrays with separator walls”, *Biomicrofluidics* 9, no.5 (2015): 054015-10.
- **Y. Chen**, E.S. Abrams, T.C. Boles, J.N. Pedersen, H. Flyvbjerg, R.H. Austin, and J.C. Sturm, “Concentrating Genomic Length DNA in a Microfabricated Array”, *Physical Review Letters* 114 (2015): 198303-5.

## A.2 Conference Presentations

- **CYTO 2016**, Seattle, WA. ““Car Wash”: An Integrated Continuous-Flow Microfluidic Device to Prepare Leukocytes for Flow Cytometry by Deterministic Lateral Displacement” (poster).

- **APS March Meeting 2016**, Baltimore, MD. “How to Concentrate Genomic Length DNA in a Microfabricated Array” (talk).

- **NHGRI Advanced DNA Sequencing Technology Development Meeting 2015**, San Diego, LA. “Nano-Bump Array for Ultra-High Speed Sorting of Oligonucleotide DS-DNA” (talk).

- **MRS Spring Meeting & Exhibit 2014**, San Francisco, LA. “Reduction of Output Contamination in On-chip Chemical Treatment and Washing Using Separator Walls in Deterministic Lateral Displacement Arrays” (talk).

- **Physical Sciences in Oncology Symposium 2014**, Bethesda, MD. “Rapid On-chip Leukocyte Labelling and Washing Using Wall-Separated Deterministic Lateral Displacement Arrays” (poster).

# Appendix B

## Fabrication Process

This appendix details the device fabrication process using conventional photolithography technology. Devices are fabricated on single-side-polished 100-mm-diameter, 600- $\mu\text{m}$ -thick silicon wafers.

### B.1 Etching

The masks are designed using L-Edit software and are fabricated by Heidelberg DWL66 laser writer at Princeton Micro/Nano Fabrication Laboratory (MNFL) or Photo Sciences, Inc. on chrome coated glass lithographic templates.

#### B.1.1 Silicon Wafer Preparation

1. Dehydration bake the silicon wafer at 95 °C for 2 min
2. Spray HMDS and spin immediately using recipe 1 (4000 rpm 40 s).

#### B.1.2 $<20 \mu\text{m}$ Etching

1. Apply  $\sim 3$  mL AZ 1518 photoresist using a plastic transfer pipette and spin using recipe 1 (4000 rpm 40 s).

2. Soft bake at 95 °C for 1 min.
3. Expose using Channel 2 and 25  $\mu\text{m}$  hard contact setting on the mask aligner (Karl Suss, MA6) for 25 s.
4. Develop using AZ 300 MIF developer for 1 min.
5. Inspect under microscope to ensure features are completely developed. If not, develop using AZ 300 MIF developer for extra 10 s and then repeat this step until features are completely developed.
6. Etch using recipe 2 (20  $\mu\text{m}$  trench) on the Samco RIE800iPB for Deep Reactive Ion Etching (DRIE). 1 cycle  $\approx$  0.2  $\mu\text{m}$ .

### **B.1.3 >20 $\mu\text{m}$ Etching**

1. Apply  $\sim$ 3 mL AZ 4330 photoresist using a plastic transfer pipette and spin using recipe 3 (3000 rpm 40 s).
2. Soft bake at 95 °C for 3 min.
3. Expose using Channel 2 and 25  $\mu\text{m}$  hard contact setting on the MA6 mask aligner for 1 min.
4. Develop using AZ 300 MIF developer for 2 min.
5. Inspect under microscope to ensure features are completely developed. If not, develop using AZ 300 MIF developer for extra 10 s and then repeat this step until features are completely developed.
6. Etch using recipe 3 (200  $\mu\text{m}$  trench) on the Samco RIE800iPB . 1 cycle  $\approx$  1.3  $\mu\text{m}$ .

## B.2 Device Clean

After the etching steps, a clean process should be performed to remove the remaining photoresist and other contaminations. This process starts with acetone, isopropanol, and DI water rinsing in a sequential order, followed by a Piranha and HF clean.

### B.2.1 Piranha Clean

1. Use clean plastic tweezers or PTFE dipper basket to handle the silicon chip.
2. Bake the chip at 95 °C for at least 2 min to ensure no liquid solvent (acetone, isopropanol, ethanol, etc.).
3. Add 30% hydrogen peroxide slowly to 96% sulfuric acid in a 1:1 ratio to form the Piranha solution in a glass beaker.
4. Immerse the chip in Piranha solution for 30 min (The Piranha solution can be heated at 70 °C for better cleaning).
5. Rinse the chip under DI water.
6. Wait until the Piranha solution cool down to room temperature before drain it in an appropriate acid waste container.

### B.2.2 HF Clean

1. Prepare 2% HF solution in a PTFE beaker.
2. Immerse the chip in 2% HF solution for 10 min.
3. Rinse the chip under DI water.

## B.3 Device Sealing

Three sealing techniques are used to form the transparent “lid” layer of the device for optical observation.

### B.3.1 Tape Sealing

1. Apply 3M 9795R polyolefin sealing tape to the chip surface.
2. Use a plastic roller to carefully push out the air trapped between the sealing tape and chip.
3. Remove the extra tape outside the chip area.

**Advantage:** simple and quick sealing procedure to test device principle.

**Disadvantage:** cannot hold at high input pressure (flow rate  $< 10$  cm/s), low uniformity, autofluorescence introducing fluorescence noise.

### B.3.2 PDMS Sealing

1. Oxygen plasma the chip surface to increase its hydrophilicity (for stronger bonding, 100 nm silicon dioxide layer can be introduced by a thermal furnace at 1000 °C for 30 min).
2. Apply  $\sim 5$  mL liquid PDMS on a 0.2-mm-thick cover glass (purchased from Ted Pella, Inc.) and spin at 2000-3000 rpm for 30 s.
3. Bake the PDMS-cover glass lid in a 60 °C oven for at least 3 hr.
4. Oxygen plasma the PDMS side to increase its hydrophilicity.
5. Carefully apply the PDMS-cover glass lid to the chip (PDMS facing the silicon surface) and use a glass blade to remove the extra part outside the chip area.

**Advantage:** no fluorescence background noise

**Disadvantage:** cannot hold at very high input pressure (flow rate  $< 1$  m/s), less uniformity.

### B.3.3 Anodic Bonding

1. Stack a piece of Pyrex glass (purchased from Dell Optics Co., Inc.) onto the silicon chip on a hot plate. Ensure both the glass and silicon chip are super cleaned.

2. Gradually increase the hot plate's temperature to 500 °C.
3. Apply 600 V voltage to the glass-silicon structure for about 2 hr with cathode electrode connected to the Pyrex glass and anode electrode connected to the silicon chip.
4. When the device area is sealed, turn off the hot plate and voltage source, and wait until the hot plate to cool down to room temperature.

**Advantage:** can hold at very high input pressure (flow rate up to 10 m/s), very high uniformity.

**Disadvantage:** complicate and time consuming process.

# Appendix C

## Blood Protocols

This appendix details protocols used to obtain and prepare blood sample.

### C.1 Buffer Preparation

Two types of buffer for experiments involving blood: (i)1% BSA and (ii)1% Kolliphor are prepared. The protocol is as following.

1. Add 500 mL phosphate buffered saline (PBS) with calcium and magnesium ions removed (purchased from Fisher Scientific) into a plastic bottle.
2. Add 5 g (i) bovine serum albumin (BSA, Fraction V, Heat Shock Treated, purchased from Fisher Scientific) or (ii) Kolliphor P 188 (purchased Sigma-Aldrich, Inc.).
3. Add Ethylenediaminetetraacetic acid (EDTA, Anhydrous, Crystalline, purchased from Sigma-Aldrich, Inc.) to have a final concentration at least 5 mM and not more than 7.5 mM.
4. Magnetic stir the solution in a chamber degassed using a vacuum pump. The dissolving process usually takes 2 hr.
5. Filter the solution with 0.2  $\mu\text{m}$  pore size filters into a clean sterile plastic bottle.

## C.2 Whole Blood Sample Preparation

Venous EDTA-anticoagulated blood (purchased from Interstate Blood Bank, Inc.) can be diluted with the buffer (usually 1:3 or 1:10) to form the blood sample solution. 40  $\mu$ M D-Phenylalanyl-prolyl-arginyl Chloromethyl Ketone (PPACK) can be added to the sample to reduce on-chip clogging for long time device operation [71].

Some experiments may require the blood sample to be pre-labeled. SYTO 13, a nucleic acid stain, is often used. 6  $\mu$ L SYTO 13 (purchased from Fisher Scientific) is added to every 1 mL blood as purchased. The solution is then incubated at room temperature for 10 min.

## C.3 RBC Lysed Blood Sample Preparation

1. Add 1 mL blood (as purchased) or labelled blood (without dilution) to a clean sterile plastic centrifuge tube.
2. Add 10 mL 1 $\times$  RBC lysis buffer (purchased from eBiosciences).
3. Incubate the solution at 4  $^{\circ}$ C for 30 min.
4. Centrifuge at 2000  $\times$ g for 20 min.
5. Collect the pellet (mostly leukocytes) and then resuspend in the 1% BSA or 1% Kolliphor buffer.

# Appendix D

## Fixation and Permeabilization Protocol

This appendix details protocols used to obtain and prepare fixed and permeabilized K562, TF1 and CEM cell samples.

1. Harvest and wash cells, and re-suspend cells in 7.5ml of PBS/2.5% FBS buffer.
2. Split each cell line sample into 2 sterile centrifuge tubes (one for unstained sample and the other for SYTO13 stained sample;  $\sim 3.3$  mL per each tube).
3. SYTO13 staining: Incubate cells with SYTO13 for 30min on ice (Final SYTO 13 concentration is about 5 $\mu$ M).
4. Wash cells with PBS/2.5%FBS buffer twice.

### **Fixation/Permeabilization**

5. Re-suspend the cell pellets with BD Cytofix/Cytoperm solution (1ml solution per  $5 \times 10^6$  cells) and incubate for 30min.
6. Wash cells with 20ml of 1X BD Perm/Wash buffer twice.
7. Re-suspend cell pellets in 1X BD Perm/Wash buffer (to make final cell concentration about  $1 - 2 \times 10^6$  cells/mL).
8. Store samples at 4°C.

# Appendix E

## DNA Staining

This appendix details the DNA sample preparation protocols described in 5.4.

### E.1 Running buffer

$\beta$ -mercaptoethanol is used as an antibleaching agent.

1. Add 900 mL of DI water to a clean sterile plastic bottle.
2. Add 100 g 2% w/v pluronic F108.
3. Add 20 mL 50 $\times$  TE buffer.
4. Mix the solution thoroughly and filter it through 0.2  $\mu$ m sterile filter.
5. When running experiments, aliquot 10 mL prepared solution to a clean sterile centrifuge tube.
6. Add 50  $\mu$ L  $\beta$ -mercaptoethanol to form the running buffer.

### E.2 DNA staining

The ratio between dye molecule and base pair is 1:5.

1. Add 1090  $\mu$ L TE buffer to a clean sterile microfuge tube.
2. Add 130  $\mu$ L 5 M NaCl solution.

3. Add 13  $\mu\text{L}$   $\beta$ -mercaptoethanol.
4. Add 40  $\mu\text{L}$  33 ng/ $\mu\text{L}$  166 kbp T4 DNA (1:10 diluted in 50 $\times$  TE buffer as purchased from Promega Co.).
5. Add 29  $\mu\text{L}$  10  $\mu\text{M}$  YOYO-1 solution (purchased from Thermo Fisher Scientific Inc.).
6. Incubate the prepared solution at 50  $^{\circ}\text{C}$  for 1 hr. The concentration of YOYO labeled DNA is 1 ng/ $\mu\text{L}$ .
7. When running experiments, aliquot 400  $\mu\text{L}$  YOYO labeled DNA to a clean sterile centrifuge tube.
8. Add 20 mL running buffer. The final concentration of DNA molecule is  $\sim$ 20 pg/ $\mu\text{L}$ .

# Bibliography

- [1] M. Toner and D. Irimia. Blood-on-a-chip. *Annu. Rev. Biomed. Eng.*, 7:77–103, 2005.
- [2] A. Manz, N. Graber, and H. Widmer. Miniaturized total chemical analysis systems: a novel concept for chemical sensing. *Sensors and actuators B: Chemical*, 1(1-6):244–248, 1990.
- [3] M. A. McClain, C. T. Culbertson, S. C. Jacobson, N. L. Allbritton, C. E. Sims, and J. M. Ramsey. Microfluidic devices for the high-throughput chemical analysis of cells. *Analytical chemistry*, 75(21):5646–5655, 2003.
- [4] J. Nguyen, Y. Wei, Y. Zheng, C. Wang, and Y. Sun. On-chip sample preparation for complete blood count from raw blood. *Lab on a Chip*, 15(6):1533–1544, 2015.
- [5] A. J. Mach, J. H. Kim, A. Arshi, S. C. Hur, and D. Di Carlo. Automated cellular sample preparation using a centrifuge-on-a-chip. *Lab on a Chip*, 11(17):2827–2834, 2011.
- [6] A. P. Tan, J. S. Dudani, A. Arshi, R. J. Lee, T. K. Henry, D. R. Gossett, and D. Di Carlo. Continuous-flow cytomorphological staining and analysis. *Lab on a Chip*, 14(3):522–531, 2014.
- [7] K. J. Morton, K. Loutherbach, D. W. Inglis, O. K. Tsui, J. C. Sturm, S. Y. Chou, and R. H. Austin. Crossing microfluidic streamlines to lyse, label and wash cells. *Lab on a Chip*, 8(9):1448–1453, 2008.
- [8] J. A. Davis, D. W. Inglis, K. J. Morton, D. A. Lawrence, L. R. Huang, S. Y. Chou, J. C. Sturm, and R. H. Austin. Deterministic hydrodynamics: taking blood apart. *Proceedings of the National Academy of Sciences*, 103(40):14779–14784, 2006.
- [9] D. W. Inglis, J. A. Davis, T. J. Zieziulewicz, D. A. Lawrence, R. H. Austin, and J. C. Sturm. Determining blood cell size using microfluidic hydrodynamics. *Journal of immunological methods*, 329(1):151–156, 2008.
- [10] A. Huebner, D. Bratton, G. Whyte, M. Yang, C. Abell, F. Hollfelder, et al. Static microdroplet arrays: a microfluidic device for droplet trapping, incubation and release for enzymatic and cell-based assays. *Lab on a Chip*, 9(5):692–698, 2009.

- [11] D. Di Carlo, N. Aghdam, and L. P. Lee. Single-cell enzyme concentrations, kinetics, and inhibition analysis using high-density hydrodynamic cell isolation arrays. *Analytical chemistry*, 78(14):4925–4930, 2006.
- [12] D. Di Carlo, L. Y. Wu, and L. P. Lee. Dynamic single cell culture array. *Lab on a Chip*, 6(11):1445–1449, 2006.
- [13] A. M. Skelley, O. Kirak, H. Suh, R. Jaenisch, and J. Voldman. Microfluidic control of cell pairing and fusion. *Nature methods*, 6(2):147–152, 2009.
- [14] H. Baatz, M. Steinbauer, A. G. Harris, and F. Krombach. Kinetics of white blood cell staining by intravascular administration of rhodamine 6g. *International Journal of Microcirculation*, 15(2):85–91, 1995.
- [15] M. W. Berns, A. Dahlman, F. M. Johnson, R. Burns, D. Sperling, M. Gultinan, A. Siemens, R. Walter, W. Wright, M. Hammer-Wilson, et al. In vitro cellular effects of hematoporphyrin derivative. *Cancer Research*, 42(6):2325–2329, 1982.
- [16] R. Mcmillan and J. L. Scott. Leukocyte labeling with 51chromium. *Blood*, 32(5):738–754, 1968.
- [17] B. H. Mock and D. English. Leukocyte labeling with technetium-99m tin colloids. *J Nucl Med*, 28:1471–1477, 1987.
- [18] J. G. McAfee, G. Subramanian, G. Gagne, R. F. Schneider, and C. Zapf-Longo. 99m tc-hm-pao for leukocyte labelingexperimental comparison with 111 in oxine in dogs. *European Journal of Nuclear Medicine and Molecular Imaging*, 13(7):353–357, 1987.
- [19] H. Kelbæk, J. Linde, and S. L. Nielsen. Evaluation of a new leukocyte labeling procedure with 99m tc-hmpao. *European Journal of Nuclear Medicine and Molecular Imaging*, 14(12):621–623, 1988.
- [20] Y. Chen, J. D’Silva, R. H. Austin, and J. C. Sturm. Microfluidic chemical processing with on-chip washing by deterministic lateral displacement arrays with separator walls. *Biomicrofluidics*, 9(5):054105, 2015.
- [21] Y. Chen, E. S. Abrams, T. C. Boles, J. N. Pedersen, H. Flyvbjerg, R. H. Austin, and J. C. Sturm. Concentrating genomic length dna in a microfabricated array. *Physical review letters*, 114(19):198303, 2015.
- [22] E. M. Purcell. Life at low reynolds number. *American journal of physics*, 45(1):3–11, 1977.
- [23] C. A. Stan, A. K. Ellerbee, L. Guglielmini, H. A. Stone, and G. M. Whitesides. The magnitude of lift forces acting on drops and bubbles in liquids flowing inside microchannels. *Lab on a Chip*, 13(3):365–376, 2013.

- [24] H. Wang, P. Iovenitti, E. Harvey, and S. Masood. Optimizing layout of obstacles for enhanced mixing in microchannels. *Smart materials and structures*, 11(5):662, 2002.
- [25] K. Loutherbach. *Microfluidic Devices for High Throughput Cell Sorting and Chemical Treatment*, volume 73. Citeseer, 2011.
- [26] Lotien Richard Huang, Edward C Cox, Robert H Austin, and James C Sturm. Continuous particle separation through deterministic lateral displacement. *Science*, 304(5673):987–990, 2004.
- [27] D. W. Inglis, J. A. Davis, R. H. Austin, and J. C. Sturm. Critical particle size for fractionation by deterministic lateral displacement. *Lab on a Chip*, 6(5):655–658, 2006.
- [28] K. J. Morton, J. C. Sturm, R. H. Austin, and S. Y. Chou. Nanoimprinted fluidic device for continuous separation of nanoparticles. *Proc of  $\mu$  TAS*, 1:1014–1016, 2006.
- [29] D. W. Inglis, K. J. Morton, J. A. Davis, T. J. Zieziulewicz, D. A. Lawrence, R. H. Austin, and J. C. Sturm. Microfluidic device for label-free measurement of platelet activation. *Lab on a Chip*, 8(6):925–931, 2008.
- [30] K. J. Morton, K. Loutherbach, D. W. Inglis, O. K. Tsui, J. C. Sturm, S. Y. Chou, and R. H. Austin. Hydrodynamic metamaterials: Microfabricated arrays to steer, refract, and focus streams of biomaterials. *Proceedings of the National Academy of Sciences*, 105(21):7434–7438, 2008.
- [31] S. H. Holm, J. P. Beech, M. P. Barrett, and J. O. Tegenfeldt. Separation of parasites from human blood using deterministic lateral displacement. *Lab on a Chip*, 11(7):1326–1332, 2011.
- [32] J. V. Green, M. Radisic, and S. K. Murthy. Deterministic lateral displacement as a means to enrich large cells for tissue engineering. *Analytical chemistry*, 81(21):9178–9182, 2009.
- [33] H. N. Joensson, M. Uhlén, and H. A. Svahn. Droplet size based separation by deterministic lateral displacement—separating droplets by cell-induced shrinking. *Lab on a Chip*, 11(7):1305–1310, 2011.
- [34] D. J. Collins, T. Alan, and A. Neild. Particle separation using virtual deterministic lateral displacement (vdld). *Lab on a Chip*, 14(9):1595–1603, 2014.
- [35] Z. Liu, F. Huang, J. Du, W. Shu, H. Feng, X. Xu, and Y. Chen. Rapid isolation of cancer cells using microfluidic deterministic lateral displacement structure. *Biomicrofluidics*, 7(1):011801, 2013.

- [36] M. Heller and H. Bruus. A theoretical analysis of the resolution due to diffusion and size dispersion of particles in deterministic lateral displacement devices. *Journal of Micromechanics and Microengineering*, 18(7):075030, 2008.
- [37] D. Jin, B. Deng, J. X. Li, W. Cai, L. Tu, J. Chen, Q. Wu, and W. H. Wang. A microfluidic device enabling high-efficiency single cell trapping. *Biomicrofluidics*, 9(1):014101, 2015.
- [38] D. R. Gossett, W. M. Weaver, N. S. Ahmed, and D. Di Carlo. Sequential array cytometry: multi-parameter imaging with a single fluorescent channel. *Annals of biomedical engineering*, 39(4):1328–1334, 2011.
- [39] L. Lin, Y.-S. Chu, J. P. Thiery, C. T. Lim, and I. Rodriguez. Microfluidic cell trap array for controlled positioning of single cells on adhesive micropatterns. *Lab on a Chip*, 13(4):714–721, 2013.
- [40] D. B. Weibel, W. R. DiLuzio, and G. M. Whitesides. Microfabrication meets microbiology. *Nature Reviews Microbiology*, 5(3):209–218, 2007.
- [41] M. J. Madou. *Fundamentals of microfabrication: the science of miniaturization*. CRC press, 2002.
- [42] P. J. A. Kenis, R. F. Ismagilov, and G. M. Whitesides. Microfabrication inside capillaries using multiphase laminar flow patterning. *Science*, 285(5424):83–85, 1999.
- [43] R. I. Handin, S. E. Lux, and T. P. Stossel. *Blood: principles and practice of hematology*, volume 1. Lippincott Williams & Wilkins, 2003.
- [44] H. K. Lin, S. Zheng, A. J. Williams, M. Balic, S. Groshen, H. I. Scher, M. Fleisher, W. Stadler, R. H. Datar, Y.-C. Tai, et al. Portable filter-based microdevice for detection and characterization of circulating tumor cells. *Clinical Cancer Research*, 16(20):5011–5018, 2010.
- [45] S. Meng, D. Tripathy, E. P. Frenkel, S. Shete, E. Z. Naftalis, J. F. Huth, P. D. Beitsch, M. Leitch, S. Hoover, D. Euhus, et al. Circulating tumor cells in patients with breast cancer dormancy. *Clinical cancer research*, 10(24):8152–8162, 2004.
- [46] S. Park, R. R. Ang, S. P. Duffy, J. Bazov, K. N. Chi, P. C. Black, and H. Ma. Morphological differences between circulating tumor cells from prostate cancer patients and cultured prostate cancer cells. *PloS one*, 9(1):e85264, 2014.
- [47] Joseph DSilva. *High-Throughput Microfluidic Capture of Rare Cells from Large Volumes of Blood*. PhD thesis, Princeton University, 2016.
- [48] J. M. Ramirez, E. A. Thomann, E. C. Waymire, R. Haggerty, and B. Wood. A generalized Taylor–Aris formula and skew diffusion. *Multiscale Modeling & Simulation*, 5(3):786–801, 2006.

- [49] M. S. Bello, R. Rezzonico, P. G. Righetti, et al. Use of Taylor-Aris dispersion for measurement of a solute diffusion coefficient in thin capillaries. *SCIENCE-NEW YORK THEN WASHINGTON*, pages 773–773, 1994.
- [50] C. V. Chrysikopoulos, P. K. Kitanidis, and P. V. Roberts. Generalized Taylor-Aris moment analysis of the transport of sorbing solutes through porous media with spatially-periodic retardation factor. *Transport in Porous Media*, 7(2):163–185, 1992.
- [51] L. K. Tamm. Lateral diffusion and fluorescence microscope studies on a monoclonal antibody specifically bound to supported phospholipid bilayers. *Biochemistry*, 27(5):1450–1457, 1988.
- [52] A. R. L. Gear. Rhodamine 6g a potent inhibitor of mitochondrial oxidative phosphorylation. *Journal of Biological Chemistry*, 249(11):3628–3637, 1974.
- [53] S. A. Kim, K. G. Heinze, and P. Schuille. Fluorescence correlation spectroscopy in living cells. *Nature methods*, 4(11):963–973, 2007.
- [54] L. V. Johnson, M. L. Walsh, and L. B. Chen. Localization of mitochondria in living cells with rhodamine 123. *Proceedings of the National Academy of Sciences*, 77(2):990–994, 1980.
- [55] S. Massberg, G. Enders, R. Leiderer, S. Eisenmenger, D. Vestweber, F. Krombach, and K. Messmer. Platelet-endothelial cell interactions during ischemia/reperfusion: the role of p-selectin. *Blood*, 92(2):507–515, 1998.
- [56] L. L. Wright, A. G. Palmer, and N. L. Thompson. Inhomogeneous translational diffusion of monoclonal antibodies on phospholipid Langmuir-Blodgett films. *Biophysical Journal*, 54(3):463–470, 1988.
- [57] R. Karlsson, A. Michaelsson, and L. Mattsson. Kinetic analysis of monoclonal antibody-antigen interactions with a new biosensor based analytical system. *Journal of Immunological Methods*, 145(1-2):229–240, 1991.
- [58] D. W. Inglis. Efficient microfluidic particle separation arrays. *Applied Physics Letters*, 94(1):013510, 2009.
- [59] I. Ippolito, E. J. Hinch, G. Daccord, and J. P. Hulin. Tracer dispersion in 2-d fractures with flat and rough walls in a radial flow geometry. *Physics of Fluids A: Fluid Dynamics*, 5(8):1952–1962, 1993.
- [60] K. He, F. Babaye Khorasani, S. T. Retterer, D. K. Thomas, J. C. Conrad, and R. Krishnamoorti. Diffusive dynamics of nanoparticles in arrays of nanoposts. *ACS Nano*, 7(6):5122–5130, 2013.
- [61] I. I. Vlasov, A. A. Shiryaev, T. Rendler, S. Steinert, S.-Y. Lee, D. Antonov, M. Vörös, F. Jelezko, A. V. Fisenko, L. F. Semjonova, et al. Molecular-sized fluorescent nanodiamonds. *Nature Nanotechnology*, 9(1):54–58, 2014.

- [62] F. M. Zehentbauer, C. Moretto, R. Stephen, T. Thevar, J. R. Gilchrist, D. Pokrajac, K. L. Richard, and J. Kiefer. Fluorescence spectroscopy of rhodamine 6g: concentration and solvent effects. *Spectrochimica Acta Part A: Molecular and Biomolecular Spectroscopy*, 121:147–151, 2014.
- [63] L. Zeng, S. Balachandar, and P. Fischer. Wall-induced forces on a rigid sphere at finite reynolds number. *Journal of Fluid Mechanics*, 536:1–25, 2005.
- [64] P. Cherukat and J. B. McLaughlin. The inertial lift on a rigid sphere in a linear shear flow field near a flat wall. *Journal of Fluid Mechanics*, 263:1–18, 1994.
- [65] A. M. Mollinger and F. T. M. Nieuwstadt. Measurement of the lift force on a particle fixed to the wall in the viscous sublayer of a fully developed turbulent boundary layer. *Journal of Fluid Mechanics*, 316:285–306, 1996.
- [66] P. Stephen Williams, S. Lee, and J. Calvin Giddings. Characterization of hydrodynamic lift forces by field-flow fractionation. inertial and near-wall lift forces. *Chemical Engineering Communications*, 130(1):143–166, 1994.
- [67] J.-S. Park, S.-H. Song, and H.-I. Jung. Continuous focusing of microparticles using inertial lift force and vorticity via multi-orifice microfluidic channels. *Lab on a Chip*, 9(7):939–948, 2009.
- [68] K. K. Zeming, S. Ranjan, and Y. Zhang. Rotational separation of non-spherical bioparticles using i-shaped pillar arrays in a microfluidic device. *Nature communications*, 4:1625, 2013.
- [69] S. P. Klinken. Red blood cells. *The international journal of biochemistry & cell biology*, 34(12):1513–1518, 2002.
- [70] R. Skalak and P. Branemark. Deformation of red blood cells in capillaries. *Science*, 164(3880):717–719, 1969.
- [71] J. D’Silva, R. H. Austin, and J. C. Sturm. Inhibition of clot formation in deterministic lateral displacement arrays for processing large volumes of blood for rare cell capture. *Lab on a Chip*, 15(10):2240–2247, 2015.
- [72] K. Louterback, J. D’Silva, L. Liu, A. Wu, R. H. Austin, and J. C. Sturm. Deterministic separation of cancer cells from blood at 10 ml/min. *AIP advances*, 2(4):042107, 2012.
- [73] C. I. Civin, T. Ward, A. M. Skelley, K. Gandhi, Z. Peilun Lee, C. R. Dosier, J. L. D’Silva, Y. Chen, M. Kim, J. Moynihan, et al. Automated leukocyte processing by microfluidic deterministic lateral displacement. *Cytometry Part A*, 89(12):1073–1083, 2016.
- [74] J. A. Davis. *Microfluidic separation of blood components through deterministic lateral displacement*. PhD thesis, Princeton University, 2008.

- [75] P. R. Wheater, H. G. Burkitt, V. G. Daniels, et al. *Functional histology. A text and colour atlas*. Churchill Livingstone, 23 Ravelston Terrace, Edinburgh, EH4 3TL., 1979.
- [76] A. Sharei, J. Zoldan, A. Adamo, W. Y. Sim, N. Cho, E. Jackson, S. Mao, S. Schneider, M.-J. Han, A. Lytton-Jean, et al. A vector-free microfluidic platform for intracellular delivery. *Proceedings of the National Academy of Sciences*, 110(6):2082–2087, 2013.
- [77] P. Lebaron, N. Parthuisot, and P. Catala. Comparison of blue nucleic acid dyes for flow cytometric enumeration of bacteria in aquatic systems. *Applied and environmental microbiology*, 64(5):1725–1730, 1998.
- [78] D. A. Hammer and S. M. Apte. Simulation of cell rolling and adhesion on surfaces in shear flow: general results and analysis of selectin-mediated neutrophil adhesion. *Biophysical journal*, 63(1):35–57, 1992.
- [79] C. Dong and X. X. Lei. Biomechanics of cell rolling: shear flow, cell-surface adhesion, and cell deformability. *Journal of biomechanics*, 33(1):35–43, 2000.
- [80] S. I. Simon and H. L. Goldsmith. Leukocyte adhesion dynamics in shear flow. *Annals of biomedical engineering*, 30(3):315–332, 2002.
- [81] J. P. Brody, P. Yager, R. E. Goldstein, and R. H. Austin. Biotechnology at low reynolds numbers. *Biophysical journal*, 71(6):3430–3441, 1996.
- [82] E. H. Chapman, A. S. Kurec, and F. R. Davey. Cell volumes of normal and malignant mononuclear cells. *Journal of clinical pathology*, 34(10):1083–1090, 1981.
- [83] Y. F. Dufrière. Sticky microbes: forces in microbial cell adhesion. *Trends in microbiology*, 23(6):376–382, 2015.
- [84] M. Stefanini, C. De Martino, and L. Zamboni. Fixation of ejaculated spermatozoa for electron microscopy. *Nature*, 216(5111):173–174, 1967.
- [85] G. E. Palade. A study of fixation for electron microscopy. *The Journal of experimental medicine*, 95(3):285, 1952.
- [86] F. M. M. Morel, R. F. Baker, and H. Wayland. Quantitation of human red blood cell fixation by glutaraldehyde. *The Journal of cell biology*, 48(1):91, 1971.
- [87] J. W. Chan, D. S. Taylor, and D. L. Thompson. The effect of cell fixation on the discrimination of normal and leukemia cells with laser tweezers raman spectroscopy. *Biopolymers*, 91(2):132–139, 2009.
- [88] M. Moloney, L. McDonnell, and H. OShea. Atomic force microscopy of bhk-21 cells: an investigation of cell fixation techniques. *Ultramicroscopy*, 100(3):153–161, 2004.

- [89] L. L. Lanier and N. L. Warner. Paraformaldehyde fixation of hematopoietic cells for quantitative flow cytometry (facs) analysis. *Journal of immunological methods*, 47(1):25–30, 1981.
- [90] M. C. Jamur and C. Oliver. Permeabilization of cell membranes. *Immunocytochemical methods and protocols*, pages 63–66, 2010.
- [91] S. Choi, J. M. Karp, and R. Karnik. Cell sorting by deterministic cell rolling. *Lab on a Chip*, 12(8):1427–1430, 2012.
- [92] S. Lopez, L. Stuhl, S. Fichelson, A. Dubart-Kupperschmitt, R. St Arnaud, J.-R. Galindo, A. Murati, N. Berda, P. Dubreuil, and S. Gomez. Naca is a positive regulator of human erythroid-cell differentiation. *J Cell Sci*, 118(8):1595–1605, 2005.
- [93] H. Kim, H. Terazono, H. Takei, and K. Yasuda. Cup-shaped superparamagnetic hemispheres for size-selective cell filtration. *Scientific reports*, 4:6362, 2014.
- [94] T. A. J. Duke. Monte carlo reptation model of gel electrophoresis: steady state behavior. *The Journal of chemical physics*, 93(12):9049–9054, 1990.
- [95] O. Bakajin, T. A. J. Duke, J. Tegenfeldt, C.-F. Chou, S. S. Chan, R. H. Austin, and E. C. Cox. Separation of 100-kilobase dna molecules in 10 seconds. *Analytical chemistry*, 73(24):6053–6056, 2001.
- [96] L. R. Huang, J. O. Tegenfeldt, J. J. Kraeft, J. C. Sturm, R. H. Austin, and E. C. Cox. A dna prism for high-speed continuous fractionation of large dna molecules. *Nature biotechnology*, 20(10):1048–1051, 2002.
- [97] J. O. Tegenfeldt, C. Prinz, H. Cao, S. Chou, W. W. Reisner, R. Riehn, Y. M. Wang, E. C. Cox, J. C. Sturm, P. Silberzan, et al. The dynamics of genomic-length dna molecules in 100-nm channels. *Proceedings of the National Academy of Sciences of the United States of America*, 101(30):10979–10983, 2004.
- [98] E. T. Lam, A. Hastie, C. Lin, D. Ehrlich, S. K. Das, M. D. Austin, P. Deshpande, H. Cao, N. Nagarajan, M. Xiao, et al. Genome mapping on nanochannel arrays for structural variation analysis and sequence assembly. *Nature biotechnology*, 30(8):771–776, 2012.
- [99] Erik Borgström, Sverker Lundin, and Joakim Lundeberg. Large scale library generation for high throughput sequencing. *PloS one*, 6(4):e19119, 2011.
- [100] W. D. Volkmuth and R. H. Austin. Dna electrophoresis in microlithographic arrays. *Nature*, 358(6387):600–602, 1992.
- [101] T. Biben, P. Bladon, and D. Frenkel. Depletion effects in binary hard-sphere fluids. *Journal of Physics: Condensed Matter*, 8(50):10799, 1996.

- [102] J. Pelletier, K. Halvorsen, B.-Y. Ha, R. Paparcone, S. J. Sandler, C. L. Woldringh, W. P. Wong, and S. Jun. Physical manipulation of the escherichia coli chromosome reveals its soft nature. *Proceedings of the National Academy of Sciences*, 109(40):E2649–E2656, 2012.
- [103] S. Cunha, C. L Woldringh, and T. Odijk. Polymer-mediated compaction and internal dynamics of isolated escherichia coli nucleoids. *Journal of structural biology*, 136(1):53–66, 2001.
- [104] L. S. Lerman. A transition to a compact form of dna in polymer solutions. *Proceedings of the National Academy of Sciences*, 68(8):1886–1890, 1971.
- [105] S. B. Zimmerman and A. P. Minton. Macromolecular crowding: biochemical, biophysical, and physiological consequences. *Annual review of biophysics and biomolecular structure*, 22(1):27–65, 1993.
- [106] P. G. DE GENNES. *Scaling Concepts in Polymer*. Cornell University Press, 1979.
- [107] S. Asakura and F. Oosawa. Interaction between particles suspended in solutions of macromolecules. *Journal of polymer science*, 33(126):183–192, 1958.
- [108] N. Pamme. Continuous flow separations in microfluidic devices. *Lab on a Chip*, 7(12):1644–1659, 2007.
- [109] M. D. Tarn, M. J. Lopez-Martinez, and N. Pamme. On-chip processing of particles and cells via multilaminar flow streams. *Analytical and bioanalytical chemistry*, 406(1):139–161, 2014.
- [110] D. E. Smith, H. P. Babcock, and S. Chu. Single-polymer dynamics in steady shear flow. *Science*, 283(5408):1724–1727, 1999.
- [111] H. Yamakawa. *Modern theory of polymer solutions*. Harper & Row, 1971.
- [112] K. Günther, M. Mertig, and R. Seidel. Mechanical and structural properties of yoyo-1 complexed dna. *Nucleic acids research*, 38(19):6526–6532, 2010.
- [113] M. Rubinstein and R. H. Colby. Oxford university press; new york: 2003. *Polymer Physics*.
- [114] P. G. De Gennes. Coil-stretch transition of dilute flexible polymers under ultrahigh velocity gradients. *The Journal of Chemical Physics*, 60(12):5030–5042, 1974.
- [115] H. Kang, P. A. Pincus, C. Hyeon, and D. Thirumalai. Effects of macromolecular crowding on the collapse of biopolymers. *Physical review letters*, 114(6):068303, 2015.

- [116] K. Yoshikawa, Y. Yoshikawa, Y. Koyama, and T. Kanbe. Highly effective compaction of long duplex dna induced by polyethylene glycol with pendant amino groups. *Journal of the American Chemical Society*, 119(28):6473–6477, 1997.
- [117] N. H. Olson, M. Gingery, F. A. Eiserling, and T. S. Baker. The structure of isometric capsids of bacteriophage t4. *Virology*, 279(2):385–391, 2001.